

REPORT DOCUMENTATION PAGE			Form Approved OMB No. 074-0188	
Public reporting burden for this collection of information is estimated to average 1 hour per response, including the time for reviewing instructions, searching existing data sources, gathering and maintaining the data needed, and completing and reviewing the collection of information. Send comments regarding this burden estimate or any other aspect of the collection of information, including suggestions for reducing this burden to Washington Headquarters Services, Directorate for Information Operations and Reports, 1215 Jefferson Davis Highway, Suite 1204, Arlington, VA 22202-4302, and to the Office of Management and Budget, Paperwork Reduction Project (0704-0188), Washington, DC 20503.				
1. AGENCY USE ONLY (Leave blank)		2. REPORT DATE 7 May 2007		3. REPORT TYPE AND DATE COVERED
4. TITLE AND SUBTITLE A Quantitative Analysis of Starting Jet Vortex Ring Entrainment at Low Reynolds Number			5. FUNDING NUMBERS	
6. AUTHOR(S) Dulude, Alex G.				
7. PERFORMING ORGANIZATION NAME(S) AND ADDRESS(ES)			8. PERFORMING ORGANIZATION REPORT NUMBER	
9. SPONSORING/MONITORING AGENCY NAME(S) AND ADDRESS(ES)			10. SPONSORING/MONITORING AGENCY REPORT NUMBER	
US Naval Academy Annapolis, MD 21402			Trident Scholar project report no. 351 (2007)	
11. SUPPLEMENTARY NOTES				
12a. DISTRIBUTION/AVAILABILITY STATEMENT This document has been approved for public release; its distribution is UNLIMITED.				12b. DISTRIBUTION CODE
13. ABSTRACT The future propulsion of very small unmanned air and underwater vehicles operating at Reynolds numbers in the hundreds or less may be accomplished by pulsing a jet of fluid rather than more conventional methods of propulsion such as propellers and turbo jets as used by large-scale vehicles. Pulse jet propulsion produces trailing vortex rings and recent research concerning the formation and evolution of vortex rings has suggested that these structures may be exploited to augment the thrust and increase the efficiency of pulsed jet propulsion. Limited studies have indicated correlations between the length and shape of the generating pulse and the formation, fluid entrainment, and thrust augmentation provided by the resultant vortex ring at ring Reynolds number as low as approximately 13,000. The onset of vortex ring pinch-off has previously been shown to be a limit to this thrust augmentation. The design, construction, and implementation of a novel, piston-cylinder-type, vortex ring generator to confirm and further improve measurements of fluid entrainment and other formation characteristics has been accomplished. This apparatus was used in dye injection studies and stereoscopic particle image velocimetry (SPIV) studies to qualitatively examine the evolution of the vortex ring, and evaluate the effects of pulse length and shape on the formation of the vortex ring over a range of Reynolds numbers between 250 and 13,000. Results from this investigation at a Reynolds number of 13,000 are in close agreement with those of previous research, indicating that pulse shaping can delay the phenomena of vortex ring pinch-off by as much as 20% of the stroke length to diameter ratio. Results from lower Reynolds numbers show a trending toward even greater delay of pinch-off, as Reynolds number decreases. Tests conducted at Re=250 indicate a delay in pinch-off in excess of 400% over that seen at Re=13,000.				
14. SUBJECT TERMS Vortex ring, PIV, Reynolds number			15. NUMBER OF PAGES 110	
			16. PRICE CODE	
17. SECURITY CLASSIFICATION OF REPORT	18. SECURITY CLASSIFICATION OF THIS PAGE	19. SECURITY CLASSIFICATION OF ABSTRACT	20. LIMITATION OF ABSTRACT	

U.S.N.A. --- Trident Scholar project report; no. 351 (2007)

A Quantitative Analysis of Starting Jet Vortex Ring Entrainment at Low Reynolds Number

by

Midshipman 1/C Alex G. Dulude
United States Naval Academy
Annapolis, Maryland

(signature)

Certification of Advisers Approval

Assistant Professor Eric N. Hallberg
Aerospace Engineering Department

(signature)

(date)

Assistant Professor David S. Miklosovic
Aerospace Engineering Department

(signature)

(date)

Acceptance for the Trident Scholar Committee

Professor Joyce E. Shade
Deputy Director of Research & Scholarship

(signature)

(date)

USNA-1531-2

ABSTRACT

The future propulsion of very small unmanned air and underwater vehicles operating at Reynolds numbers in the hundreds or less may be accomplished by pulsing a jet of fluid rather than more conventional methods of propulsion such as propellers and turbo jets as used by large-scale vehicles. Pulse jet propulsion produces trailing vortex rings and recent research concerning the formation and evolution of vortex rings has suggested that these structures may be exploited to augment the thrust and increase the efficiency of pulsed jet propulsion. Limited studies have indicated correlations between the length and shape of the generating pulse and the formation, fluid entrainment, and thrust augmentation provided by the resultant vortex ring at ring Reynolds number as low as approximately 13,000. The onset of vortex ring pinch-off has previously been shown to be a limit to this thrust augmentation. The design, construction, and implementation of a novel, piston-cylinder-type, vortex ring generator to confirm and further improve measurements of fluid entrainment and other formation characteristics has been accomplished. This apparatus was used in dye injection studies and stereoscopic particle image velocimetry (SPIV) studies to qualitatively examine the evolution of the vortex ring, and evaluate the effects of pulse length and shape on the formation of the vortex ring over a range of Reynolds numbers between 250 and 13,000. Results from this investigation at a Reynolds number of 13,000 are in close agreement with those of previous research, indicating that pulse shaping can delay the phenomena of vortex ring pinch-off by as much as 20% of the stroke length to diameter ratio. Results from lower Reynolds numbers show a trending toward even greater delay of pinch-off, as Reynolds number decreases. Tests conducted at $Re=250$ indicate a delay in pinch-off in excess of 400% over that seen at $Re=13,000$.

Keywords: vortex ring, PIV, Reynolds number

ACKNOWLEDGEMENTS

First, I would like to thank my advisors, Assistant Professors Eric Hallberg and David Miklosovic, whose expertise, guidance, and enthusiasm were essential to the successful execution of this project.

I would also like to thank the many talented and dedicated professionals of the USNA Technology Support Division, who worked commendably to craft the parts that were critical to this project. Specifically, Mr. Bowie Smith and Mr. Jerry Myers receive thanks for their tireless efforts on a difficult project.

The USNA Fluids Laboratory staff made every effort to facilitate this project and was critical to its successful completion. Special thanks go to Mr. Dick Garman for his guidance and sharing his office, Mr. Rusty Foard for his technical advice and expertise, Ms. Louise Becnel for ensuring materials were received in a timely manner, and Mr. Fritz Woolford for his assistance with the electrical aspects of this work.

The Ms. Cindi Gallagher of the MSC Graphics Lab ensured that the visual aspects of this work had a polished, professional appearance, and I wholeheartedly thank her for that.

Finally, I would like to thank Professor Joyce Shade and the Trident Committee for their guidance and constructive input, as well as the opportunity to conduct this research.

TABLE OF CONTENTS

Abstract.....	1
Acknowledgements.....	2
Table of contents.....	3
List of Figures.....	5
List of Tables.....	7
List of Symbols.....	7
1 Introduction.....	8
1.1 Background.....	8
1.2 Structure of a Vortex Ring.....	14
1.2.1 Reference Geometry.....	14
1.2.2 Composition.....	16
1.3 Key Performance Parameters.....	19
2 Experimental Setup.....	22
2.1 Vortex Ring Generator.....	22
2.1.1 Piston.....	23
2.1.2 Nozzle.....	24
2.1.3 Motor.....	26
2.2 Testing Tank.....	30
2.3 Viscometer.....	31
2.4 Stereoscopic Particle Image Velocimetry Setup.....	32
2.4.1 Background.....	32
2.4.2 Process.....	32
2.4.3 Equipment.....	34
2.4.4 Calibration.....	34
2.5 Experimental Method.....	37
2.5.1 Viscosity Measurement.....	38
2.5.2 Capture Timing.....	38
2.5.3 Image Processing.....	40
2.5.4 Recursion.....	41
2.6 Reduced Reynolds Number Regimes.....	42
2.6.1 Kinematic Viscosity Determination.....	43
2.6.2 Solution Mixing.....	43
2.6.3 Humidity and Viscosity Effects.....	44
2.6.4 Viscosity Similarity.....	45
3 Results.....	47
3.1 Vector Dropout.....	47
3.2 Velocity Profile and Vorticity Production.....	47
3.3 Pinch-Off.....	48
3.4 Results at $Re=13,000$	53

	4
3.4.1 Right Skew Profile	54
3.4.2 Left Skew Profile.....	57
3.4.3 Symmetrical Profile.....	60
3.4.4 Impulsive Profile	63
3.5 Results at $Re=1,500$	66
3.5.1 Right Skew Profile	66
3.5.2 Left Skew Profile.....	68
3.5.3 Symmetrical Profile.....	69
3.5.4 Impulsive Profile	70
3.6 Results at $Re=780$	71
3.7 Results at $Re=250$	73
3.7.1 Influence of Velocity Profile	74
3.7.2 Ring Structure.....	77
3.8 Summary of Observed Trends.....	80
3.9 Implications of Results	81
4 Conclusions.....	84
4.1 Recommendations	85
Bibliography	87
Appendix A: Contraction Curve Script.....	91
Appendix B: Velocity Profile Generator Script.....	93
Appendix C: Sample Velocity Profile	96
Appendix D: Ensemble Averaging Script.....	97
Appendix E: Vorticity Contour Generator Script	102
Appendix F: Tank Mixing Script.....	105
Glossary	107

LIST OF FIGURES

Figure 1. Relative sizes and flight regimes of representative aircraft.....	9
Figure 2. Relative sizes and regimes of representative marine vehicles and animals	10
Figure 3. Schematic of typical gas-powered pulse jet engine.....	12
Figure 4. Entrainment and evolution of a piston-induced vortex ring in dye laden water	14
Figure 5. Vortex ring in y-z plane, propagating vertically out of the plane of the paper	15
Figure 6. Cross-section of vortex ring, propagating to the right.....	15
Figure 7. Simplified two-dimensional representation of vortex ring formation.....	16
Figure 8. Diagram of vortex ring, showing fluid regions	17
Figure 9. Vortex ring, with injected dye highlighting fluid zones.....	18
Figure 10. Velocity profiles of right and left skew	21
Figure 11. Design drawings of vortex generator apparatus	24
Figure 12. Design drawings of nozzle	25
Figure 13. Contraction curve used to manufacture nozzle	26
Figure 14. MDrive motor shown attached to mounting plate.....	27
Figure 15. Normalized velocity profiles	28
Figure 16. Sample graphical depiction of right skew velocity profiles for a range of L/D	29
Figure 17. Fully-assembled test apparatus, with calibration target in place	31
Figure 18. Viscometer with high-viscosity spindle attached.....	31
Figure 19. Simplified depiction of SPIV correlation	33
Figure 20. Calibration target positioned on base, in interrogation region	35
Figure 21. Calibration target in place, showing orientation of mirror and laser.....	35
Figure 22. Final camera mounting positions.....	36
Figure 23. Processed calibration images, showing grid definition	37
Figure 24. Plot of K_3 variation with glycerin concentration.....	46
Figure 25. Vertical velocity component plot for a pinched off vortex ring.....	49
Figure 26. Translational velocity component maps for rings of various proximity to pinch-off	51
Figure 27. Vorticity contour plot showing primary and secondary vortices	52
Figure 28. Vortex contour plots with trailing vortices of varying levels of development.....	53
Figure 29. Velocity plots for the right skew profile, at $Re=13,000$	55
Figure 30. Vorticity maps for the right skew profile at $Re=13,000$	56
Figure 31. Velocity plots for the left skew profile, at $Re=13,000$	58
Figure 32. Vorticity contours for the left skew profile, at $Re=13,000$	59
Figure 33. Velocity flood plots for the symmetrical profile, at $Re=13,000$	62
Figure 34. Vorticity contours for the symmetrical profile, at $Re=13,000$	62
Figure 35. Velocity flood plots for the impulsive profile, at $Re=13,000$	64
Figure 36. Vorticity contours for the impulsive profile, at $Re=13,000$	65
Figure 37. Velocity maps for right skew profile at $Re=1,500$ and $L/D=5$	67
Figure 38. Vorticity contour plot for right skew profile at $Re=1,500$ and $f_n = 5$	67
Figure 39. Velocity component maps for left skew profile at $Re=1,500$ and $f_n = 6$	68

Figure 40. Vorticity contour map for left skew-generated vortex at $Re=1500$ and $f_n = 6$	68
Figure 41. Vorticity contours for symmetrical profile at $Re=1,500$ and $L/D=6$	69
Figure 42. Component velocity flood plots for the impulsive profile at $Re=1,500$ and $L/D=6$...	70
Figure 43. Vorticity contour plot for the impulsive profile at $Re=1,500$ and $L/D=6$	71
Figure 44. Component velocity plots for the right skew profile at $Re=780$ and $L/D=6$	72
Figure 45. Vorticity contours for the right skew profile, at $Re=780$	73
Figure 46. Axial velocity maps showing velocity profile insensitivity, at $Re=250$	76
Figure 47. Velocity component plots of varying profiles, at $Re=250$	79
Figure 48. Vorticity contours, at $Re=250$	80
Figure 49. Major observed vortex ring evolutionary trends, with Reynolds number	81

LIST OF TABLES

Table 1. Ranges of time delays utilized	39
Table 2. Time steps used to obtain captures in test solutions	39
Table 3. L/D ratios examined in secondary sweep in pure water	42
Table 4. Daily viscosity and Reynolds number measurements taken for 80% glycerin solution.	45

LIST OF SYMBOLS

A	area of nozzle exit plane
D	characteristic length (nozzle exit diameter)
f_n	ring formation number
L/D	slug length to diameter ratio
m_{added}	mass of fluid in the added mass region
$m_{ejected}$	mass of fluid in the vortex previously expelled through the nozzle
$m_{entrained}$	mass of ambient fluid incorporated into the ring
p_{cl}	pressure at nozzle exit plane
p_{∞}	ambient pressure
Re	Reynolds Number
t^*	time of end of circulation injection
t_p	pulse duration
U	nozzle exit velocity
U_j	jet velocity at nozzle exit
W	propagation velocity of vortex ring
x	distance from nozzle exit plane, along vortex propagation path
\bar{x}	mean average of velocity profile
\tilde{x}	median of velocity profile
Γ	vortex ring circulation
Γ_s	circulation due to slug effects
Γ_p	circulation due to overpressure
γ	skewness
ρ	fluid density
σ	standard deviation of the velocity profile
μ	fluid viscosity
ν	kinematic viscosity

1 INTRODUCTION

1.1 Background

Over the last decade, numerous successes in the implementation of unmanned aerial vehicles (UAVs) into the battlespace by American military forces have led researchers and military strategists to consider the further miniaturization of such vehicles. In fewer than five years, practical UAVs have gone from the 14 foot Pioneer reconnaissance aircraft to the diminutive 4 foot wide Sender UAV, suggesting that significantly smaller flying vehicles could be possible. Recent initiatives led by the Defense Advanced Research Project Administration (DARPA) have begun to explore the potential for practical application of these small vehicles for use in the battlespace. The Micro Air Vehicle (MAV) initiative, in particular, has been fielded for the purpose of demonstrating the feasibility of employing vehicles with wingspans on the scale of 15 cm or less in the near future (Wilson 1998). In addition to being reduced in size, aerial vehicles have been designed to operate in flight regimes in which viscous forces exert an increased influence on vehicle motion. This influence is conventionally characterized using the Reynolds number, which is a ratio between the inertial and viscous forces acting on a representative segment of the craft, and defined according to the equation:

$$\text{Re} = \frac{UD}{\nu} \quad (1)$$

In this relationship, U represents velocity, D represents a representative length, and ν represents the kinematic viscosity of the fluid medium. A summary of characteristic Reynolds numbers for a variety of common aerial vehicles is shown in Figure 1. Notable in this diagram is the specific region of interest for MAVs, namely $10^1 < \text{Re} < 10^4$.

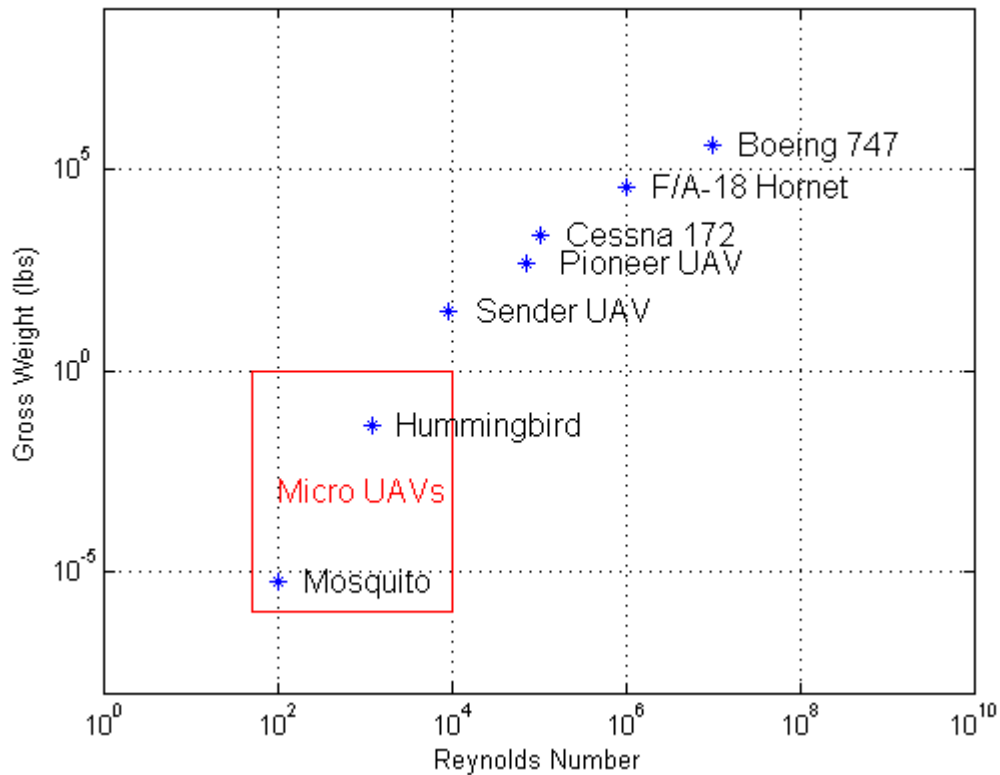


Figure 1. Relative sizes and flight regimes of representative aircraft

Simultaneously, in the oceanographic community, remotely operated vehicles (ROVs) were being tested and used to great acclaim in a variety of information gathering, object recovery, underwater repair, and myriad other applications. In this arena as well, much emphasis has been placed upon the miniaturization of said vehicles for the purposes of increasing the range of applications, decreasing the potential for detection, and reducing equipment cost. A graphical depiction of these trends is shown in Figure 2.

In this arena, propulsion has been a limiting factor to miniaturization. It is believed that this is due to the fact that propulsion system designs for these craft have largely been scaled-down versions of conventional designs. Through experiment, both the conventional propeller drive and impeller-jet/ducted fan drives have been found to be excessively bulky, heavy, and inefficient in micro-UUV applications (Mohseni 2006). The physical size of these systems

compromises payload capacity, while their heft deprives the craft of speed and buoyancy. The relatively high power consumption of these systems has severely limited vehicle endurance, thereby reducing the mission envelope. Additionally, the selection of one propulsion system over another in ROVs has dictated that the craft be limited to either high-speed maneuvering with poor station-keeping characteristics, or slow-speed operations, with better station-keeping abilities (Mohseni 2006). To broaden the effectiveness of such vehicles, a propulsion system which would permit operation in both regimes is desirable. For this, lightweight synthetic jets, which emit vortex rings, have been shown to be a viable method (Mohseni 2006). The efficiency of these jets is linked directly to the efficient entrainment and optimization of the vortex ring.

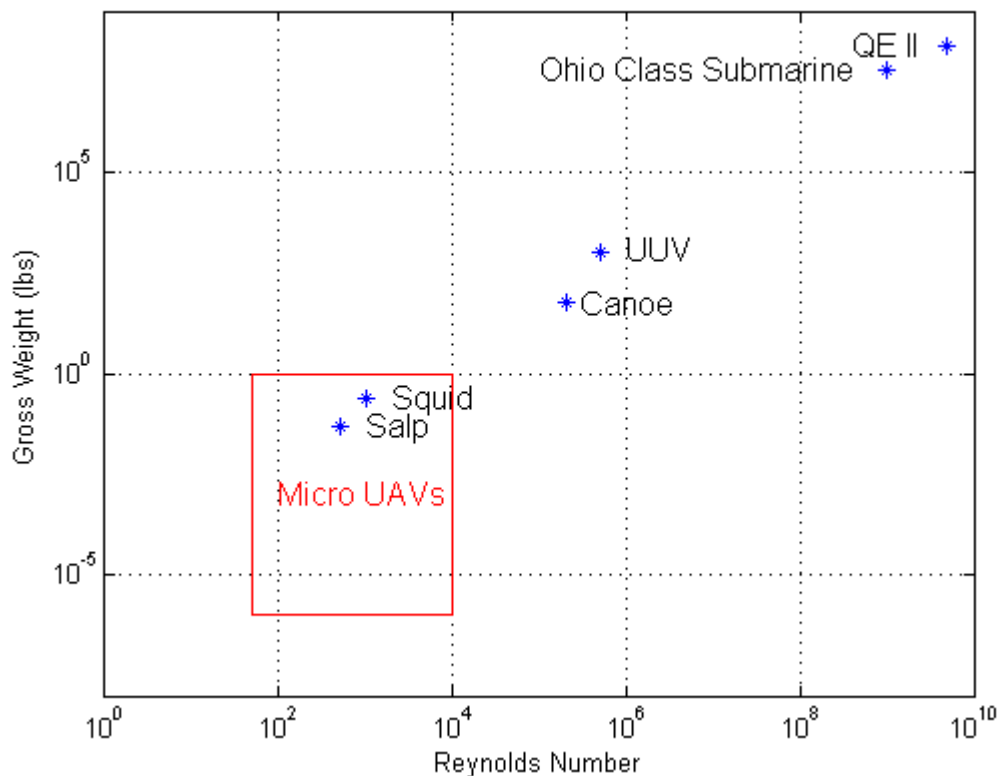


Figure 2. Relative sizes and regimes of representative marine vehicles and animals

This miniaturization of unmanned vehicles has been primarily driven by the implications of the now well-known Moore's Law. As the size and power requirements of the microelectronics that drive the controls, communications, and payload systems have been reduced, the vehicles have

undergone a similar reduction in size. Means of propulsion and lift, however, have remained largely conventional. The further miniaturization of unmanned air vehicles to a size smaller than approximately that of a hummingbird present interesting engineering challenges. Such vehicles, whether designed for flight or underwater travel, would be restricted by their very nature and design to operation in the low Reynolds numbers regimes of a few thousand or below. As interest in fluid flow and vehicle operation in this regime has only been generated in recent years, there is a need for more information on the flow characteristics at these Reynolds numbers.

Very-small UAV designs have been hampered as they have mainly been efforts at scaling-down larger, conventional designs; implementation and operation will likely need to exploit the unique nature of this regime. In this vein, some research teams have focused on using an ornithopter, or flapping-wing principle for propulsion of these small craft, and although initial results appear promising, these devices have been found largely to be structurally unsound (Michelson 2004). A divergent approach which would make use of the intrinsic differences in this regime, suggested by natural trends in Figure 1 and Figure 2, would be to use a jet-type propulsor, as does a squid or salp (Mohseni 2006). This theory is bolstered by the work of Rayner (1979), who showed that the propulsion of humming birds and hovering insects is a pulsed-thrust phenomenon, caused by the production of vortex rings in the wake of the wing.

Of seminal importance to vehicle design for low Reynolds number regimes is the pronounced degradation in aerodynamic performance of propellers, leading to poor propulsive efficiency, which has been observed for chord Reynolds numbers below 100,000 (Mueller 1985). In these laminar flow conditions, the airflow distribution over the propeller is characterized by laminar boundary layer separation and irregular turbulent transition and flow reattachment, which significantly increase the drag on the propeller, thereby increasing the torque and power demand on the engine, and greatly reduce the thrust provided. This significantly reduces the overall propulsive efficiency of the propeller-engine combination. Therefore, while the functionality of propellers at high Reynolds numbers is driven predominantly by pressure effects, that of low Reynolds number propellers is dominated by viscous effects. This change renders conventional

propellers unsuitable for employment as primary propulsion devices for UAVs on the one inch scale. This has spurred investigations into the potential suitability of jet-type engines for very-small UAV use. However, the complexity, required tolerances, and manufacturing limitations related to the moving parts, along with the ensuing fuel economies of current turbomachinery appear to be disqualifying characteristics for their application at this scale (Epstein 1997).

Natural flight and propulsion studies of animals which typically operate in low Reynolds number regimes, such as humming birds (*Selasphorus scintilla*) and salps (*Salpa thompsoni*), indicate pulsatile propulsion schemes as a possible alternative for motive power of small UAVs (Siekman 1963 and Weihs 1977). By definition, a pulse-jet is a propulsive device which expels exhaust in discrete, intermittent bursts. A schematic of a representative gas-powered pulse jet engine is shown in Figure 3. Notable in this diagram is the relatively small number of parts when compared to the turbojet or even reciprocating engine. This simplicity of construction, high thrust to weight ratio, and comparative fuel economy of the pulse-jet engine have designated it a prime candidate for application to low Reynolds number regimes.

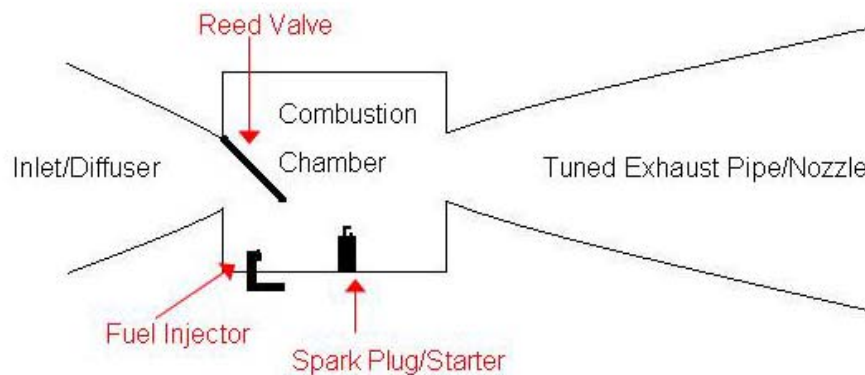


Figure 3. Schematic of typical gas-powered pulse jet engine

Although largely neglected by the aerospace industry for almost sixty years, the employment of the pulse-jet in UAVs would not be without precedent, as the World War II-era, German V-1 “Buzzbomb” was powered by a large Schmidt-type pulse-jet. These systems, however, operated

in a regime of much higher Reynolds numbers, and results in that regime are not necessarily transferable to the smaller scale required by MAVs. Available data concerning fluid flow in the low Reynolds number regime in which these diminutive UAVs would operate is sparse, and more research is required before micro pulsejet designs can be implemented.

While the time-variant thrust output of a pulsed jet has known advantages at higher Reynolds numbers, vortex ring entrainment is the key phenomenon to producing feasible propulsive efficiencies at low Reynolds numbers. An impulsively-started piston can be used to create a jet flow through a nozzle or orifice. At the exit plane of the nozzle, the viscous boundary layer will separate and roll up into a vortex ring that translates downstream of the nozzle. The vortex motion is characterized as a time-dependent flow which must match the impulse delivered by the vortex ring generator, making the startup process an important element of understanding the overall problem. A focus of debate is how the maximum circulation and energy can be imparted to the vortex ring by the piston. Vortex ring entrainment is defined as the net momentum imparted to the surrounding fluid by the translating vortex ring. Hence, a time-averaging of the jet flow field results in a net axial momentum flux, or thrust.

As the sequence of images in Figure 4 shows, the entrainment and evolution of a vortex ring is a three-dimensional, time-dependent process. The dye-laden vortex in these images was formed at similar Reynolds number to the goal of this study, and its evolution shows how the viscous forces of the fluid medium exert shearing stresses on the slug of fluid ejected from the nozzle, engendering the formation of the toroidal vortex ring. Following initial ring formation in part b below, no additional energy from the nozzle is injected into the ring. However, the translation of this ring and circular flow of fluid inside it cause quiescent fluid particles to be pulled into the ring, causing a net dilatation and increase in momentum flux, as seen in part c. This entrainment lasts only a finite amount of time before the viscous forces in the medium induce ring disintegration, as shown in the part d. For this reason, maximizing the efficiency of ring entrainment in the early stages of its evolution is a critical element in increasing the momentum flux.

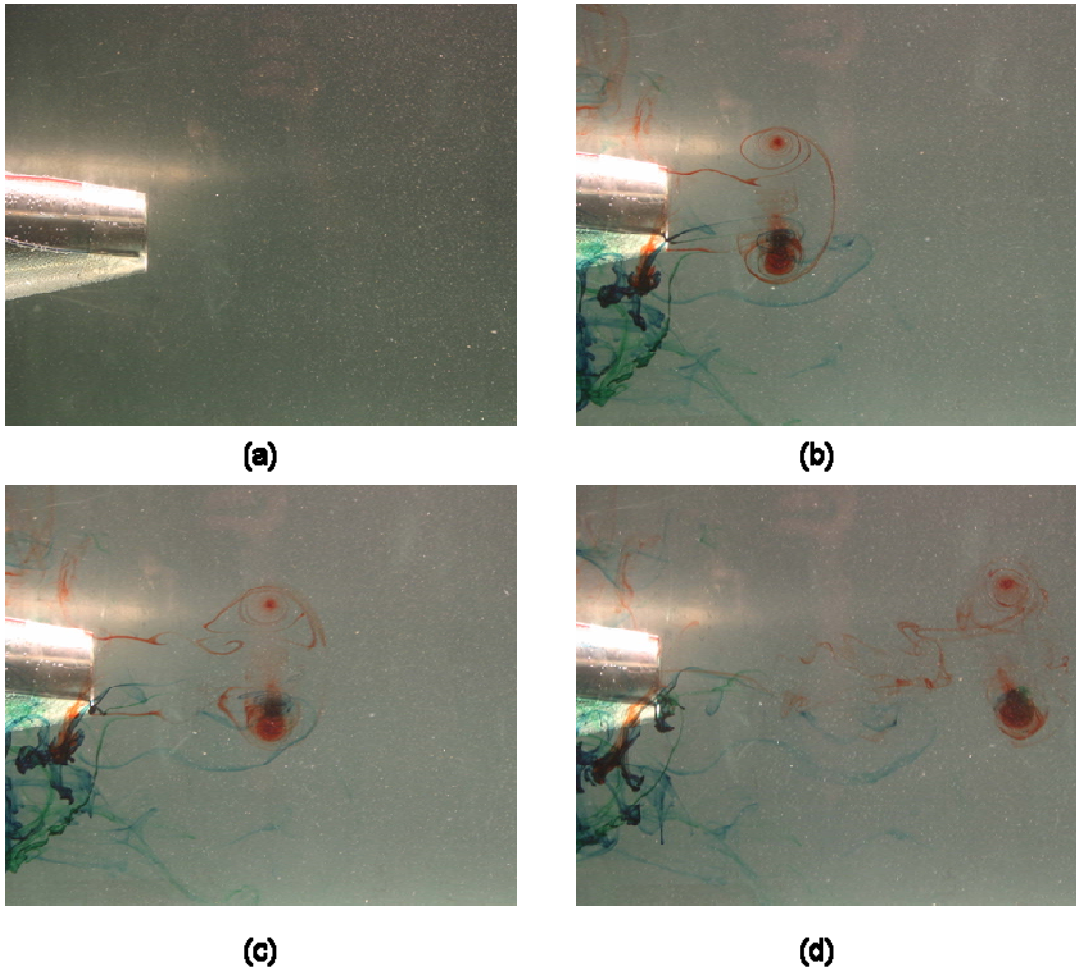


Figure 4. Entrainment and evolution of a piston-induced vortex ring in dye laden water ($Re=13,000$)

1.2 Structure of a Vortex Ring

1.2.1 Reference Geometry

Although a vortex ring is a three-dimensional, toroidal structure (Figure 5), it has been shown to have a high degree of symmetry along the translational axis (Shariff and Leonard 1992). This permits the simplification whereby vortex rings are conventionally discussed and presented graphically using only the two-dimensional cross section illustrated in Figure 6.

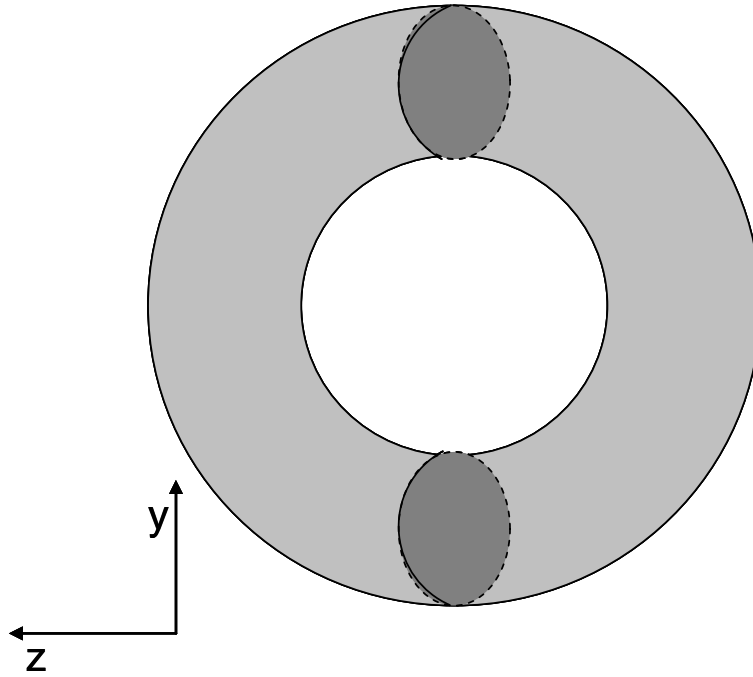


Figure 5. Vortex ring in y-z plane, propagating vertically out of the plane of the paper

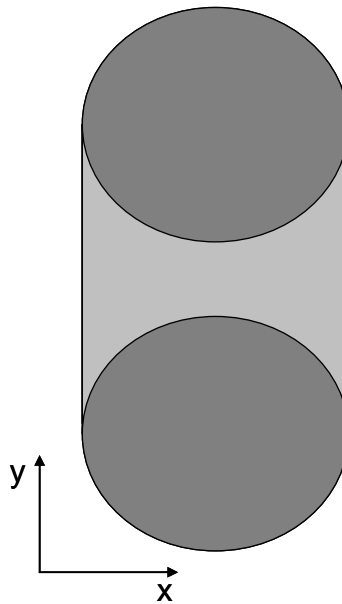


Figure 6. Cross-section of vortex ring, propagating to the right

The velocity components of the vortex ring and fluid particles in the ring follow the standard Cartesian notation. Namely, the velocity components in the x , y , z directions are designated u , v ,

w, respectively. Per established convention, the bulk velocity of the vortex ring is designated W , and has the same directionality as the u velocity components (Krueger and Gharib 2003). These terms are illustrated in Figure 7 below, which presents a simplified representation of the formation of a vortex ring.

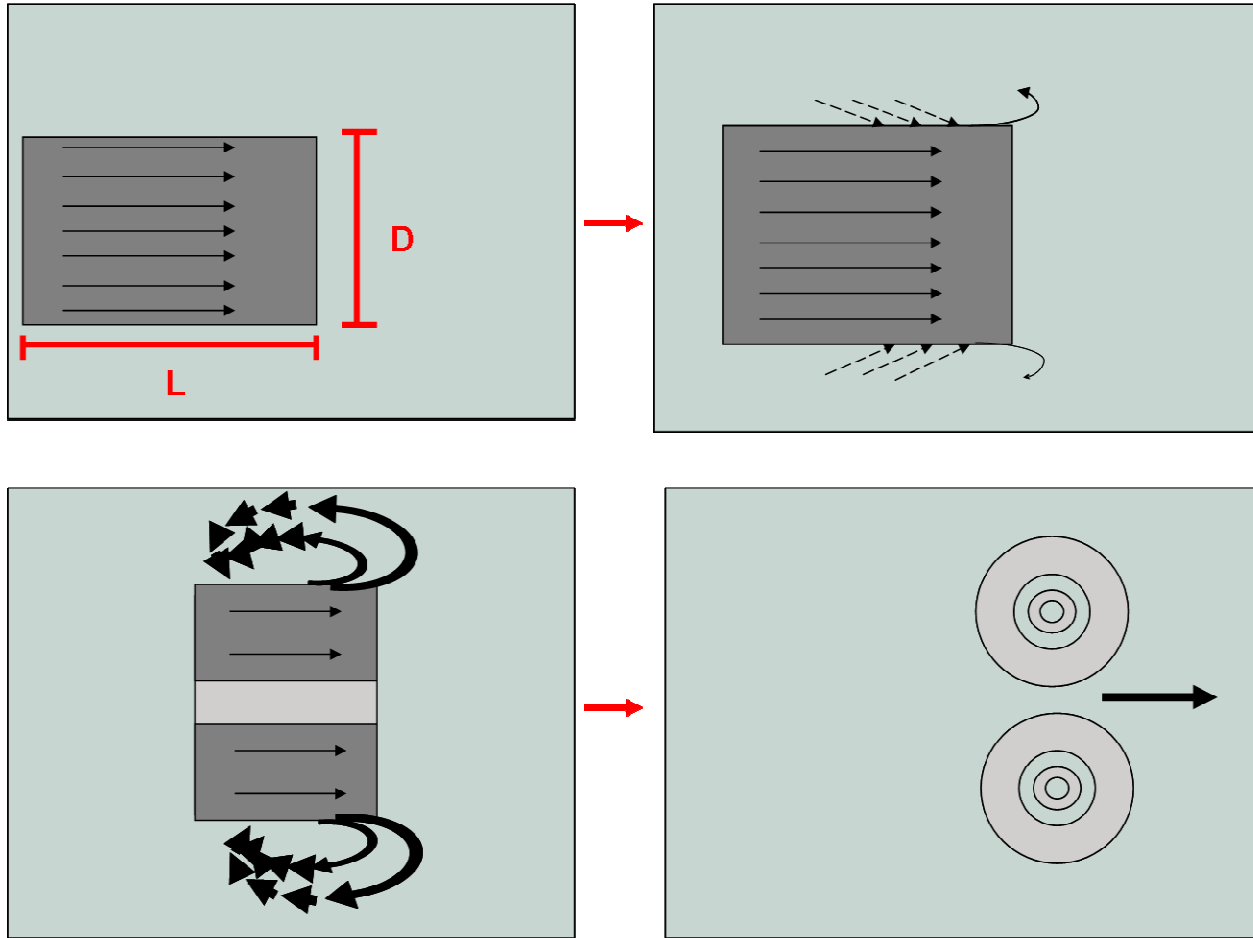


Figure 7. Simplified two-dimensional representation of vortex ring formation

1.2.2 Composition

The composition of a vortex ring is essential to understanding the thrust advantage provided by this structure. The vortex ring is comprised of fluid from three different sources. These fluid regions are most easily visualized by examining a two-dimensional slice of the ring, taken in the plane of ring propagation, as shown in schematic format in Figure 8 and via dye injection in Figure 9.

First, there is the mass of fluid ejected from the nozzle, $m_{ejected}$, shown in white in Figure 8 and in colored dye in Figure 9. As this fluid exits the nozzle, it's outside layer shears against the ambient fluid and is rolled into the two vortex cores shown by the concentric circles. The interplay of the fluid jet and the ambient fluid on the shear layer in the jet propagates this structure (Krueger and Gharib 2003).

As the vortex core forms and propagates downstream, ambient fluid is entrained into the vortex bubble and accelerated, $m_{entrained}$. These regions are shown in dark gray in Figure 8 and match the background in Figure 9. This fluid may be sucked into the vortex cores, or may simply be pulled and held inside the vortex bubble, which is demarcated with hashed lines in both figures. A characteristic property of this entrained fluid is that it propagates through space at the same net velocity, W , as the ejected fluid and the bulk ring structure (Didden 1979).

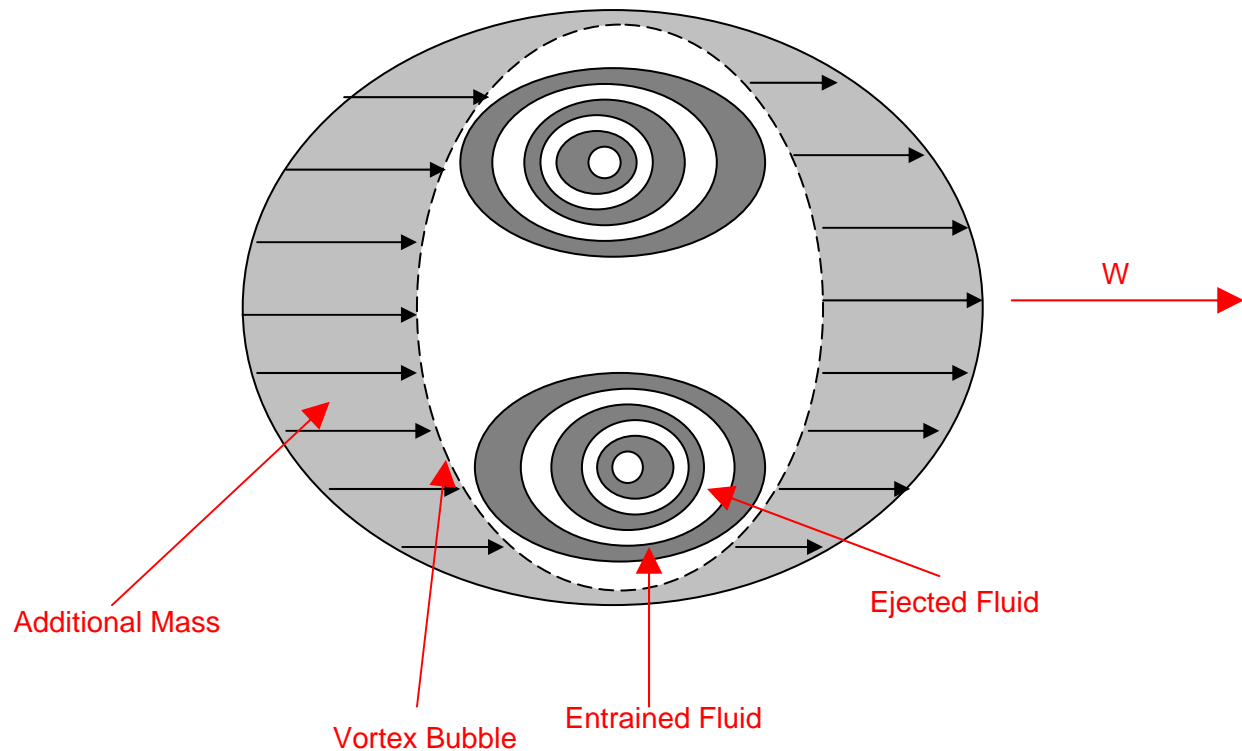


Figure 8. Diagram of vortex ring, showing fluid regions

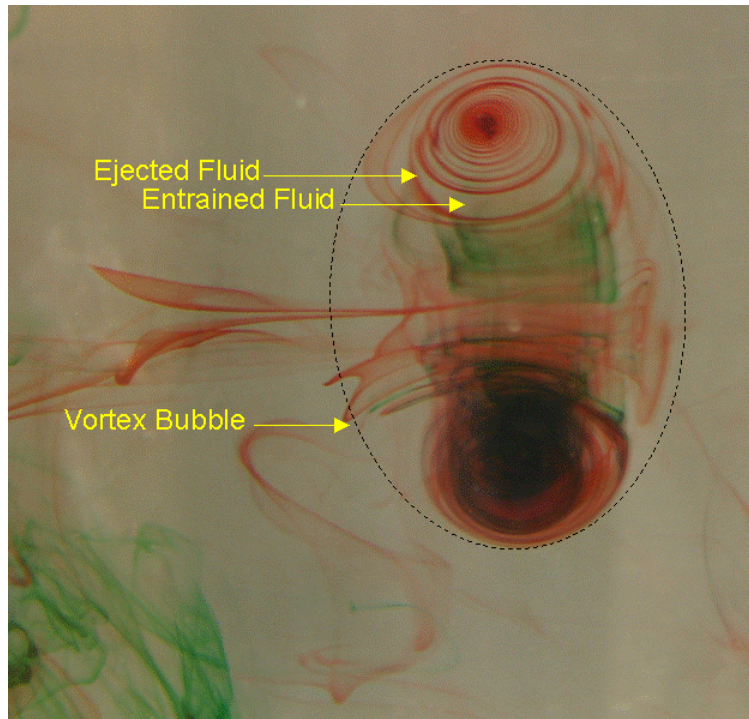


Figure 9. Vortex ring, with injected dye highlighting fluid zones

The third region of fluid in a vortex ring has been dubbed the “Added Mass” region in the literature (Krueger and Gharib 2003). This is an oblong region of increased fluid velocity caused by the fast vortex bubble pushing through the quiescent environmental fluid. Fluid in front of the bubble is accelerated in a manner analogous to snow being carried by a plow, while the fluid behind the bubble is dragged along in the partial-vacuum of the wake, in accordance with continuity (Krueger 2003). The fluid in this region may be sheared away, but it must be replaced with ambient fluid, again in accordance with continuity, so the overall effect is that the mass in this region, m_{added} , is moving at the propagation velocity, W (Krueger 2003).

When the momentum of all three of these regions is summed, the net impulse produced by the ring (due solely to the fluid momentum of the ring), I_U , is given by:

$$I_U = (m_{ejected} + m_{entrained} + m_{added})W \quad (2)$$

1.3 Key Performance Parameters

In Weihs' study of 1977, it was noted that the more advanced aquatic creatures utilize a pulsed jet mechanism for propulsion. Time averaging of thrust data indicated the realization of thrust augmentation in excess of 40% in creatures using pulsatile propulsion over those utilizing a steady jet. Also noted in this study was that the slug length to nozzle exit diameter ratio, L/D , was nearly 4 in all species, suggesting a universal value for the optimization of thrust augmentation in a pulsed propulsion scheme.

The work of Krueger and Gharib (2003) indicates that the optimization of the thrust potential of a vortex ring is strongly dependent on L/D . Their research suggests the existence of a quantity known as the formation number, f_n , which is defined as the largest L/D for a given velocity profile which yields a jet exhaust characterized by a single vortex ring. Rings created using L/D larger than the formation number were observed to experience a phenomenon known as 'pinch-off,' whereby the vortex ring separated from the jet outflow, creating a second, weaker vortex aft of the main vortex. The thrust attained from the pinched rings was less than that of the rings created at the formation number by as much as 30%, indicating a distinct advantage to using pulses tuned to the formation number (Krueger and Gharib 2003).

Rosenfeld et al. (1998) showed empirically that manipulation of the piston velocity profile could cause the formation number to shift. Krueger and Gharib (2003) validated this observation using particle image velocimetry (PIV), and showed that thrust augmentation is maximized through the creation of rings with the largest formation number. This study suggested that piston velocity profiles consisting primarily of acceleration to a specified maximum velocity tended to delay pinch-off by as much as an entire L/D over other profiles. However, their inability to precisely regenerate their velocity profiles has cast doubt on the specific validity of these data.

A final parameter of experimental relevance to the study of the optimization of vortex rings is the observed pressure-induced increase in circulation in the vortex ring over that of the steady jet (Krueger 2005). Vortex ring theory has largely been dominated by the so-called “Slug Model” for predicting ring circulation since the proposal of this model by Glezer in 1988 and its validation and refinement by Shariff and Leonard in 1992. This model predicts the circulation of the vortex ring as

$$\Gamma = \frac{1}{2} \int_0^{t_p} U_J^2(t) dt \quad (3)$$

However, experiments (e.g., Gharib, Rambod, and Shariff 1998; as well as Zhao, Frankel, and Mongeau 2000) have shown that this model under-predicts the circulation of the vortex ring by as much as 67% (Krueger 2005). As Krueger showed in his 2005 paper, this difference in circulation is due to an increase in circulation caused by the increase in pressure at the nozzle exit plane that occurs upon jet startup. This pressure is believed to be caused by the unsteady effects of the initiation of fluid flow out the nozzle exit, which distorts the shape of the velocity profile of the nozzle exit plane. Specifically, radial velocity in the nozzle exit plane is induced, increasing the vorticity and circulation of the flow (Krueger 2005). The corrected circulation, accounting for nozzle-exit overpressure (NEOP) effects, is presented by Krueger as the sum of the circulation from the fluid slug and the circulation induced by NEOP effects:

$$\Gamma = \Gamma_s + \Gamma_p \quad (4)$$

which is expanded to the more useful form:

$$\Gamma = \frac{1}{2} \int_0^{t_p} U_J^2(t) dt + \frac{1}{\rho} \int_0^{t^*} [p_{cl}(t) - p_\infty] dt \quad (5)$$

From this, it can be noted that the circulation of the vortex ring can be augmented by increasing the pressure at the nozzle exit plane. Similarly, the impulse imparted by the vortex ring has been

shown to be dependent on slug as well as NEOP effects, necessitating the addition of a pressure correction term, I_p , to account for pressure-induced impulse (Krueger and Gharib 2003):

$$I = I_U + I_p \quad (6)$$

in which the impulse imparted by NEOP can be expressed as:

$$I_p = \int_0^t \int_A [p_{cl} - p_\infty] dS dt \quad (7)$$

This equation also shows a direct propulsive benefit to overpressure at the nozzle exit plane. In their 2003 study, Krueger and Gharib showed that velocity profiles consisting of a faster acceleration yield a higher NEOP. Alternately, it may be stated that a right skew velocity profile, like that in Figure 10, will yield more pressure impulse than a similar left skew velocity profile.

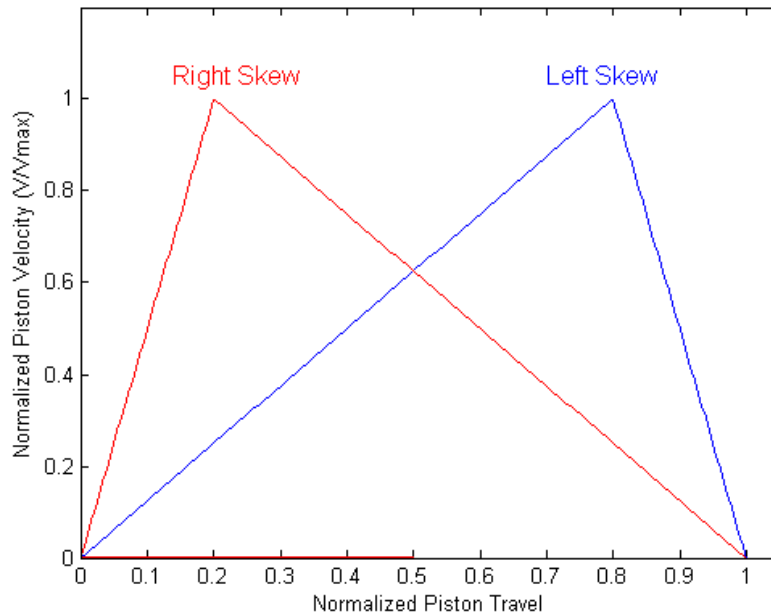


Figure 10. Velocity profiles of right and left skew

2 EXPERIMENTAL SETUP

The initial goal of this experiment was to assess the validity of the trends noted by Krueger and Gharib in 2003. This necessitated the design of a novel apparatus with a lower susceptibility to the nonlinearities and hysteretic effects inherent to that of the previous study. The resultant design allowed for more precise control of the piston velocity profile, but precluded the determination of thrust magnitudes.

A second goal was the evaluation of proprietary velocity profiles for signs of improvement in vortex creation over the profiles tested in previous studies. Specifically, an increase in the formation number over that of the original profiles was desired in the new profiles.

The final goal of this work was to study the effects of L/D and velocity profiles on vortex ring entrainment at Reynolds numbers in the hundreds, where no experimental data existed. Emphasis was placed on determining the formation number of each profile at these lower Reynolds numbers, and on observing the structure of the rings to assess any changes.

2.1 Vortex Ring Generator

The generation of a vortex ring in a fluid medium can be accomplished by means as simple as placing a droplet of negatively buoyant food coloring in water (Shariff and Leonard 1992). However, the repeatable generation of rings of a size and translational speed suitable for quantitative study necessitates the use of a more sophisticated apparatus with greater user control.

Recent studies (Kruger and Gharib 2003) have shown that a piston-cylinder apparatus can be used to generate vortex rings in water of varying size and vorticity. While these studies have produced encouraging results concerning the piston velocity profile dependence of vortex rings, the design of these apparatus has inhibited precise control of the piston at small stroke lengths, causing nonrepeatability and significant nonlinearity in piston velocity profiles. It has been

suggested that this nonrepeatability has been caused by the use of a free-floating piston, propelled using water pressure, vice a rigidly-coupled shaft. The apparatus designed for the present study attempted to correct this shortcoming, albeit at the expense of losing the ability to directly measure the thrust produced.

To further enhance the accuracy of the new results over those of the previous experiments, the exit of the nozzle for this study was enlarged by 400% over that used previously. First, this enlargement physically agitated more seed particles in the PIV interrogation region, thereby creating more possible vectors and improving resolution in the vector map. Second, the larger nozzle, and its concomitant increase in energy imparted to the working fluid, yielded greater displacement of the seed particles. This allowed the use of a larger spot size, improving vector accuracy. Additionally, it minimized the effects of any tank turbulence on vortex formation and propagation.

2.1.1 Piston

The current study utilized a shaft-driven machined aluminum piston. This piston had a diameter of 25.0 cm (9.8 inches) and was propelled through the use of a computer-controlled linear stepper motor. The piston was fitted with two rubber o-rings along its diameter to facilitate a watertight seal, and then seated in an aluminum cylinder which terminated in an aluminum contraction nozzle, as shown in Figure 11.

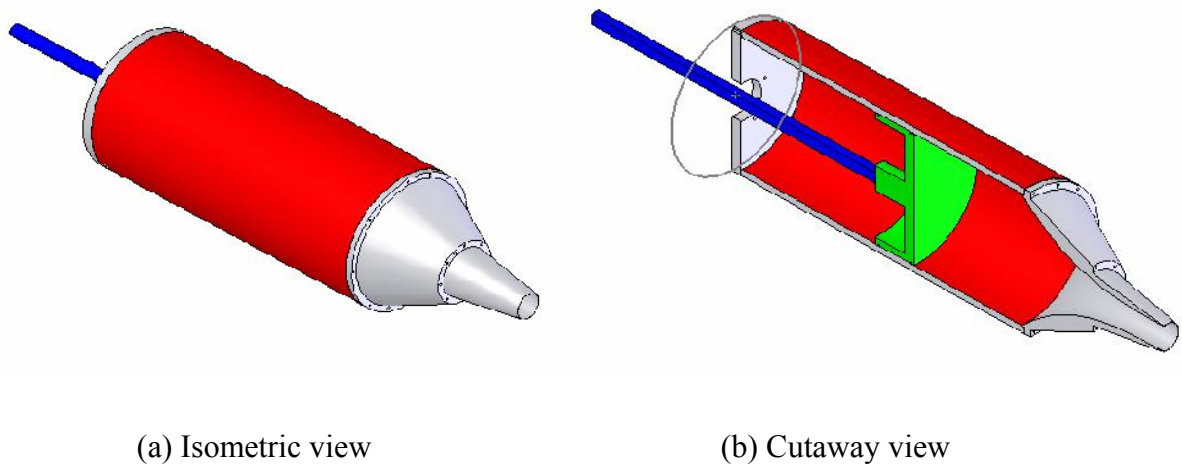


Figure 11. Design drawings of vortex generator apparatus

2.1.2 Nozzle

The nozzle utilized in this experiment was machined from a single aluminum billet and attached to the cylinder end using machine bolts and silicone caulk. The nozzle had an inlet diameter of 25 cm (9.8 in) and an exit diameter of 4.8 cm (1.9 in), yielding a contraction ratio of 23.4 to 1. The SOLIDWORKS drawing used to create this nozzle is shown in Figure 12.

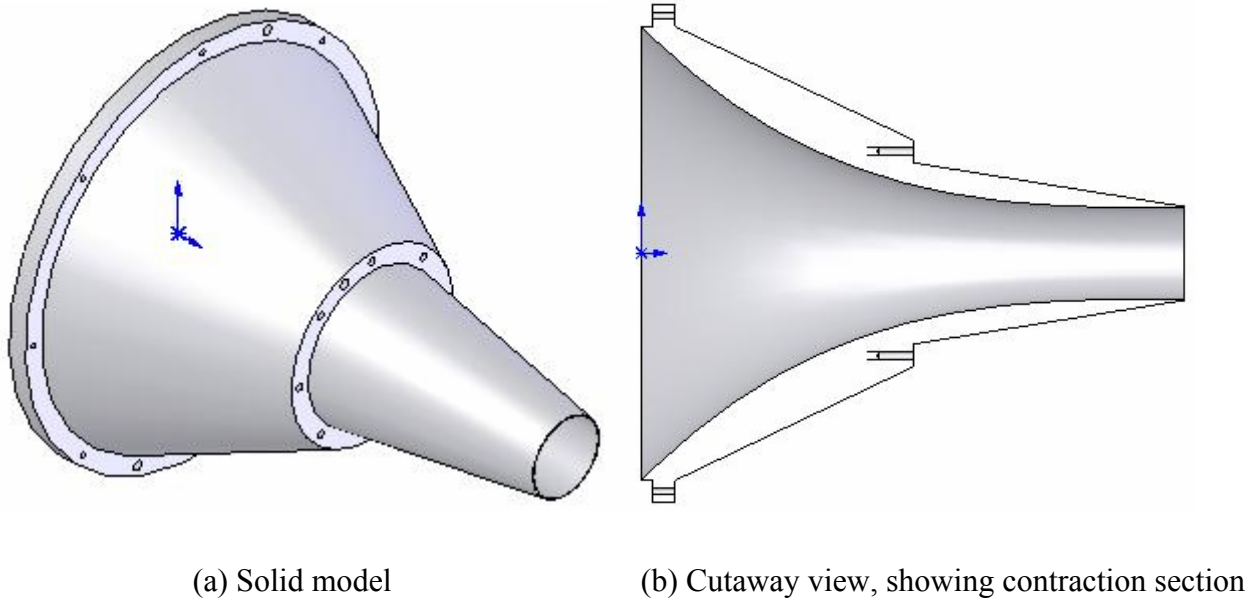


Figure 12. Design drawings of nozzle

The inside of the nozzle was machined via CNC with the quartic contraction curve given by Equation (8), and shown graphically in Figure 13.

$$y = 4.6000 - (1.1918)x + (1.4586 \times 10^{-1})x^2 - (7.9301 \times 10^{-3})x^3 + (1.6161 \times 10^{-4})x^4 \quad (8)$$

This curve allowed acceptable ease of manufacturing, while yielding a continuous flow contraction without inflection points. Additionally, this curve was created to ensure that at the termination of the contraction, velocity and acceleration in the lateral direction were zero, indicating that all exit flow was in a purely axial direction so as not to affect the formation of the vortex ring. The MATLAB script used to generate this curve is included in Appendix A: Contraction Curve Script.

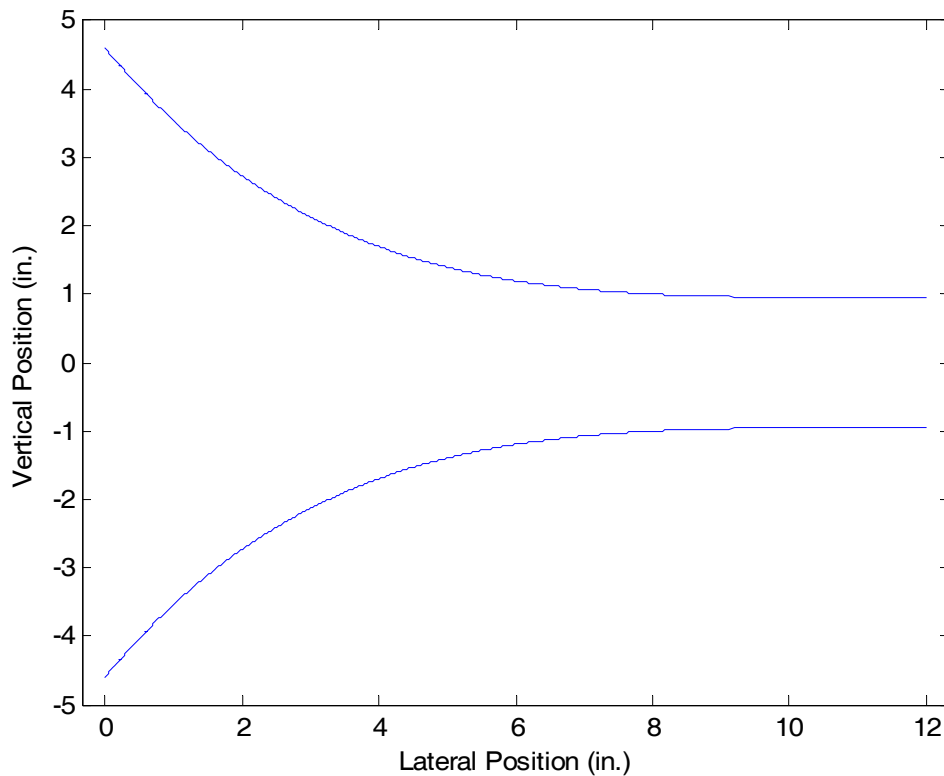


Figure 13. Contraction curve used to manufacture nozzle

2.1.3 Motor

Precise control of the piston was accomplished through the use of an Intelligent Motion Systems MDrive34 linear stepper motor. This motor had a screw rate of one half inch per revolution and a controller resolution of 51,200 micro-steps per revolution. The maximum linear force that could be supplied by the motor was 756 N (170 lbs), and the maximum torque available was 120 Nm (16992 oz-in). Maximum linear (shaft procession) speed was 38 cm/s (15 in/s). The MDrive was mounted to a custom mounting plate affixed to the rear of the cylinder using machine bolts and the manufacturer's suggested mounting holes, as shown in Figure 14.

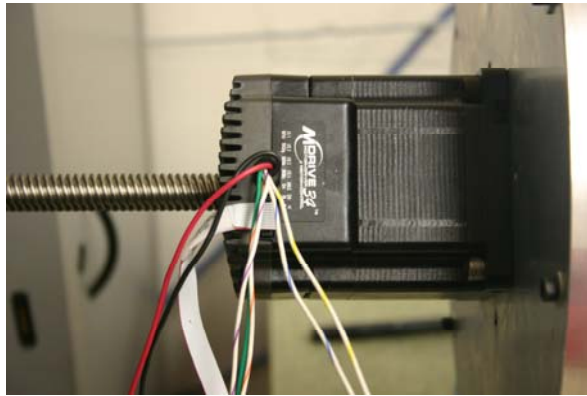
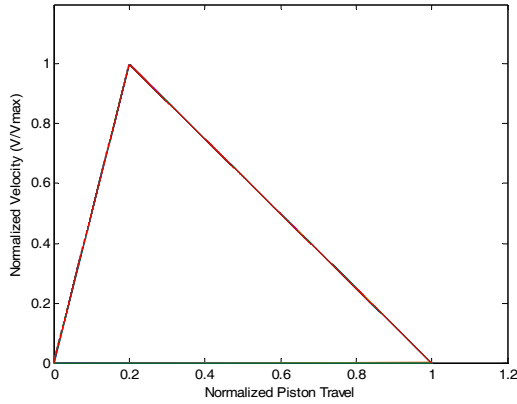


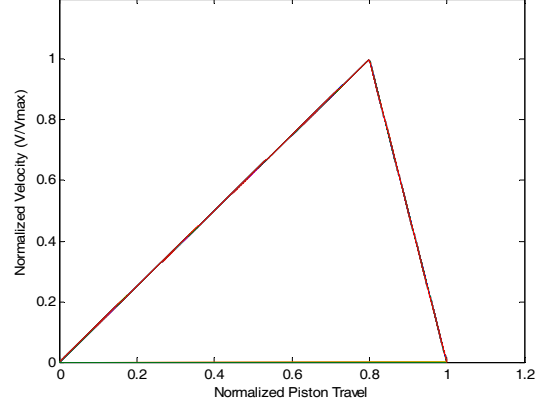
Figure 14. MDrive motor shown attached to mounting plate

2.1.3.1 Velocity Profiles

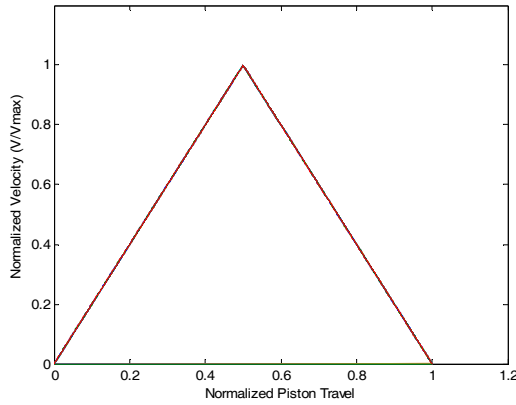
The precise, repeatable generation of desired velocity profiles was seminal to the execution of this study. The profiles utilized in earlier studies (Krueger and Gharib 2003) were modified to reflect a definitively positive, negative, and neutral skew. In this case, we use the term “skew” to denote the skewness of the distribution, as defined by the Pearson simplification to the definition of skewness, specifically $\gamma = \frac{3(\bar{x} - \tilde{x})}{\sigma}$. An impulsive profile, characterized by an acceleration to maximum piston velocity in 5% of the total piston travel distance, was also utilized. Plots of the four profiles examined in this experiment are shown in Figure 15.



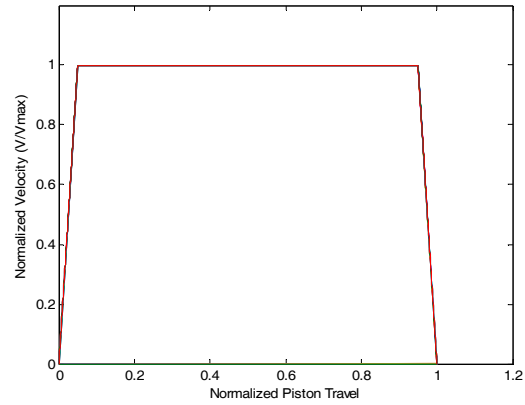
(a) Right skew



(b) Left skew



(c) Symmetrical



(d) Impulsive

Figure 15. Normalized velocity profiles

Each general profile shape (i.e., skew, acceleration and deceleration fractions, and maximum velocity) was input into the MATLAB script in Appendix B: Velocity Profile Generator Script, which converted the inputs to MDrive IMS Terminal parlance and plotted the profiles for visual verification of correctness. A sample plot of the L/D sweep of the right skew profile examined is shown in Figure 16.

At each Reynolds number, each profile was tested at $L/D=[2, 3, 4, 5, 6]$, in response to the pinch-off trends noted in earlier publications. The specific range of L/D examined for each profile was expanded beyond this initial survey, based on the observed behavior of each profile at each Reynolds number tested. These secondary L/D sweeps ranged in scope from $L/D=0.5$ to $L/D=20$, and are specified for each test case in subsequent sections of this report. Sample IMS Terminal programs used to execute these velocity profiles are included in Appendix C: Sample Velocity Profile.

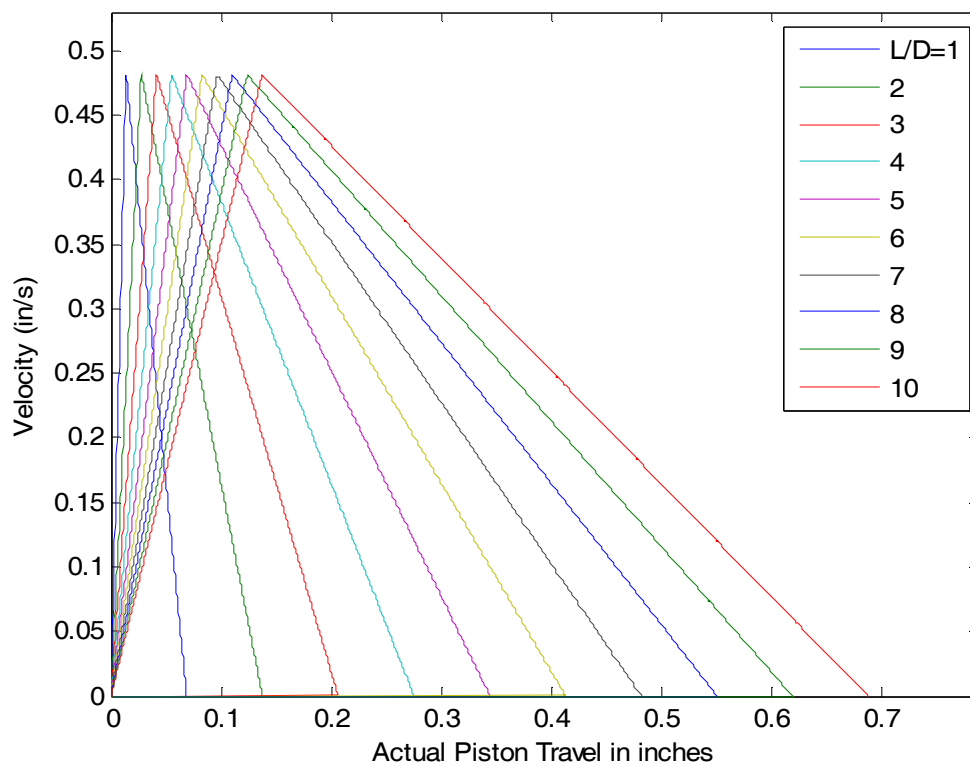


Figure 16. Sample graphical depiction of right skew velocity profiles for a range of L/D

2.1.3.2 Control

Control of the motor was accomplished using MDrive Plus IMS Terminal. Velocity profiles were composed in the IMS Terminal editor and uploaded individually to the MDrive34's controller card. Following the testing of each profile, it was removed from the MDrive's memory and

overwritten with a new velocity profile to prevent possible control algorithm contamination. The profile program for each velocity profile for is included in Appendix C: Sample Velocity Profile.

2.2 Testing Tank

All flow surveys in this study were conducted inside a glass and aluminum tank with a 50.8 x 50.8 x 101.6 cm (20 X 20 X 40 inch) test section. This tank had a front wall and side wall made of 0.5 inch plate glass to permit passage of the PIV laser and cameras. The aluminum base and sidewalls were covered with blue corrugated plastic tuned to absorb 532 nm wavelength light, which minimized the number of laser light reflections in the tank.

To compensate for the amount of fluid added to the tank test section with each piston pulse, a weir was incorporated into the tank design. This device extended the entire length of the tank to a height of 50.8 cm (20 in) and had an angled top edge, which facilitated the spillage of fluid from the test section of the tank into the spillway. Following testing and re-centering of the piston, the contents of the spillway were returned to the test section using a Thirsty Mate manual bilge pump, from Beckson Marine Incorporated.

Draining of the tank was accomplished through the use of a ball valve and sink-type drain in the base of the tank. This drain was placed directly beneath the back edge of the nozzle to prevent any interaction with the vortex rings. The assembled test apparatus is shown in Figure 17 below.

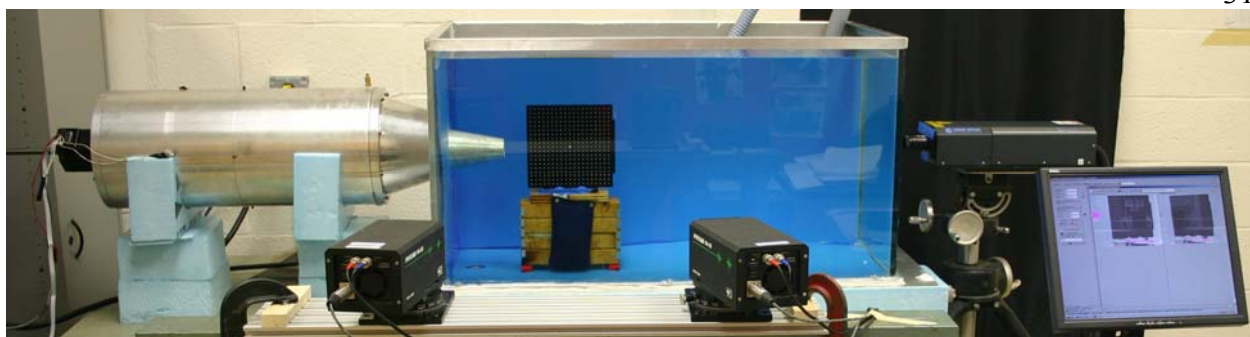


Figure 17. Fully-assembled test apparatus, with calibration target in place

2.3 Viscometer

A Brookfield Engineering dial-reading, low viscosity viscometer was utilized for viscosity measurements. Samples were placed in a 250 mL laboratory beaker and measured using Brookfield Low Viscosity Spindle #2. Two blind measurements were taken at each of five different spindle speeds and compared using a Microsoft Excel Spreadsheet. A picture of the viscometer and spindle is shown in Figure 18.



Figure 18. Viscometer with high-viscosity spindle attached

2.4 Stereoscopic Particle Image Velocimetry Setup

2.4.1 Background

Stereoscopic Particle Image Velocimetry (SPIV) is a quantitative flow visualization technique which permits the determination of fluid flow properties, such as velocity and vorticity, in three dimensions. This is accomplished by digitally dividing a flow region into a number of discrete elements and tracking the movement of particles inside each element over a known period of time.

2.4.2 Process

Small reflective particles must be suspended (or “seeded”) in the fluid flow of interest. In this study, Dantec Dynamics silver-coated hollow glass spheres (item number 80A7001) with a nominal diameter of 10 microns were uniformly distributed in the tank and cylinder. These particles travel with the fluid in the tank and while they are in motion, a pulsed laser illuminates them, and a collection of four digital images (a “capture”) is taken using a pair of high-speed digital cameras mounted non-orthogonally. Each camera takes two images in rapid succession, synchronized with the partner camera. The time step between these images is a known, user-programmable value, which varied from 800-1200 μs in this experiment.

TSI Incorporated’s Insight 3G computer image-processing software package was then used to “correlate” these images. Correlation was accomplished by examining each of the discrete regions of the flow field in each image pair in a capture (i.e., the two images from the same camera). The computer tracked the movements of groups of particles in each interrogation region and produced planar velocity vectors for each region. These planar vectors from each camera were then cross-correlated to produce the three dimensional velocity vectors, as shown in Figure 19. From these, quantities such as vorticity and momentum flux can be calculated.

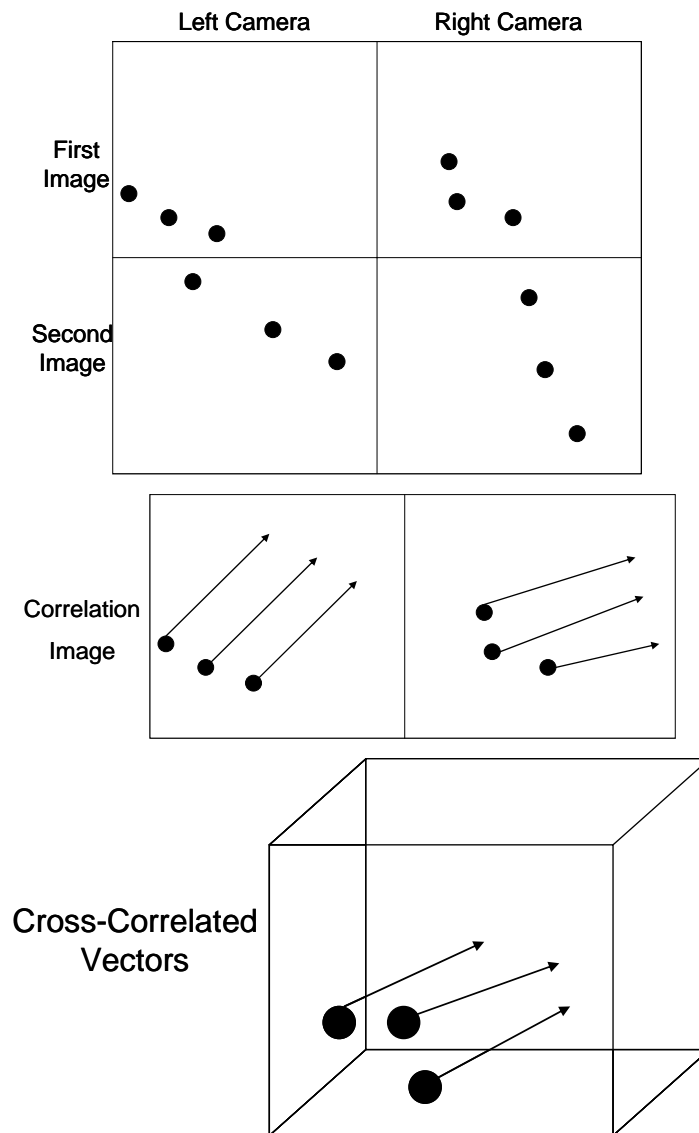


Figure 19. Simplified depiction of SPIV correlation

In order to complete this process successfully and produce accurate results, there are six accepted guidelines to follow. First, each grid element must be sufficiently small that the vector describes the motion within the spot. Second, the maximum allowable number of particles per spot is ten. Third, particles should not be displaced inside the plane by more than one quarter of the spot size. Fourth, the particles should not be displaced out of the plane by more than one quarter of the thickness of the light sheet. Fifth, particles must be displaced in the plane by at least two

diameters. Last, the exposure window must be sufficiently large so as to clearly show the particles.

2.4.3 Equipment

Two TSI, Inc. PIVCam 14-10 digital cameras were used in this study. Each had a 1374 x 1024 pixel resolution, with a maximum framerate of 10 Hz and a shutter open time of 255 μ s. Each camera used a 28mm Nikon lens with a 532 nm filter.

A New Wave research Solo 120 laser was used to illuminate the tank. This laser was a dual-head, 500 mJ, Nd:YAG laser with a flashlamp frequency of 15 Hz and a light wavelength of 532 nm.

The time step used for each capture was generally set at 1000 μ s, however, some tests necessitated the use of time steps as short as 800 μ s and others required steps as long as 1400 μ s. The pulse repetition rate was set at 3.63 Hz and the Q-switch delay was held constant at 250 μ s, which was the minimum allowable for the laser on the high power setting.

2.4.4 Calibration

Calibration of the SPIV system was accomplished through the use of the TSI model 640010-4P PIV Calibration target. This target was used because of its relatively large size which encompassed most of the interrogation region in the tank. This target is comprised of a matrix of circular white dots spaced 10 mm apart in the horizontal and vertical directions, with the dots on each positively-sloped diagonal (i.e., lines going from lower left to upper right) offset by an out of plane distance of 1.0 mm. This three-axis positional difference between dots permitted a three axis calibration of the laser and camera system, which is necessary for the resolution of velocity components in the principal three orthogonal planes. Also on the face of this target was a large cross, called the “Fiducial Point,” in the center of the target. This point was aligned with the centers of the camera lenses and the laser prior to the capturing of calibration data. A picture of this target, mounted on its custom-made base, is shown in Figure 20.

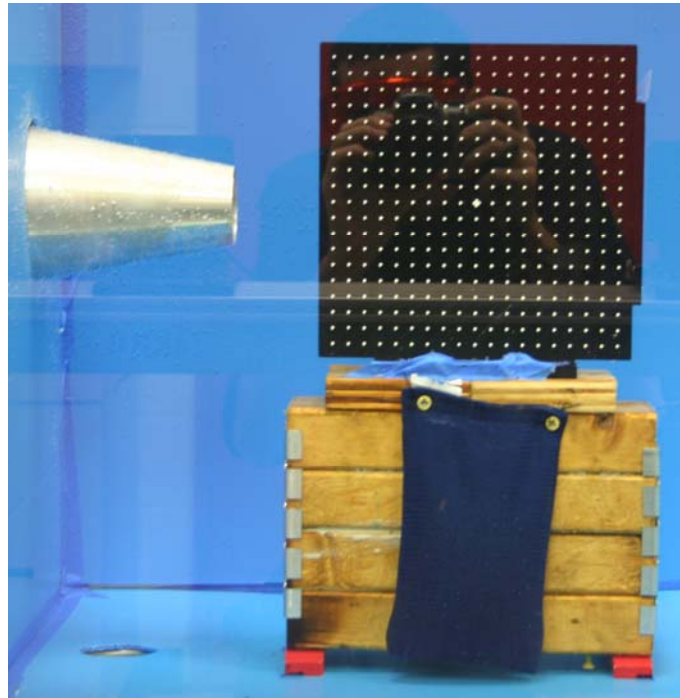


Figure 20. Calibration target positioned on base, in interrogation region

The target was coarsely positioned in the region of interest using a tape measure, and then the position was refined using the alignment mirror affixed to the edge of target facing the laser aperture. The target was moved until the mirror split the laser light sheet and reflected the laser light back onto the center of the laser aperture. The positioning of the mirror and laser is shown in Figure 21.

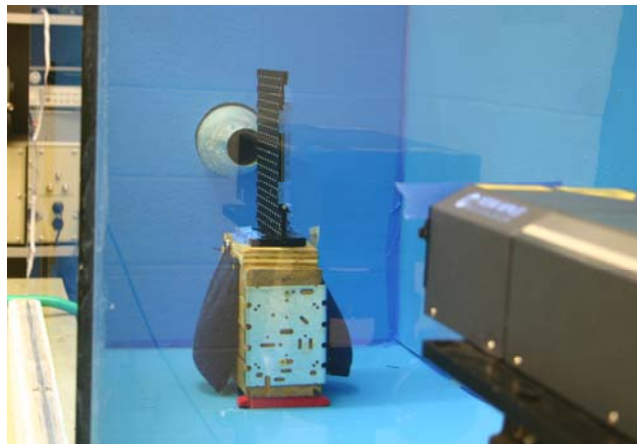


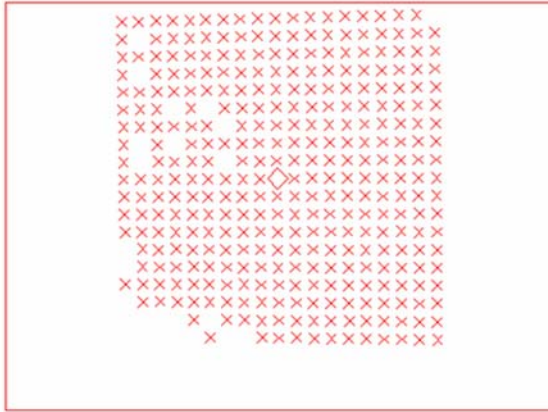
Figure 21. Calibration target in place, showing orientation of mirror and laser

Following this, the cameras were positioned with a 25 degree angle between their lines of sight and focused on the fiducial point. The line of sight angle and the elevation angle of each camera was then adjusted to position the crosshairs of the camera directly over the fiducial point. This resulted in a line of sight angle of 26.0 degrees between the cameras. The cameras were then re-focused through a process of bracketing the focus point with incrementally smaller focus regions. An overhead view of the final camera positions on the mounting rail is shown in Figure 22.

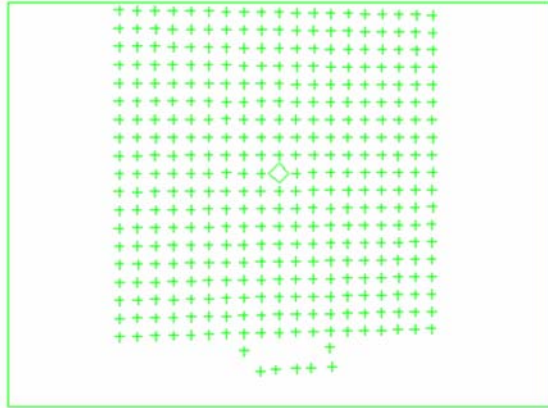


Figure 22. Final camera mounting positions

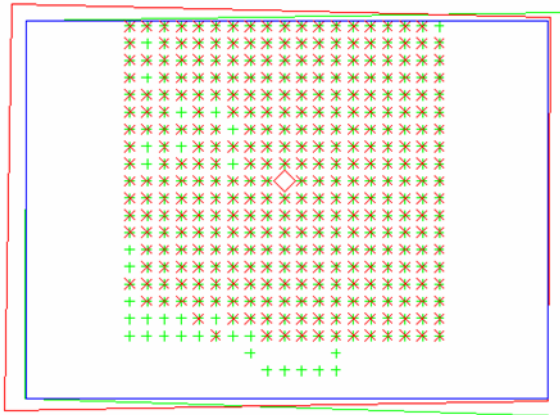
Following camera alignment, a series of images of the calibration target were taken from each camera. The calibration processor in Insight 3G located the fiducial point in the images and used a correlation algorithm to build a three-dimensional coordinate grid in the interrogation region, thereby permitting the determination of position and velocity data for particles in the flow field. Example images of the grid defined for tests conducted in water are shown in Figure 23.



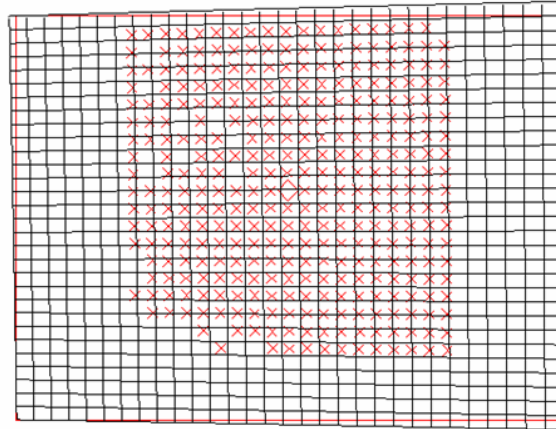
(a) Left camera calibration points



(b) Right camera calibration points



(c) Calibration points in three plane correlation



(d) Calibration grid, on left camera field of view

Figure 23. Processed calibration images, showing grid definition

2.5 Experimental Method

The fluid in the tank was seeded until acceptable image captures could be taken (approximately 10 g of particles, for tests in water) and motion was allowed to settle to a quiescent state. Prior to testing, a pair of 300 mL samples of tank fluid was collected using a mouth pipette, one from the top of the right front corner and one from the bottom of the left rear corner. Tank motion was allowed to settle and the fluid temperature was measured via an installed alcohol thermometer. The motor was then triggered using a Sony VAIO laptop equipped with MSterm. The cameras

and the laser were initiated by a TTL pulse emitted by the motor upon initiation of piston motion. A trigger delay was then activated through Insight 3G and upon completion of the delay time, the synchronizer triggered the camera and laser capture sequence. A delay time of 0.001 second was utilized for runs where ring inception data was desired, while a delay time of 1.5 seconds was used for runs where only late-stage data was desired. The images were captured using a Dell desktop PC running Insight 3G. Data from each run was then moved from RAM to the computer's hard disk. Motion in the tank was allowed to settle for an additional 30-40 seconds, and the process was repeated for all L/D desired, and each of the four velocity profiles previously stated. Following completion of PIV data collection, a second pair of fluid samples was collected in the same manner as the earlier set, along with a second temperature measurement.

2.5.1 Viscosity Measurement

The viscosity of each of the fluid samples was measured using the viscometer and recorded in a Microsoft Excel spreadsheet. Prior to testing, if the two samples exhibited a difference in viscosity greater than 1%, the tank was re-mixed using a series of long-stroke piston movements and cordless drill with paint mixer attachment. Viscosity measurements were then repeated, until the desired tolerances were satisfied. The viscosity of samples collected after testing were determined in the same manner, and compared with measurements taken prior to testing. In practice, differences in viscosity measurements taken before and after testing were always found to be within 0.5% of total viscosity.

2.5.2 Capture Timing

Initial trials in water were collected using 20 captures per piston movement, which presented a time history of the vortex from the zero fluid motion stage to the exit of the interrogation region. However, following collection of data for approximately 150 runs, a frame synchronization discrepancy was noted between captures in successive runs (i.e., corresponding captures in subsequent runs were observed to lag their counterpart from earlier runs). Attempts to remedy this problem in software and hardware proved unsuccessful, so subsequent runs were cataloged

using a longer trigger delay and only 4 captures per fluid shot. The longer delay permitted the ring to propagate down the tank to the specific region of interest, $0.05 < x/D < 6.61$, where the entirety of the primary vortex ring and any trailing jet could be observed. These delays are summarized in Table 1.

Table 1. Ranges of time delays utilized

Glycerin Percentage	Time Delay (ms)
0	1800-2800
60	1500-3200
70	2000-3500
80	1000-8500

Of critical importance to obtaining high-fidelity SPIV data was tuning to the appropriate time step between successive capture images, Δt . The preferred value of Δt was found to increase in duration as glycerin concentration increased. The values of Δt used for each glycerin concentration are shown in Table 2 below.

Table 2. Time steps used to obtain captures in test solutions

Glycerin Percentage	Δt (ms)
0	1000
60	1200
70	1300
80	1500

Following successful collection of data, a series of captures were collected using 10 captures per fluid shot, cataloguing the motion from quiescence to frame exodus. Again, frame slippage was sporadically noted in some captures, but was found to be equivalent to a delay of one single

frame. These sequences were formed into digital movies, for analysis and capture timing purposes.

2.5.3 Image Processing

Insight 3G was used to process the image captures and produce 2-D and 3-D vector fields, through a process known as recursive grid processing. All images were processed using a series of four aggressive filters to eliminate erroneous vectors. First, a standard deviation filter compared each vector with counterparts in the same 5 x 5 pixel neighborhood, and discarded any vectors which differed from neighbors by more than three standard deviations. Next, a median filter removed any vectors which differed from the local median by more than a tolerance of 2. The final filter used was a mean filter which eliminated vectors which differed from the local mean by more than a tolerance of 2. A recursive Nyquist grid engine was used to process the images, first with a 32 X 32 pixel spot size, then with a 16 X 16 pixel spot size. A fast Fourier transform correlation engine was used for the correlation mathematics and the Gaussian Peak engine was used to optimize the peak to noise ratio. The product of this data processing was a three-dimensional vector file (V3D file) for each capture.

The V3D files from each capture were then averaged with corresponding captures from other runs through a process known as ensemble averaging. Through this process, corresponding vectors in corresponding captures were averaged, which further minimized the impact of erroneous vectors and greatly reduced the number of vector dropouts, or missing vectors, in the data. The final stage of this averaging routine took the ensemble averaged data and interpolated values for any pixels with missing vectors. This was accomplished using the MATLAB script in Appendix D: Ensemble Averaging Script.

An integral part of this process was the visual examination of the color flood plots of the averaged u, v, w, and vector count data, prior to application of the interpolation algorithm. Each plot was examined to verify that vector dropout had not occurred in a region where its presence would adversely affect the conclusions drawn from the data, and to ensure that the vector dropouts were singular entities and did not constitute large, concentrated regions of the vector

fields. Following fulfillment of these criteria, the interpolation routine was used to generate logical vectors to replace the few areas where the PIV vectors had been dropped.

The output of this averaging and interpolation routine was saved to a V3S file, which was then processed to determine vorticity contours. The MATLAB script used to determine these contours is included in Appendix E: Vorticity Contour Generator Script. This script was designed to display all discernible contours for the entire interrogation region in one figure, and close-up views of the ring vortex and trailing jet (if applicable) in additional figures. These latter figures excluded the lowest vorticity levels, for clarity purposes. All figures were computed and displayed using a common color bar, to facilitate rapid comparison of data from different runs.

2.5.4 Recursion

Following image analysis, the L/D sweep was refined to bracket the observed pinch-off L/D for each profile in the 0% glycerin and 80% glycerin runs. New MDRIVE code for each of the previously-examined profile shapes was generated with an appropriate L/D step size. Table 3 below summarizes the ranges of refined L/D examined for each profile in pure water (0% glycerin solution).

Table 3. L/D ratios examined in secondary sweep in pure water

Profile	L/D
Right	3.4
	3.6
	3.8
Left	4.5
	4.7
	4.9
Symmetrical	5.7
	5.9
	6.1
Impulsive	6.2
	6.4
	6.6
	6.8

The specific data-collection and reduction process employed in this second sweep was nearly identical to that outlined in the previous sections. The primary difference was the use of an altered delay time of between 1.8 and 3.6 s, which was found to better facilitate the capturing of images throughout the specific region of interest outlined above.

2.6 Reduced Reynolds Number Regimes

Data collection in lower Reynolds number regimes was accomplished by changing the working fluid in the testing apparatus to dilute glycerin solutions. Aqueous solutions of 80%, 70%, and 60% glycerin concentration were alternately used, which when employed with the same velocity programs used in the water trials, allowed testing at Re of 250, 780, and 1,500, due to the elevated kinematic viscosities of the glycerin solutions. Additionally, the seeding was adjusted to maximize the peak to noise ratio of the vector images.

For each new solution, a complete calibration was performed, as outlined previously.

2.6.1 Kinematic Viscosity Determination

The viscosity of the glycerin was measured using the Brookfield viscometer. A set of five measurements was taken of every sample, using Brookfield spindle number 2 over a range of spindle speed settings. The resulting measurements were recorded in an Excel Spreadsheet and the mean average of the five viscosity measurements was used for subsequent dilution and Re calculations.

The density of the glycerin was determined by weighing 500 mL of each of the glycerin solutions in a Pyrex beaker. The weight of the beaker was subtracted to get the weight of the glycerin, which was then divided by the 500 mL volume of glycerin weighed. By dividing this measurement into the viscosity measurement taken previously, the kinematic viscosity of each solution was determined, as indicated in the equation below.

$$\nu = \frac{\mu}{\rho} \quad (9)$$

The temperature of each solution was also recorded, which allowed for comparison of viscosity measurements to published temperature-viscosity charts furnished by Dow Chemical Corporation. It was determined that experimental measurements agreed with published data to within 2 percent.

2.6.2 Solution Mixing

The test tank was filled from a 55 gallon drum of glycerin using the Thirsty Mate™ pump. The amount of water to be added to each quantity of glycerin was measured and placed in a plastic carboy in the laboratory space two hours prior to mixing the fluids, to allow the glycerin and water to reach thermal equilibrium. After pumping approximately fifteen gallons of glycerin into

the tank, one quarter of the water to be added was poured into the tank. This was repeated until all of the glycerin and water had been added to the tank.

Ten grams of seeding particles were added to the solution and it was mixed in the tank for thirty minutes. Mixing was accomplished by the combined use of an MDrive program which cycled the piston from bottom dead center to top dead center hundreds of times. This program is included in Appendix F: Tank Mixing Script. Concurrently, a Makita cordless drill and an 18 inch aluminum paint mixer were used to ensure the glycerin and water was thoroughly mixed.

Using a siphon, one 300 mL sample of the tank solution was taken from the upper front corner of the tank and another sample was taken from the lower back corner of the tank. The viscosities of both samples were measured according to the process described above, and the disparity was found to be less than 0.5%, which was taken to indicate thorough mixing.

2.6.3 Humidity and Viscosity Effects

The hygroscopicity of glycerin poses an inherent challenge to any research with this substance, especially to research dependent on precise viscosity measurements. User-defined humidity control was not possible in the test facility, so an experiment was conducted to observe the effects of the ambient humidity on the glycerin solution in the tank.

The surface area to volume ratio of the test tank was 1:20 inches, which was replicated through the use of a 250 mL Pyrex graduated cylinder with a surface area to volume ratio of 1:13 inches. This was filled with the mixed glycerin solution and left uncovered in the test environment for three days, at which time viscosity measurements were taken. The kinematic viscosity was observed to decrease less than 3% over this time period, effectively dictating that hygroscopic effects could be neglected over the proposed testing time.

As a control check, the kinematic viscosity of the tank fluid was measured using the aforementioned capturing process prior to each data capturing session. These measurements

indicated negligible change in the kinematic viscosity of the fluid, as evidenced by the table of measurements shown in Table 4 below.

Table 4. Daily viscosity and Reynolds number measurements taken for 80% glycerin solution

Day	Kinematic Viscosity ($\frac{in^2}{s}$)	Reynolds Number
1	0.0923	245.4
2	0.0901	251.3
3	0.0898	252.2

2.6.4 Viscosity Similarity

The Andrade-Eyring equation models the temperature variation in viscosity as:

$$\mu = K_2 e^{E_n/RT} \quad (10)$$

where E_n is the molar free energy of activation in the stationary fluid, R is the molar gas constant, and K_2 is a constant. Though derived for gases, this equation applies to the viscosity behavior of Newtonian and non-Newtonian liquids as well (Bird 28). Therefore, the viscosity can be written as:

$$\log \mu = \frac{1}{T} \log e^{E_n/R} + \log K_2 = K_3 \frac{1}{T} + K_4 \quad (11)$$

and the constants K_3 and K_4 are determined by a curve-fitting algorithm. To achieve temperature similarity in viscosity, the viscosity at some temperature, $\mu(T)$ is shifted to a reference temperature, T_{ref} (in this case $T_{ref} = 20^\circ\text{C} = 293\text{K}$). Thus:

$$\frac{\mu_{ref}}{\mu} = \frac{K_2 e^{E_n/RT_{ref}}}{K_2 e^{E_n/RT}} = e^{\frac{E_n}{R} \left(\frac{1}{T_{ref}} - \frac{1}{T} \right)} \quad (12)$$

But $K_3 = \log e^{E_n/R}$, so $e^{E_n/R} = 10^{K_3}$ indicating that the shifted viscosity can be calculated as:

$$\mu_{ref} = \mu(T) \cdot 10^{K_3 \left(\frac{1}{T_{ref}} - \frac{1}{T} \right)} \quad (13)$$

For Newtonian fluids, μ_{ref} will be constant. Note that the only constant needed for the shift is the slope K_3 and not the offset K_4 . This means that small variations in the magnitude of the viscosity (via a few percent in concentration changes, etc.) are not significant. For aqueous solutions of glycerin over 60-80% concentration, the value of K_3 varies from 1,520 to 2,129 K, as shown in Figure 24. Thus, viscosity values at different temperatures can be compared quantitatively if the concentration has not changed appreciably between measurements.

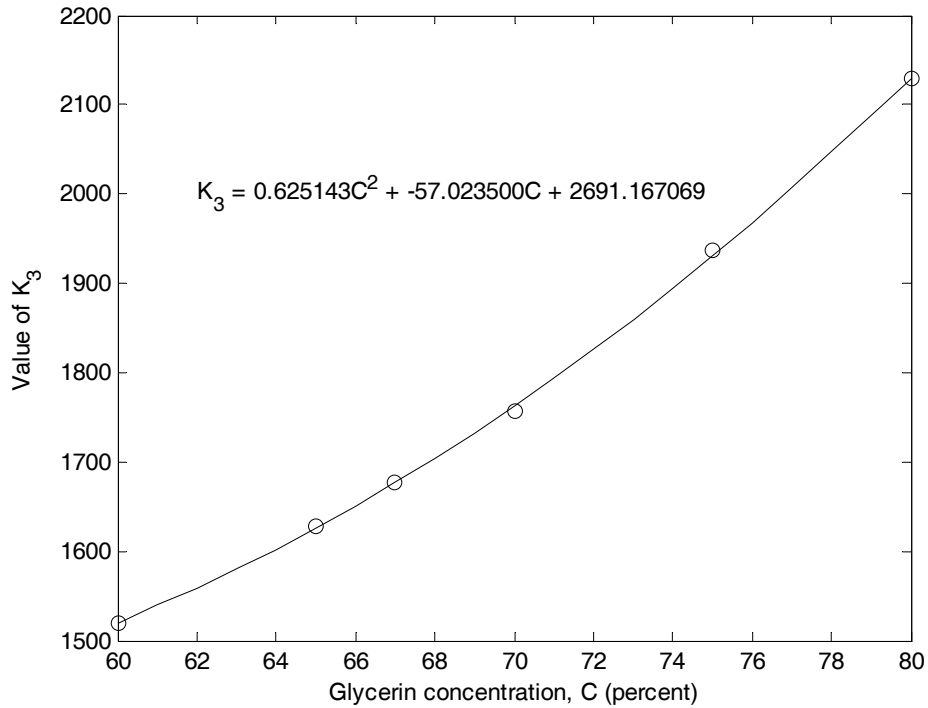


Figure 24. Plot of K_3 variation with glycerin concentration

3 RESULTS

Data were processed using Insight 3G and the criteria explained previously. The data were then ensemble averaged with corresponding data to minimize the number of vector drop-outs in the captures. Plots were generated of the three velocity components, the vector counts, and the vorticities using MATLAB.

3.1 Vector Dropout

Vector dropout is a phenomenon inherent to PIV research. Chief among the accepted schemes for minimizing its effects is ensemble averaging, wherein corresponding captures from different runs are essentially overlaid and the “holes” in each are filled with vectors captured during another run. This process was used in this experiment solely to enhance the visual appeal of the images and to ensure accuracy. In all captures, both the wake region and the vortex core(s) were found to have sufficient vector characterization to facilitate any investigations necessary for pinch-off determinations, even prior to averaging. The remaining dropout regions in some captures are likely caused by the small number of runs completed at certain test combinations of L/D and velocity profile. Capturing a larger number of runs at each test condition would improve this noticeably, but would also considerably increase data collection and processing times.

3.2 Velocity Profile and Vorticity Production

The close agreement of many of the results of this study with those of other studies has brought credence to the proprietary results. However, the nature of these new results seems to contradict the previously established theoretical model for the pinch-off mechanism. A possible modification to this model could be that the profiles with elevated initial velocity gradients produce more vorticity in the earliest stages of ring formation, as the shear layer separates from the nozzle lip. While the shapes of the profiles remained constant in the non-dimensional form (i.e., geometrically similar profiles), their specific acceleration velocity gradients were reduced as L/D was increased, as can be seen in Figure 16. These velocity gradients produce less initial

vorticity, and hence circulation, thereby reducing the vortex ring's ability to entrain fluid. The result is pinch-off at notably higher L/D values. Similarly, the profile shapes with the highest velocity gradients during the acceleration phase, such as impulse and left skew, produce more vorticity than their flatter counterparts. A possible way to test this specific explanation would be to create velocity profiles with the exact same acceleration phase and change the length and slope of the deceleration portion to achieve higher L/D . If the vorticity creation speed is truly the driving factor, pinch-off should occur at identical L/D , independent of the shape of the end of the profile.

3.3 Pinch-Off

The conventional definition of pinch-off as the point in time when the jet is no longer able to adequately supply energy to the vortex ring as it propagates away from the nozzle is a simple concept to evaluate mathematically and to demonstrate in analytical cases (Shusser and Gharib 2000). However, a clear criterion to determine and define this process in an experimental setting has not been established on any wide scale in the corpus of vortex ring literature. Krueger and Gharib (2003) use the standard that pinch-off has occurred when there is a turbulent structure in the wake of the vortex ring whose vorticity contours are at least equal in magnitude to that of the widest contour inside the primary vortex bubble. However, this standard is far from universal and leaves considerable room for interpretation and human judgment regarding the precise determination of the onset of pinch-off.

A novel criterion, complementary to those used in earlier research, has been used for determination of pinch-off in this study. This standard is threefold. The first is based on the knowledge that immediately following pinch-off, the separation of the trailing jet creates a vortex that is smaller and slower than the initial ring (Krueger and Gharib 2005). This first criterion is, therefore, the presence of a vortex aft of the main vortex bubble. The detection of the presence of this secondary vortex is accomplished by examining a plot of velocity components in the y , or vertical, direction. The circular motion of fluid in the vortex yields the characteristic pattern of alternating regions of v components with identical magnitude, but opposite (i.e. positive and negative) directionality, as shown in Figure 25. This figure is an ensemble average

of 10 frames from different runs of a left skew velocity profile at $L/D=10$. This L/D ratio is more than twice as large as any predicted or experimentally determined formation number for a left skew profile, so it clearly reflects an aggravated pinch-off state, wherein the nozzle jet is continuing to drive the secondary vortex, increasing its size and velocity. In this figure, the rightmost pattern of vortical motion is that of the primary vortex ring, while the smaller pattern in the wake of this vortex is the secondary vortex. It is the presence of this secondary vortex which is used as an indicator of the occurrence of pinch-off.

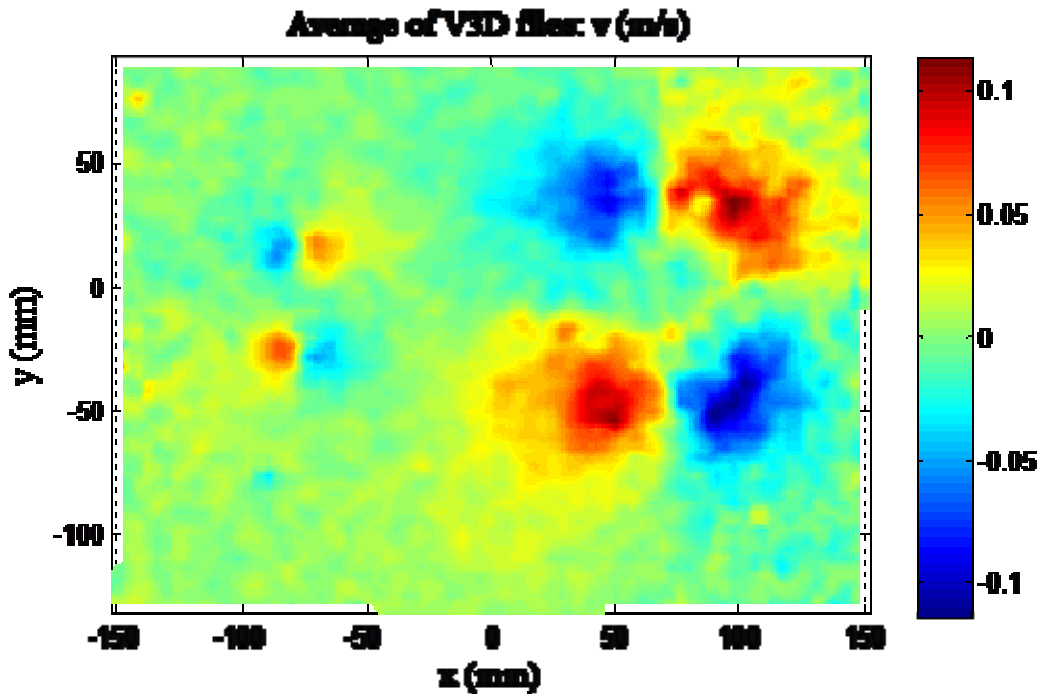


Figure 25. Vertical velocity component plot for a pinched off vortex ring

The second criterion for vortex pinch-off is the presence of a concentrated region of elevated u velocity outside the primary vortex bubble, but in the primary vortex's wake. The specific size of the region has been observed in this study and others (e.g., Krueger and Gharib 2003) to be dependent on the velocity profile and the extent to which the piston is attempting to drive the ring after the occurrence of pinch-off (i.e., L/D much larger than f_n). However, the u velocity component of this region is a value which was observed in this study to approach arbitrarily close to that of the vortex bubble with increasing L/D margin over pinch-off. Deriving its

velocity in part from energized fluid sheared away from the primary vortex ring and partially from fluid ejected through the nozzle which was unable to meet the primary vortex. This combination yields a region of velocity in the transverse, x , direction whose peak u component is at least 30% of the peak u component of the primary vortex. Because vortex ring dynamics are dominated by viscous effects and the process of pinch-off is not an instantaneous, stepwise process, in practice, concentrated regions of increased translational velocity may be noted in the wake of rings driven at L/D much less than the formation number. These cases have been observed to consistently fail to fulfill the 30% peak velocity requirement. Contrarily, known cases of pinched off vortices have been observed, in this experiment and others, to universally meet this requirement, and generally, exceed by a margin of nearly 100% (Alkislar et al. 2005).

A series of u velocity maps for increasing L/D is shown in Figure 26. In frames (a) and (b), the motion in the wake is below the 30% threshold value required for pinch-off. However, in frame (c), there is a clear indication of the presence of a trailing jet and satisfaction of this criterion for pinch-off.

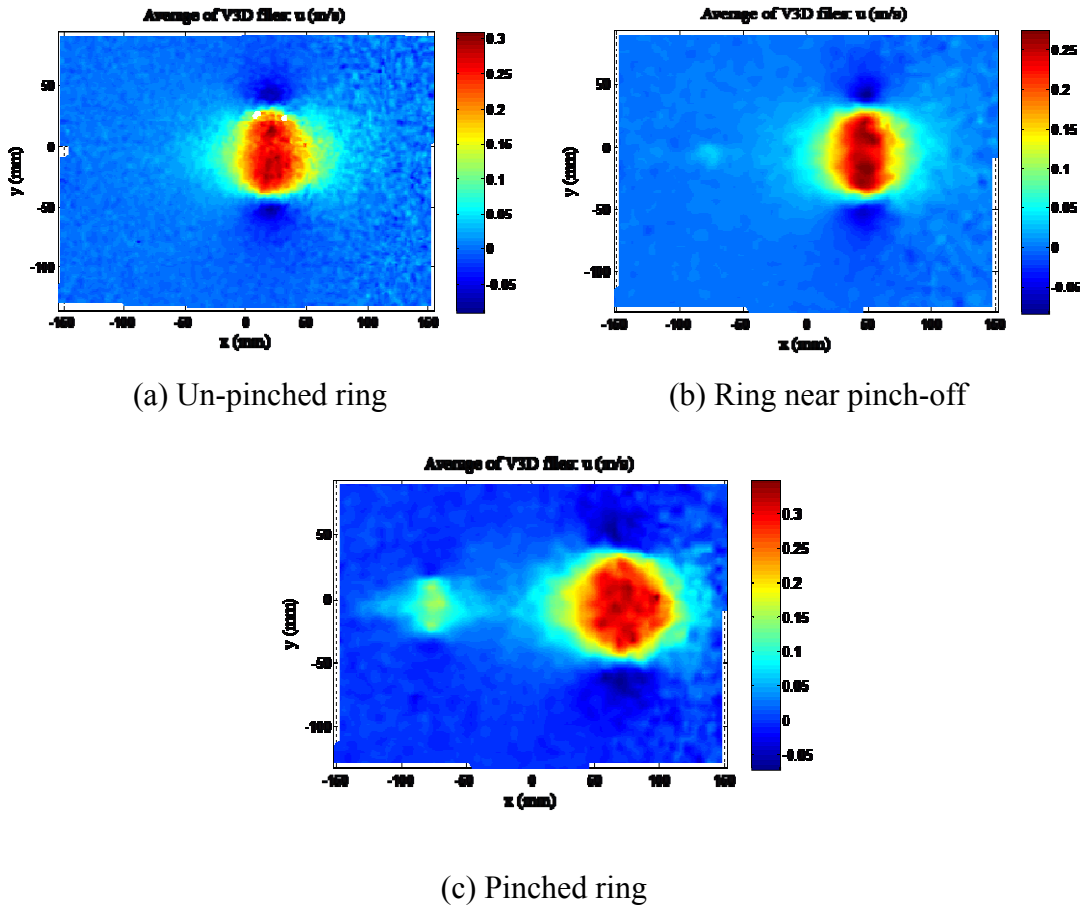


Figure 26. Translational velocity component maps for rings of various proximity to pinch-off

The final criterion used for the determination of pinch-off is dependent on an assessment of the vorticity distribution, both in the primary vortex and its wake. In keeping with the criterion utilized by Krueger and Gharib in 2005, a developed trailing jet must possess a vorticity contour greater than or equal to the magnitude of the weakest contour in the primary vortex core. In order to more fully standardize the determination of the point of vortex ring pinch-off, two additional sub-criteria were assessed in this research. First, a trailing jet must demonstrate the presence of bi-directional vortex cores in the wake of the primary vortex ring. These indicate the presence of a vortex ring, as opposed to that of simple eddy currents induced by the shifting of molecules in the test tank. Second, a trailing secondary vortex must be a concentrated, coherent structure exhibiting the characteristic vorticity cores of a vortex ring. This ensures that the vortical

structures observed are, in fact, part of a pinch-off-induced secondary vortex, rather than mere masses of vorticity shed in the wake of the primary vortex. A strongly-defined example of a vorticity plot showing a primary vortex followed by a well-developed trailing jet is shown in Figure 27.

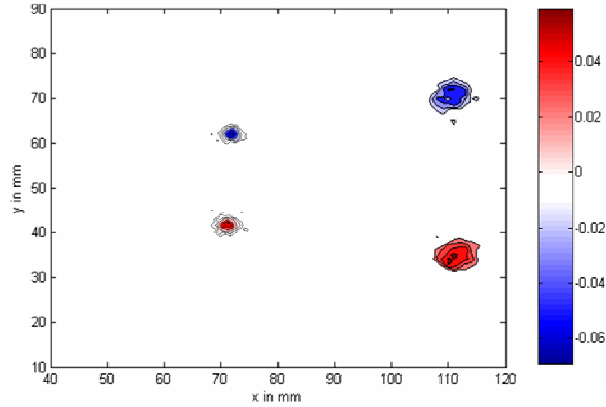
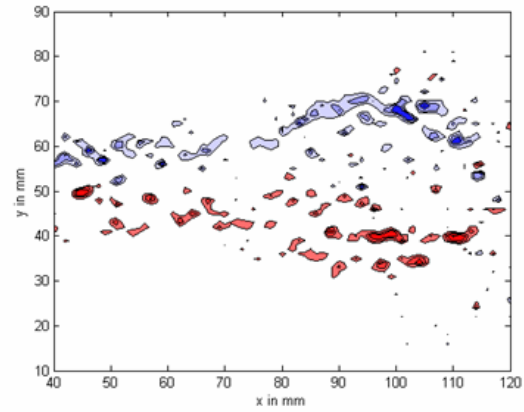
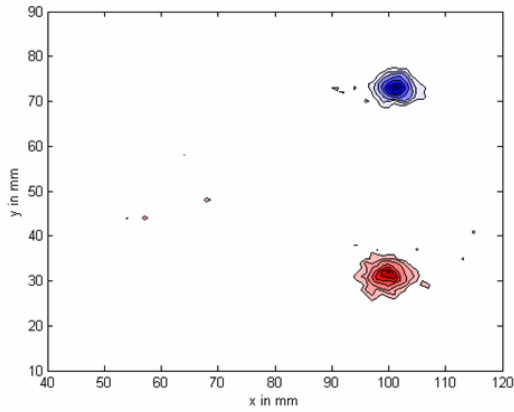
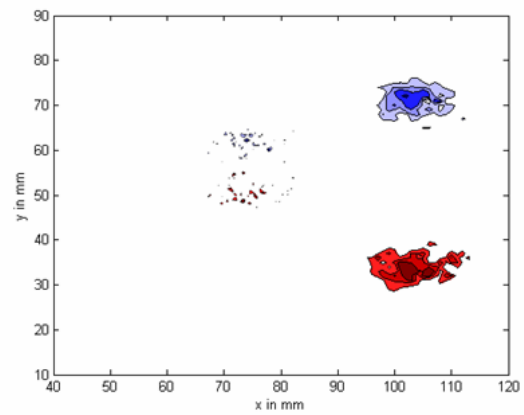
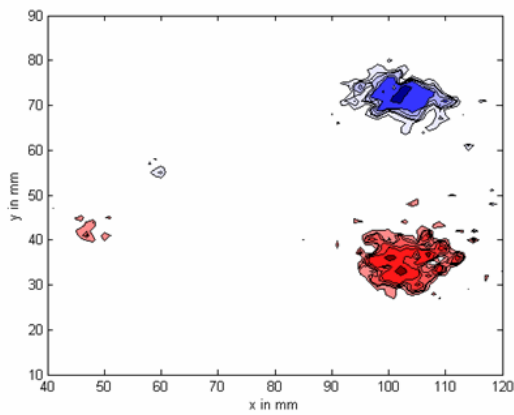


Figure 27. Vorticity contour plot showing primary and secondary vortices

The utility of all of the aforementioned vorticity criteria in the determination of pinch-off is demonstrated in the frames of Figure 28. For ease of comparison, all vorticity plots shown use the colorbar shown in Figure 27. In frame (a), vorticity meeting the canonical magnitude criterion is noted in the wake of the primary vortex; however, this is clearly not a trailing vortex and fails to be deemed as such, based on the bi-directionality criterion. Frame (b) also fails to satisfy the criteria to be considered a trailing jet, as the vorticity in the wake of the primary vortex is widely-distributed in a pattern radically different from that of a vortex ring. In contrast, frame (c) shows a pair of vortical masses which, although slightly displaced axially, meet all criteria to be considered cores of a trailing vortex. Thus, this is categorized as a weak trailing jet, indicative of a jet formed by a pulse of a size in close proximity to the formation number. In frame (d), the vorticity noted in the wake is significantly dispersed, yet still clearly contained in well-defined, symmetrical regions. This structure, too, is determined to be a trailing jet, and therefore indicative of pinch-off.



(a) Vortex ring with minute vorticity in wake (b) Vortex ring with extensive vorticity shedding



(c) Vortex ring with weak trailing jet (d) Vortex ring, with minimally-coherent trailing jet

Figure 28. Vortex contour plots with trailing vortices of varying levels of development

3.4 Results at $Re=13,000$

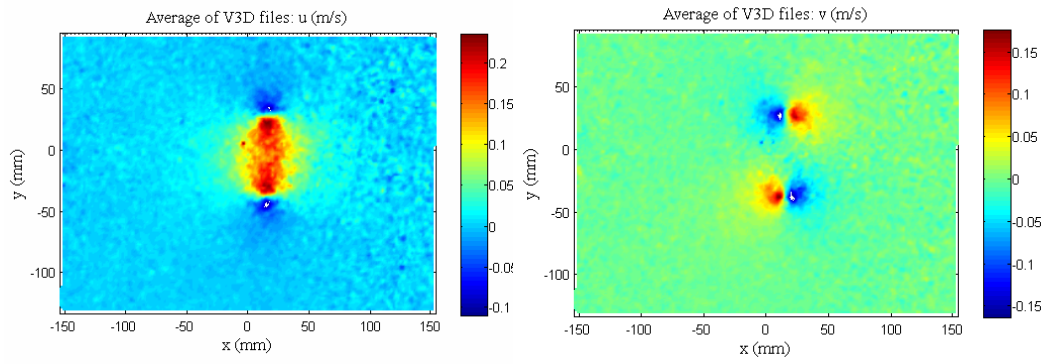
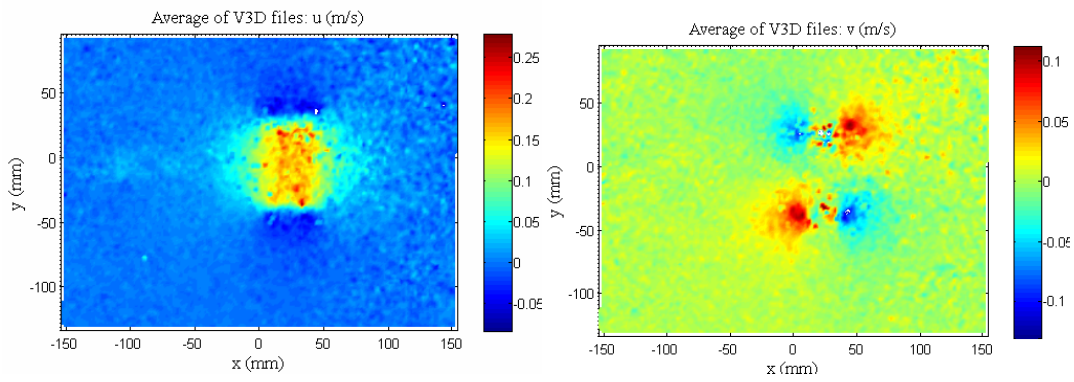
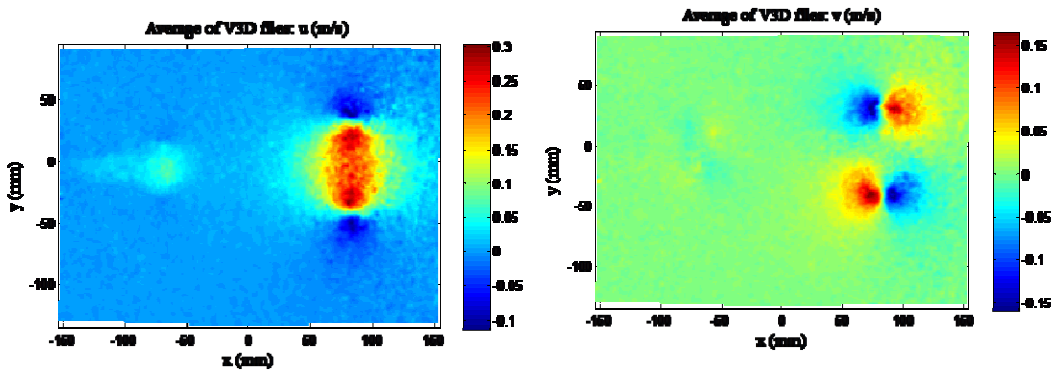
When the tank was filled with seeded water, the measured kinematic viscosity of $0.0983 \text{ in}^2/\text{s}$ yielded a test condition at a Reynolds number of 13,000. This regime was targeted because

published data on ring behavior and formation numbers were available for the left and right skew profiles in this regime (Krueger and Gharib 2003). This regime was also of interest to this study as this Reynolds number represents the flight regime of small birds, such as swallows (*Psalmidoprocne orientalis*) and cockatiels (*Nymphicus hollandicus*).

The results from this experiment corroborate those of the earlier studies. Additionally, the expanded range of velocity profiles permitted the determination of formation numbers for additional pulse shapes. These new pulse shapes were observed to have higher formation numbers than those previously observed, with the impulsive profile demonstrating the highest formation number.

3.4.1 Right Skew Profile

The right skew velocity profile was initially mapped at $L/D = [3, 4, 5, 6]$, and following data analysis, was mapped again at $L/D = [3.4, 3.6, 3.8]$ in an attempt to more accurately determine the formation number. The progression to pinch-off for the right skew velocity profile is summarized in the pairs of u and v velocity component flood plots in Figure 29 below. Evident in the final two frames is satisfaction of both velocity-based pinch-off conditions, a characteristic unique among these pairs of frames. In Figure 30, the corresponding three frame progression of vorticity contours demonstrates fulfillment of the vorticity criterion only at $L/D=4$, confirming the occurrence of pinch-off. This is in accordance with results previously published by Krueger and Gharib. For this test case, the data at non-integer L/D was observed to not cause pinch-off.

(a) $L/D=2$ (b) $L/D=3$ (c) $L/D=4$ Figure 29. Velocity plots for the right skew profile, at $Re=13,000$

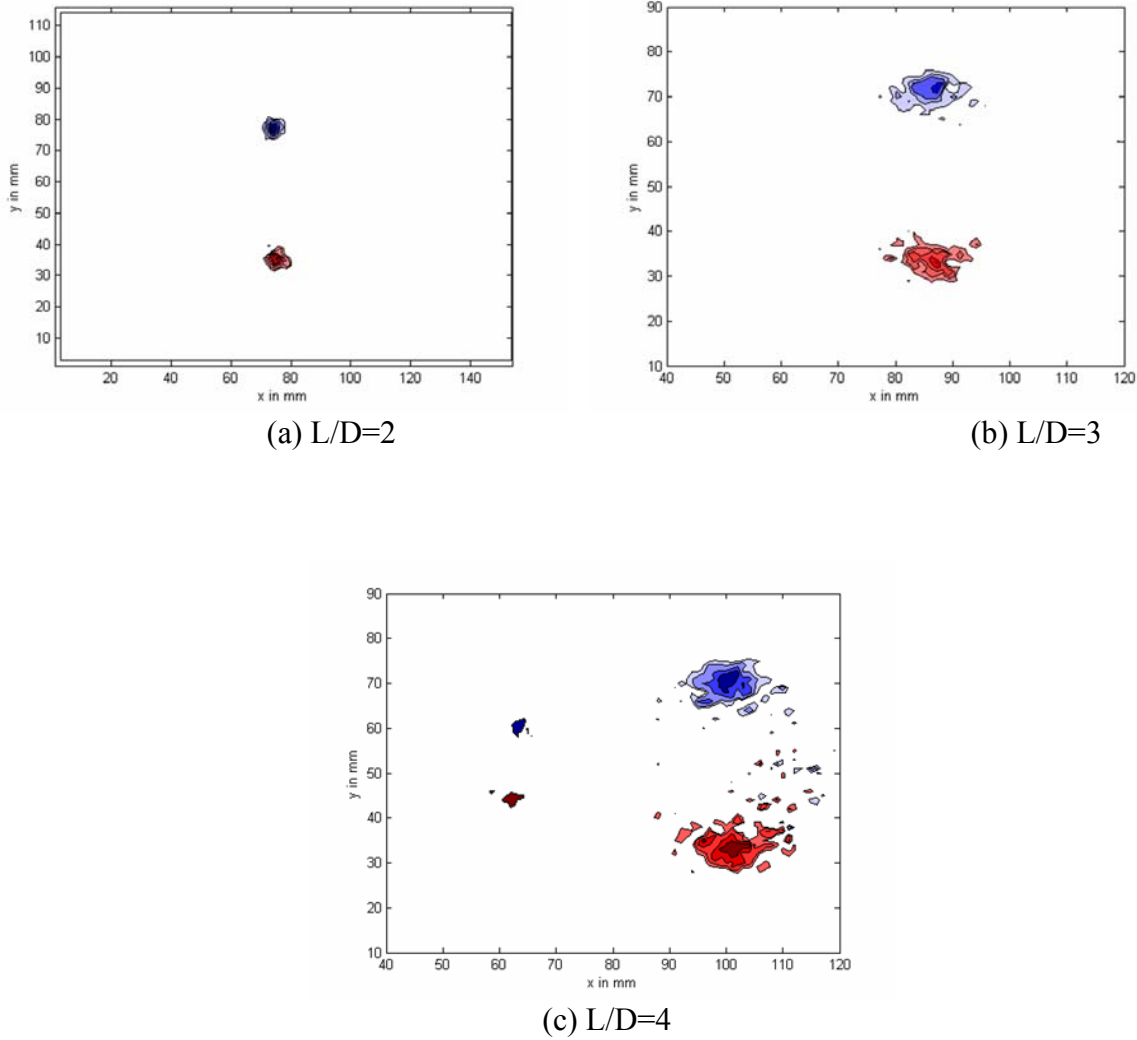
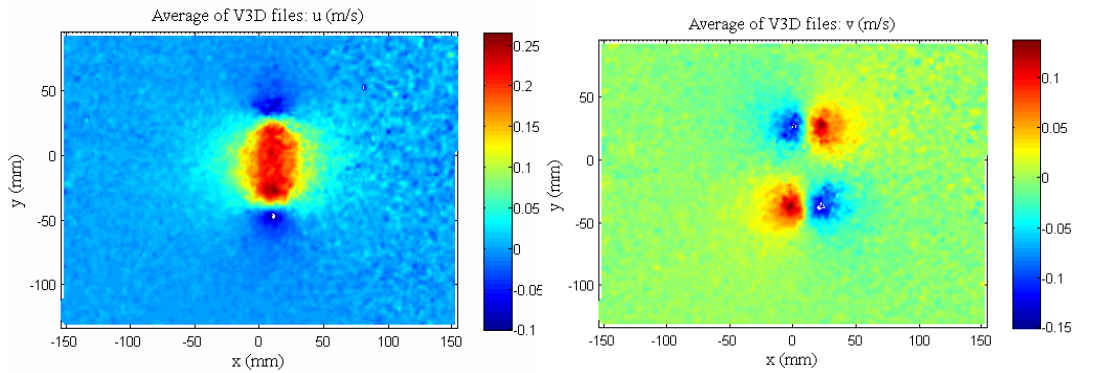


Figure 30. Vorticity maps for the right skew profile at $Re=13,000$

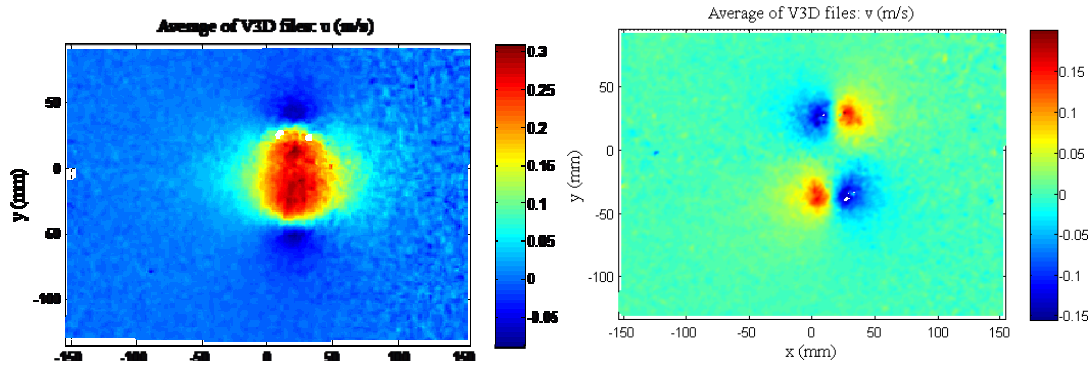
Each of the plots above was created from captures taken at identical times after the initiation of piston motion. Noteworthy in these plots is that as L/D is increased, the physical size of the vortex ring is increased, indicating a larger mass of fluid propagating down the tank. From this it can be inferred that that impulse and thrust potential are also increased, in concurrence with the findings of Krueger and Gharib 2003. Also evident through comparison of these plots is that the propagation velocity of the vortex ring, W , is increased with L/D . This further supports the findings of Krueger and Gharib (2003) concerning the higher thrust potential of rings nearer to the formation number, $f_n = 4$.

3.4.2 Left Skew Profile

Similar to the right skew profile, the left skew profile was initially examined at $L/D = [3, 4, 5, 6]$, after which a secondary sweep was conducted at $L/D = [4.5, 4.7, 4.9]$. The evolution of the left skew driven vortex ring through the range of L/D tested is shown in velocity components in Figure 31, and in corresponding vorticity contours in Figure 32.



(a) $L/D=2$



(b) $L/D=3$

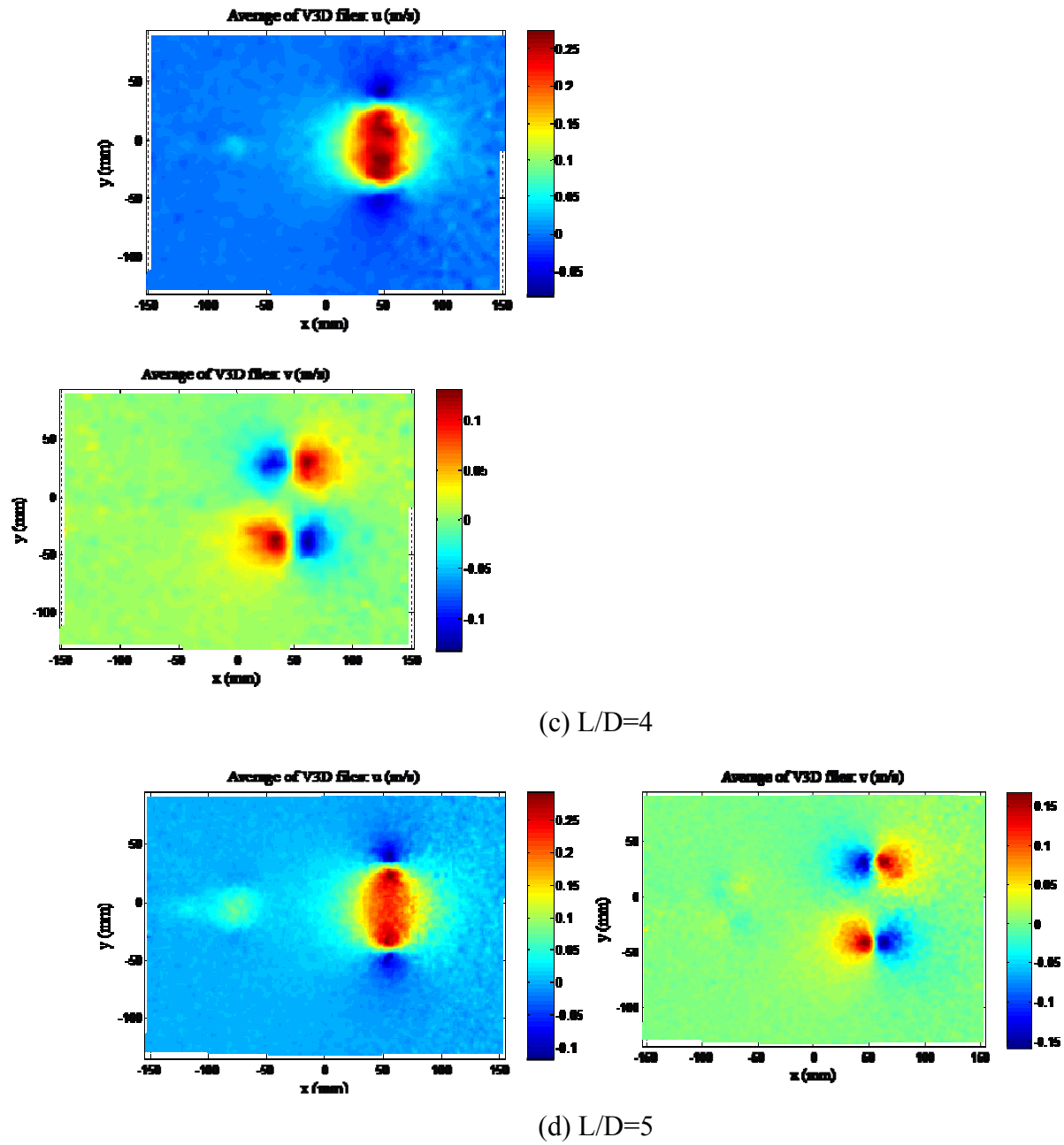
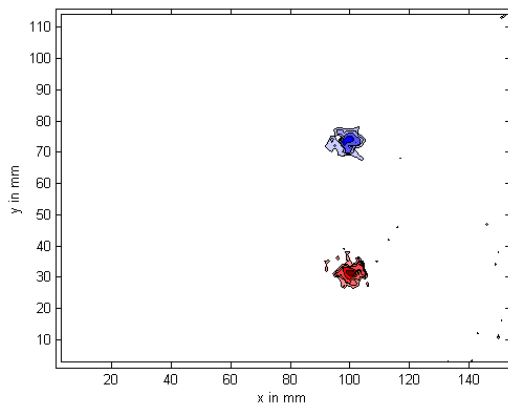
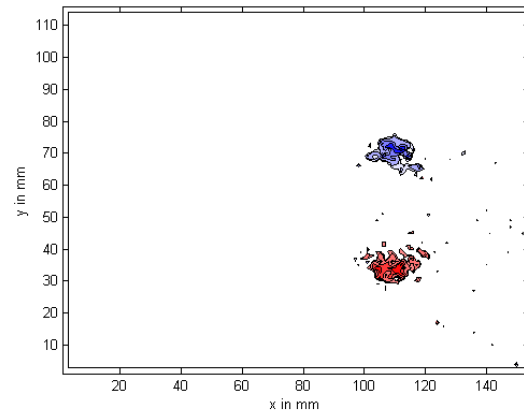
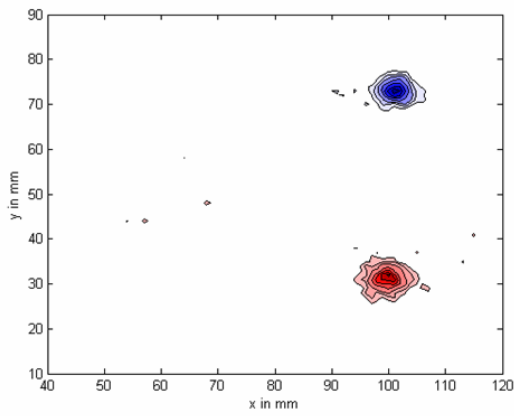
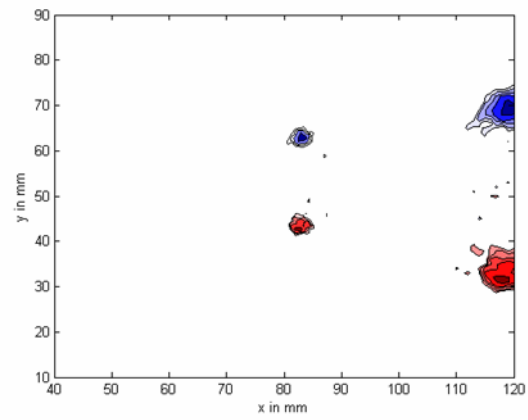


Figure 31. Velocity plots for the left skew profile, at $Re=13,000$

(a) $L/D=2$ (b) $L/D=3$ (c) $L/D=4$ (d) $L/D=5$ Figure 32. Vorticity contours for the left skew profile, at $Re=13,000$

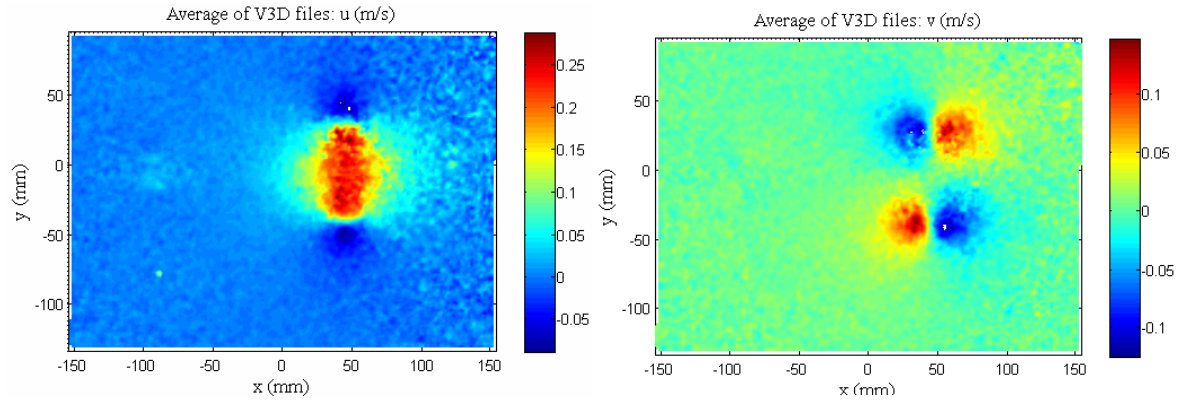
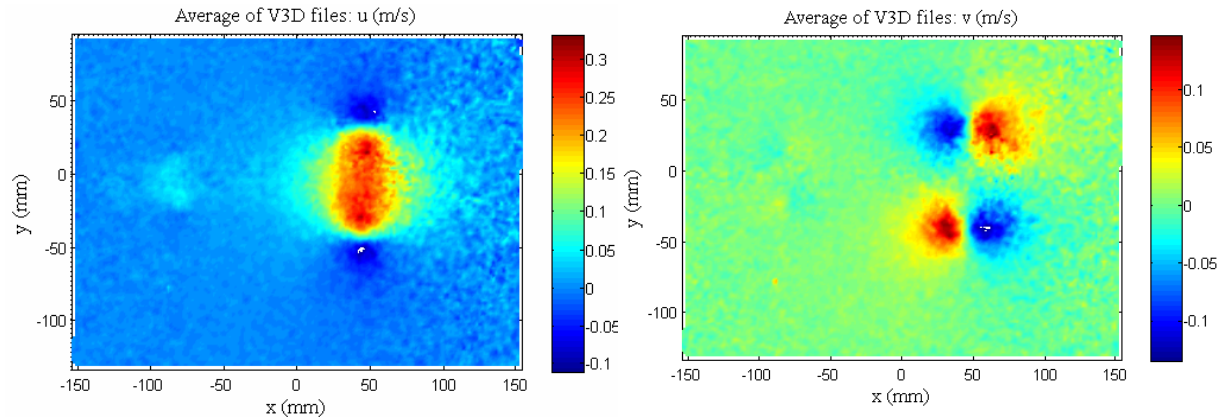
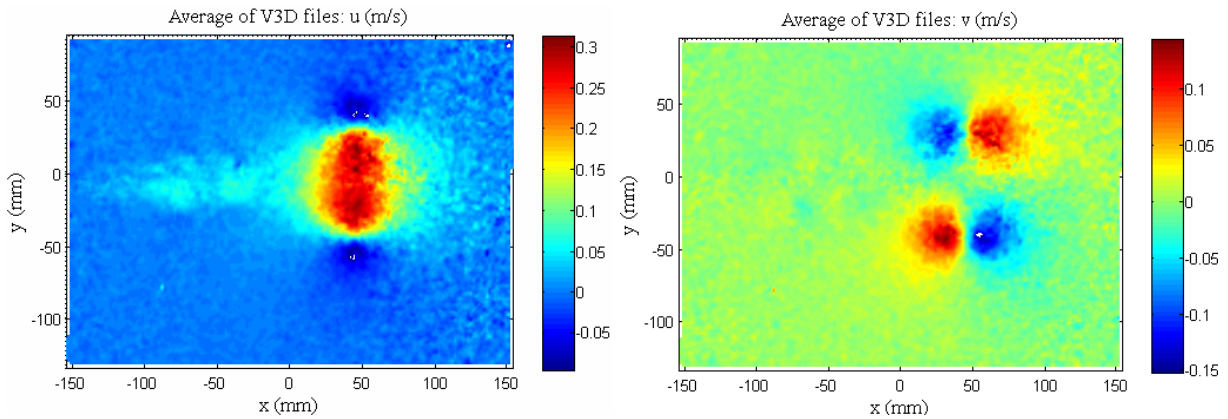
Evolutionary trends related to ring size and propagation velocity are identical to those previously noted in the right skew profile. A significant difference, however, is the delay of the onset of the different stages by what is suggested by the accuracy of this experiment to be a full L/D . This is in precise agreement with the results of Krueger and Gharib (2003) and lends credence to both sets of results. Shusser and Gharib (2000) asserted this delay of pinch-off phenomenon was due to the accelerative nature of this profile, which causes the jet fluid ejected later in the piston stroke to be moving faster than its predecessors, which allows it to catch up to the vortex ring for longer than in the predominantly decelerative profile.

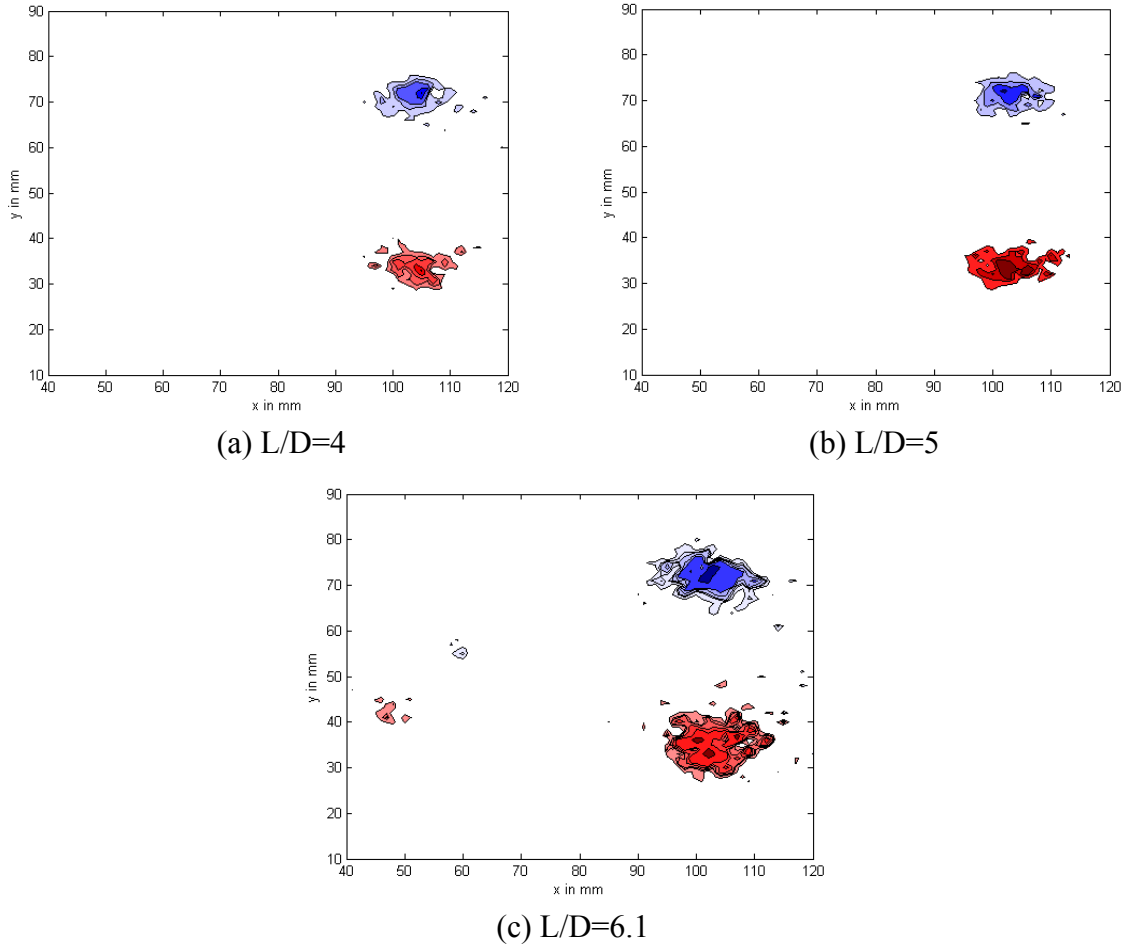
In both this and the right skew profile, in the penultimate set of frames for each, the beginning of a trailing jet is noted. In the final frames, this jet is fully developed and satisfies the criteria for pinch-off, by some addition margin. In this study, only integer L/D were tested, but there is no theory stating that the formation number cannot be fractional (Krueger and Gharib 2003). The experimental data suggests that the L/D when pinch-off is first noted is bracketed between the integer values tested in this study. Future studies will concentrate on further refining the bracketing technique to more precisely determine the exact formation number for this profile; however, until more data is available, it is accurate to conclude that $f_n = 5$.

3.4.3 Symmetrical Profile

The symmetrical profile was evaluated for two reasons. First, the relative ease with which it could be generated made its inclusion in the test plan relatively unobtrusive. Second, if the acceleration fraction is the characteristic which most directly influences the onset of pinch-off, as previous researchers have asserted, this profile should demonstrate a formation number between the L/D at which it occurs for the right profile and the left profile, as its acceleration gradient lies between those of the previously examined profiles.

The symmetrical profile was mapped at $L/D = [3, 4, 5, 6]$, then at $L/D = [5.7, 5.9, 6.1]$. The evolution of the symmetrically driven rings through the range of L/D evaluated is shown with velocity components in Figure 33 and with vorticity in Figure 34.

(a) $L/D=4$ (b) $L/D=5$ 

(c) $L/D=6$ Figure 33. Velocity flood plots for the symmetrical profile, at $Re=13,000$ Figure 34. Vorticity contours for the symmetrical profile, at $Re=13,000$

As the images in Figure 33 show, the expected pinch-off behavior for this profile was not realized. Instead, pinch-off was observed to be delayed to $f_n = 6.1$. This seems to refute the previous theory that the acceleration fraction is the causal mechanism in delaying pinch-off and suggests that at least one other factor is influential in this process.

While the volume of the trailing jet appears, from the translational velocity component, to be significantly larger than those previously observed, both of its velocity components are

proportionally less. The strength of the trailing vortex, as characterized by the magnitude of the vertical velocity components, is nearly equal to the values observed in the proceeding two profiles. The vorticity contours indicate a trailing jet which minimally satisfies all of the pinch-off criteria, indicating accurate characterization of the formation number. This fineness of resolution in formation number could also explain the lower vorticity magnitude noted in the wake of this profile compared to the preceding two profiles. While the mechanism for the delay of pinch-off in this profile will require further study to characterize, these results suggest that the arguments linking pinch-off delay to acceleration may require refinement.

3.4.4 Impulsive Profile

The impulsive profile is the profile which most closely represents the violent exhaust pattern of a gas-powered pulsejet. Its pedigree in vortex ring entrainment studies is significantly less distinguished than the skewed profiles, however, it's inclusion in a test plan is not without precedent (Gharib 1998). In this case, the range of L/D examined was [3, 4, 5, 6, 6.2, 6.4, 6.6, 6.8]. The velocity distributions in the flow field produced by this profile over the range of L/D evaluated are shown in Figure 35.

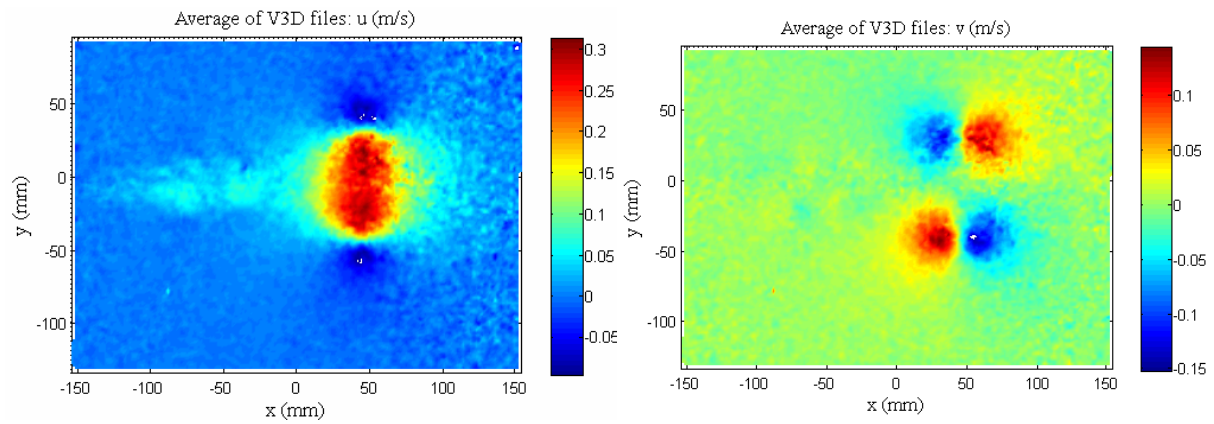
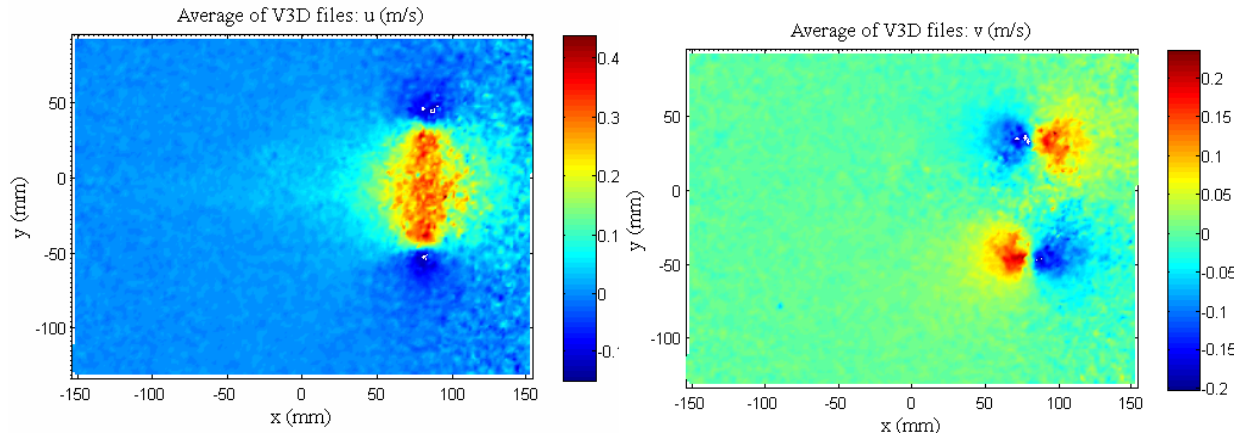
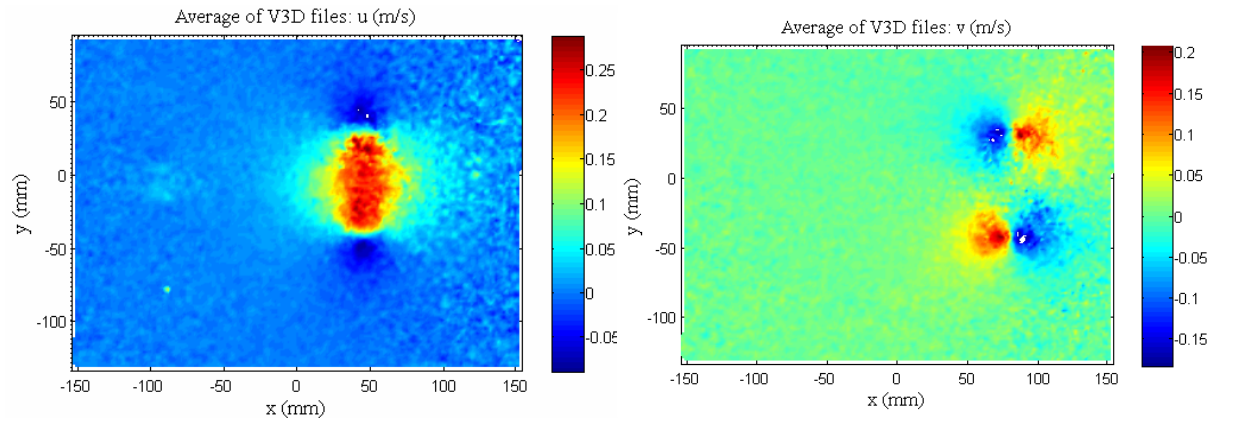


Figure 35. Velocity flood plots for the impulsive profile, at $Re=13,000$

These figures are supported by the vorticity contours shown in Figure 36. These plots show a defined lack of pinch off at L/D less than 6, but a definite pinch off at $L/D=6.2$. Due to the resolution of the experiment, it can only be said that pinch off occurs at $f_n = 6.2$.

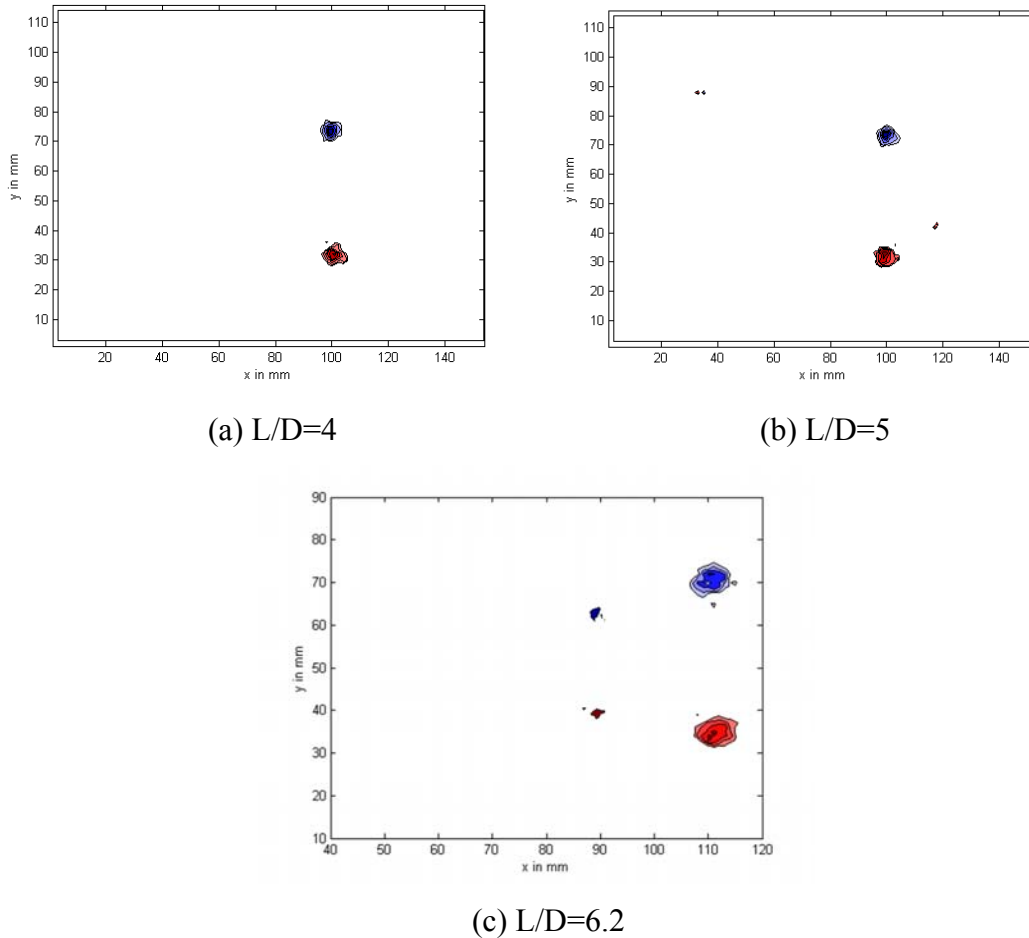


Figure 36. Vorticity contours for the impulsive profile, at $Re=13,000$

As can be observed in Figure 35, the trending of increased propagation velocity with L/D was observed to be maintained for the impulsive profile. Overall ring volume was also observed to increase with L/D for this profile, supporting the theory that vortex rings driven at a higher L/D possess a greater thrust potential. While the development of a trailing secondary vortex can be observed for $L/D=5$ and 6, neither the horizontal nor the vertical velocity components satisfy the requirements for pinch-off. Vorticity contours confirm the lack of a satisfactory vortex in the

wake. This indicates that the entire slug ejected from the nozzle is entrained into the vortex ring and that the weak trailing jet in the vortex wake is likely fluid being lost to viscous effects on the ring. These effects are responsible for the formation of the secondary vortex, which is noted at $L/D=6.2$, the formation number for this velocity profile at $Re=13,000$.

3.5 Results at $Re=1,500$

Testing at a Reynolds number of 1,500 was accomplished through the use of a 60% glycerin solution with an average kinematic viscosity of $0.0152 \text{ in}^2/\text{s}$. All profiles were examined only once in a sweep of $L/D = [2, 3, 4, 5, 6]$. This Reynolds number corresponds to the middle range of potential MAV flight regimes, similar to that of a butterfly or palm-sized aircraft. There is no known previously published data at this flight regime, which prevented validation of the current study at this Reynolds number. However, the results taken at higher Reynolds number attest to the efficacy of the test apparatus, so it is asserted that results in this lower realm are similarly valid.

3.5.1 Right Skew Profile

The right skew profile exhibited the same general trending in this flow regime as it did at the higher Re , as shown in Figure 37. Namely, it had a clearly detached trailing jet vortex which was nearly identical to that seen at $Re=13,000$. Also, this profile had the smallest formation number of the four examined, which was determined to be $L/D=5$. While this was the smallest f_n observed at this Reynolds number, it is significant because it is a full integer step larger than at the Reynolds number nearly ten times larger. This could indicate potentially larger thrust augmentation due to vortex ring entrainment at lower Reynolds number.

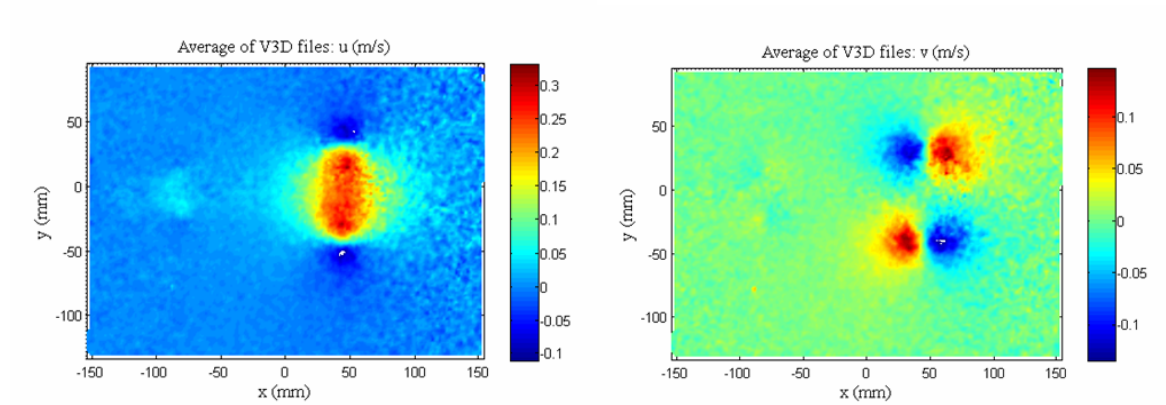


Figure 37. Velocity maps for right skew profile at $Re=1,500$ and $L/D=5$

Also notable in the performance of the right skew profile in this flow regime is the decreased coherency of the vortex cores, clearly visible in Figure 38. Both the main vortex and its trailing jet (when applicable) were considerably more oblong and less concentrated than those noted in Figure 30. Notable, however, is that these results still support all three facets of the author's refined definition of the pinch-off criterion as elucidated previously.

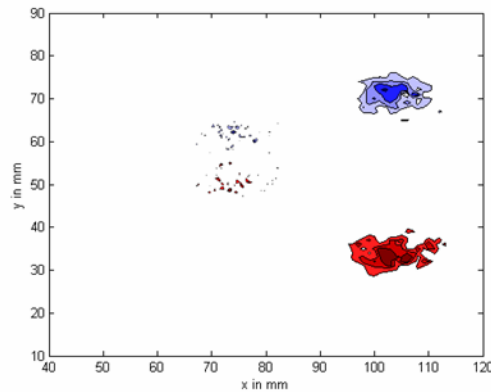


Figure 38. Vorticity contour plot for right skew profile at $Re=1,500$ and $f_n = 5$

3.5.2 Left Skew Profile

The left skew profile exhibited a trailing jet which separated at this Reynolds number in nearly identical fashion to the way it did at the higher Re, as evidenced by Figure 39. The major structural difference between this trailing jet and that seen in the pure water was a slight thinning and longitudinal elongation of the trailing jet, likely caused by the increased shearing forces acting on the structure. This observation, supported by the velocity maps, is clearly evidenced by the vorticity contours in Figure 40, which show a trailing vortex whose cores are distinctly more dispersed and elongated than their higher Re counterparts.

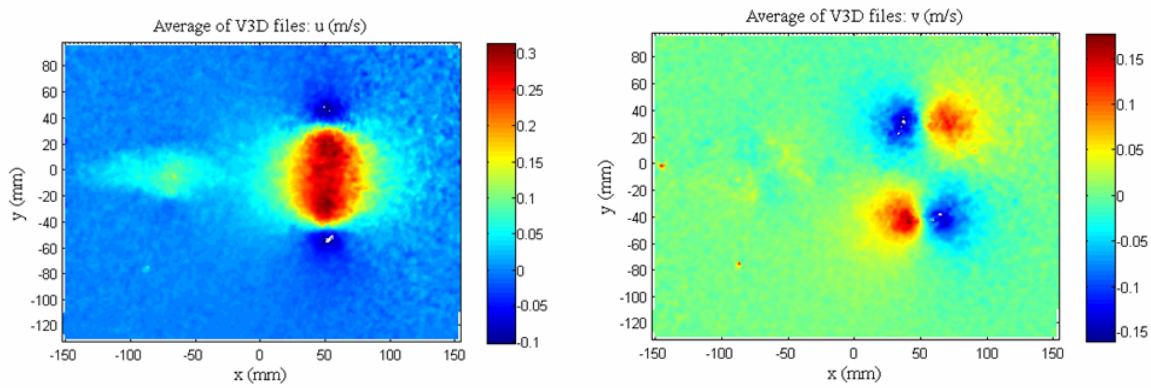


Figure 39. Velocity component maps for left skew profile at $Re=1,500$ and $f_n = 6$

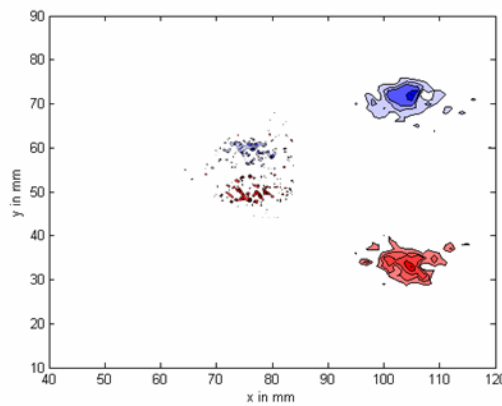


Figure 40. Vorticity contour map for left skew-generated vortex at $Re=1500$ and $f_n = 6$

Of central importance to the application of vortex rings to thrust devices in this flow regime is the delay of pinch-off with this profile to a formation number of 6, fully 20% larger than that seen at $Re=13,000$. As with the right skew profile, this could indicate greater thrust potential at this Re than in the previous flow regime.

3.5.3 Symmetrical Profile

The maximum L/D investigated, at this Reynolds number, of $L/D=6$ proved to be insufficient to determine the formation number of this vortex. While the velocity and vorticity maps show a progression toward pinch-off similar to that seen at the high Reynolds number discussed earlier, as Figure 41 shows, this vortex was clearly not driven completely to the pinch-off point.

Qualitatively, this vortex is physically larger and less coherent than the corresponding vortex in water. Additionally, this vortex had considerably more vorticity shedding in its wake at the higher Reynolds number. This is suggestive of the idea that for this profile, as with the two discussed previously, formation number is increased as Reynolds number is reduced. This delayed pinch-off could be indicative of greater potential for thrust augmentation through vortex ring entrainment with this profile in this flight regime.

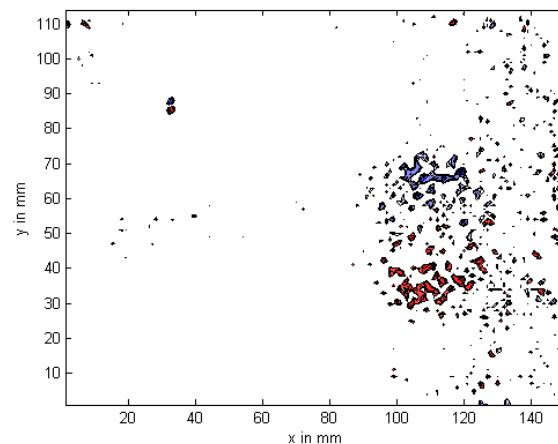


Figure 41. Vorticity contours for symmetrical profile at $Re=1,500$ and $L/D=6$

3.5.4 Impulsive Profile

The impulsive profile again seemed to possess the highest formation number of the profiles tested. While the test matrix consisting of an L/D ceiling of 6 was insufficient to drive the ring to pinch-off, at this highest L/D there is clear evidence that the vortex is beginning to separate from its trailing jet. From the velocity plots in Figure 42, it is clear that the shape of the vortex has been altered somewhat from the previous case, at $Re=13,000$. While the central core remains compact and oblong, there is a definite jet-type structure being dragged in the wake of the vortex, which would likely separate if the vortex were driven at a larger L/D. From the transverse velocity component map, it is evident that this tail structure is not a vortex as it does not exhibit the characteristic pattern of alternating directionality.

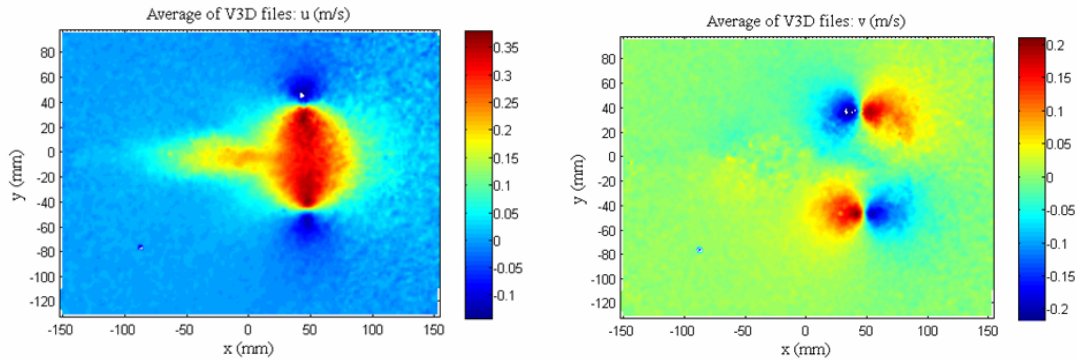


Figure 42. Component velocity flood plots for the impulsive profile at $Re=1,500$ and $L/D=6$

This is confirmed by the vorticity contour plot in Figure 43, which shows some loss of coherency in the primary vortex, and only distributed vorticity in the immediate wake. Notable is the directionality of this vorticity, which is bi-directional and correctly oriented to be a vortex, indicating the ring is nearing the point of pinch-off.

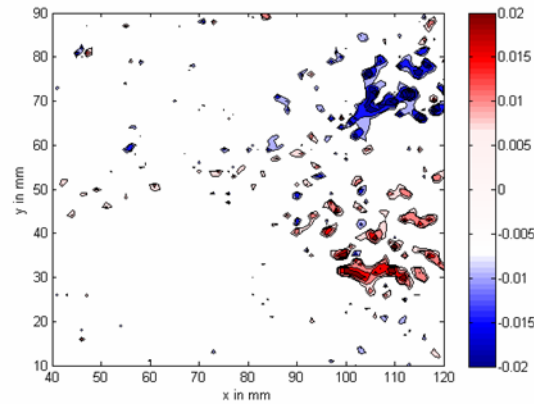


Figure 43. Vorticity contour plot for the impulsive profile at $Re=1,500$ and $L/D=6$

3.6 Results at $Re=780$

Tests were conducted in a 70% aqueous glycerin solution, using a formation number sweep of $L/D = [2,3,4,5,6]$ for all four subject profiles. The average kinematic viscosity of the working fluid during testing was determined to be $0.029 \text{ in}^2/\text{s}$, yielding an average Reynolds number of 780. This Reynolds number corresponds to the flight regime of a mosquito (*Anopheles gambiae*).

This data was found to be of very poor quality, with average vector peak-to-noise values nearly one eighth as large as those obtained at other Reynolds numbers. Examination of the digital image files shows a heavily seed-laden water column, with little laser light reflection into the camera field of view. A review of the vector maps at thus Reynolds number confirms the assessment that little light was reflected into the cameras, as evidenced by a pronounced dearth of vectors in the maps. The image analysis indicates that the tank was likely seeded too heavily and the particles outside of the laser light sheet effectively blocked most of the reflected laser light from reaching the cameras. However, the qualitative nature of the data that was collected and processed provides novel insight into the evolutionary behavior of vortex rings in this flight regime.

Sample velocity component flood plots are shown in Figure 44, demonstrating the noisiness of this data. Sample vorticity contour plots are shown in Figure 45 below, which clearly demonstrate that vortices are considerably more dispersed at this Reynolds number than they were at the aforementioned ones. Also, these vortices indicate a possible enlargement of the formation numbers of the profiles by nearly a step of one L/D over those noted at $Re=1,500$.

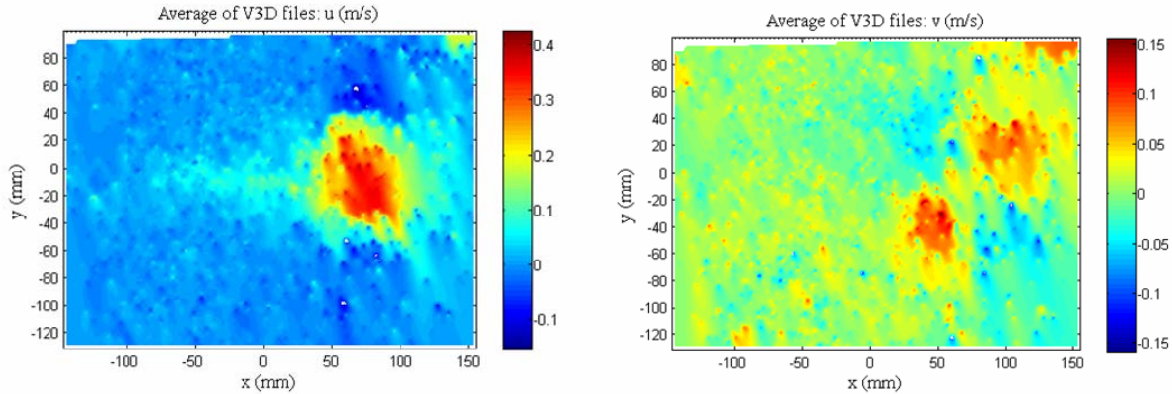


Figure 44. Component velocity plots for the right skew profile at $Re=780$ and $L/D=6$

Vorticity plots are only marginally more readable than the velocity component plots, as evidenced by Figure 45. Notable in all of the vorticity plots, for all profiles at the Reynolds number is a pronounced lack of vortex coherency. While the vortices in at $Re=13,000$ were characterized by tight, concentric circles, these vortices are marked by a more oblong shape. It is believed that the stippled appearance of the vortices is largely a result of having too few vector images to average to get a complete vector field. While there is significant vorticity shedding noted at $L/D=6$ with the right skew profile, this vorticity appears to fail the coherency criterion, in that it is clearly too distributed to denote a well-defined vortex ring. Of note, however, is the fact that this vorticity is bi-directional, with positive vorticity on the bottom and negative vorticity on the top, which is the correct orientation for a vortex ring. This suggests that the ring is nearing pinch-off, but due to the poor quality of images, a conclusive assessment of the formation number cannot be made. However, the observed trending is indicative of a continuation of the previously-noted trend suggesting that pinch-off is delayed to higher formation numbers at lower Reynolds number.

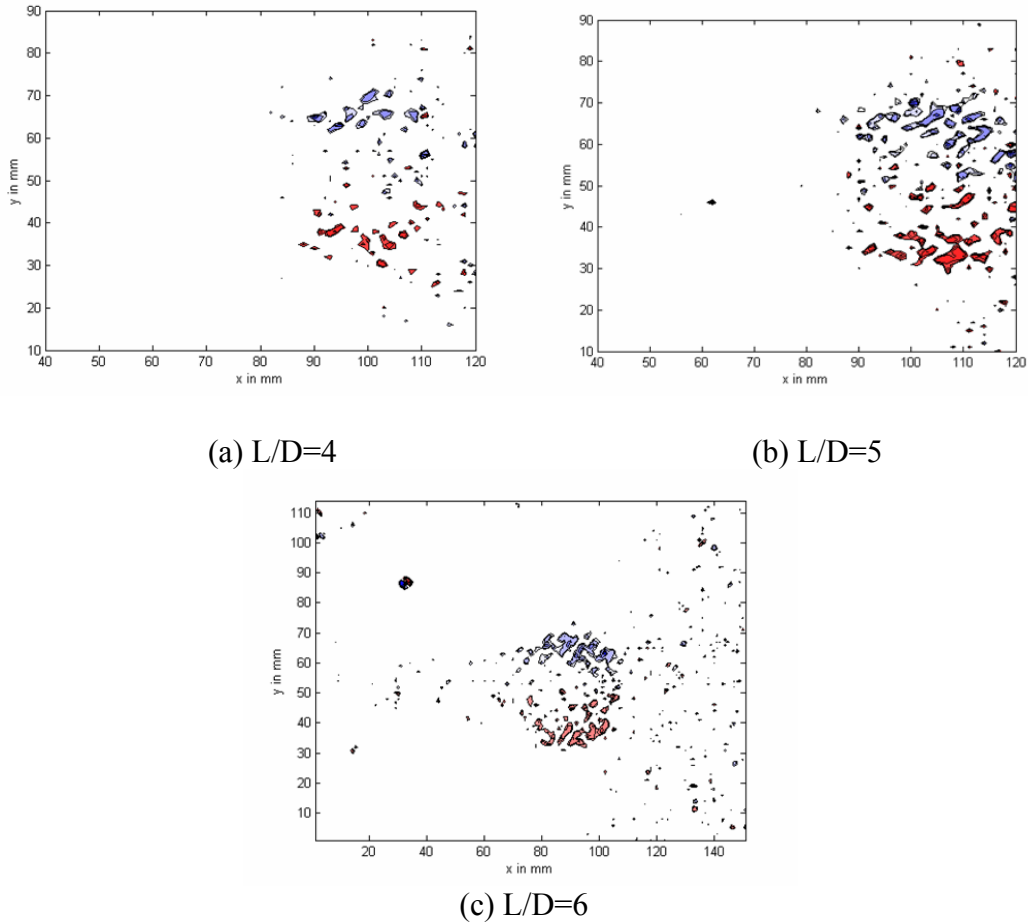


Figure 45. Vorticity contours for the right skew profile, at $Re=780$

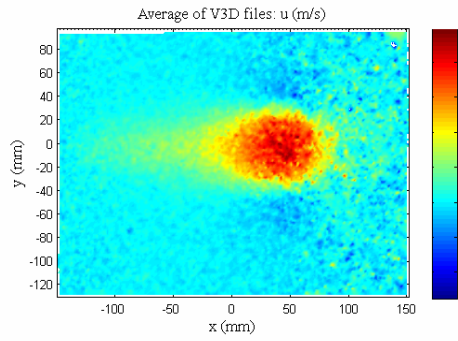
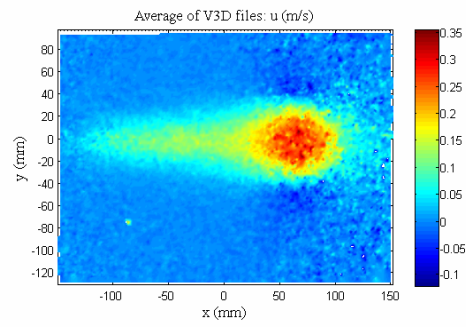
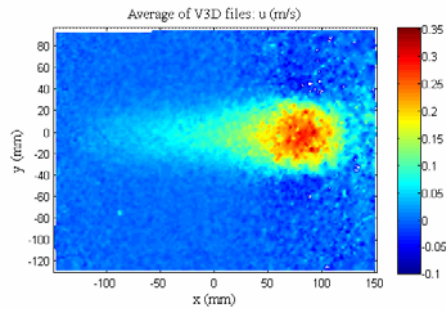
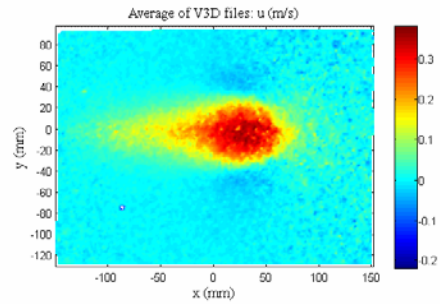
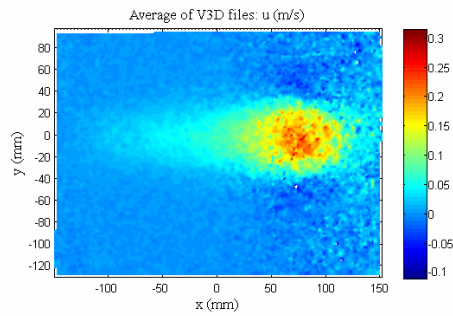
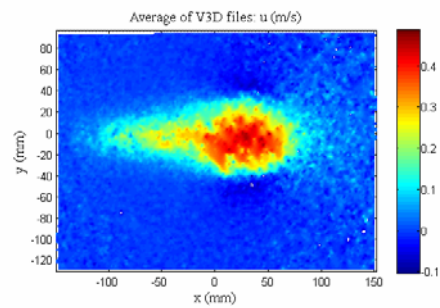
3.7 Results at $Re=250$

An 80% aqueous glycerin solution with an average kinematic viscosity of $0.090 \text{ in}^2/\text{s}$ was utilized to yield a Reynolds number of 250, which would correspond to the lower range of values believed to apply to MAVs. In terms of a natural analog, this Reynolds number simulates the flight regime of a gnat or fruitfly (e.g., *Drosophila melanogaster*). All four profiles were examined in this regime, and following an initial sweep of $L/D = [2, 3, 4, 5, 6]$, an expanded sweep of $L/D = [0.5, 1, 8, 10, 16, 20]$ was performed.

In contrast to the data collected in other glycerin solutions, the data at this concentration was of superior quality, with typical peak to noise ratios similar to those obtained at $Re=13,000$ (on the order of 10^1). This enabled the drawing of precise conclusions concerning pinch-off and vortex evolution at this flight regime. This is of seminal importance because these results are the first of their kind to be published at a Reynolds number this low.

3.7.1 Influence of Velocity Profile

In contrast to findings in other flow regimes which showed that vortex evolution was markedly different for each velocity profile, the velocity and vorticity data collected for all of the profiles examined at this test condition indicated nearly identical patterns in vortex development and evolution. Specifically, all four of the velocity profiles examined (left skew, right skew, symmetrical, and impulsive) began to form a ring at the same L/D , featured identical shaping through an intermediate range of L/D , and refused to pinch-off anywhere in the range of L/D examined. This pulse shape insensitivity is illustrated in Figure 46, which highlights the similarity of rings of various profiles, throughout a representative range of L/D . Most apparent in these panels is the similarity in velocity magnitudes and distribution among rings generated with pulses of the same L/D (i.e., in the same column in Figure 46). Also noteworthy is the increase in intensity, thinning of the vortex, and elongation of the tail portion of the rings as L/D was increased. The propagation velocities of all rings with common L/D were determined to be equivalent; the minute positional displacements of the rings seen in Figure 46 are due to the selection of different frames in the captures to create the averaged images. This was done to obtain the clearest, most complete vector fields possible for each test case.

(a) Right skew profile, $L/D=4$ (b) Right skew profile, $L/D=6$ (a) Left skew profile, $L/D=4$ (b) Left skew profile, $L/D=6$ (a) Symmetrical profile, $L/D=4$ (b) Symmetrical profile, $L/D=6$

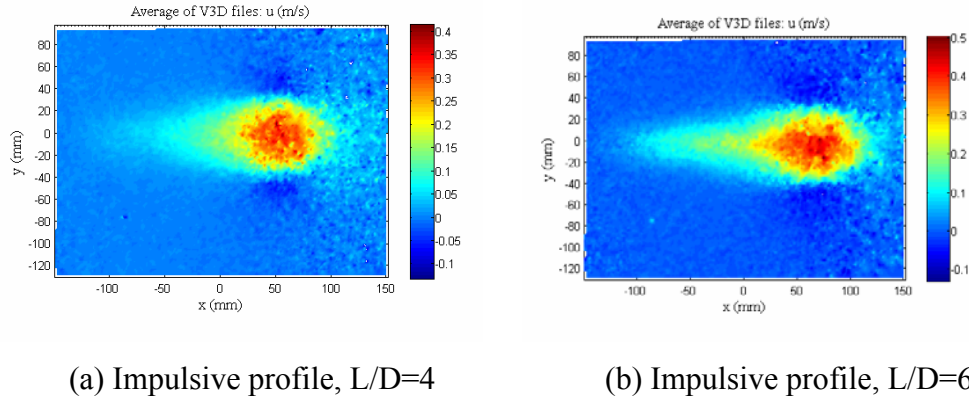


Figure 46. Axial velocity maps showing velocity profile insensitivity, at $Re=250$

This starkly contrasts with trends observed at higher L/D , each case of which showed a definite ability to delay pinch-off evolution through velocity profile manipulation. The disappearance of this phenomenon at $Re=250$ suggests a decrease in the significance of the generator pulse shape as Reynolds number is reduced below a certain value. While this transition value is decidedly below $Re=780$, due to the pulse-dependency trends noted at this Reynolds number, it may be larger than $Re=250$. However, due to the coarseness of the step-size used in the Reynolds number sweep of this study, a more precise value cannot be accurately determined.

This observation concerning the diminishment of the influence of pulse-shaping on pinch-off delay is further supported through trend analysis of the test cases in this study. At the highest Re examined, $Re=13,000$, formation number was increased from $f_n = 4.0$ to $f_n = 6.2$ through the sole influence of velocity profile. At $Re=1,500$, the effect of velocity profile was seen to diminish slightly as the range of formation numbers was seen to shrink, with the right skew profile at $f_n = 5$ and the impulsive profile at $f_n > 6.0$. While the precise formation number of the impulse profile was not determined at this Reynolds number, flow field analysis suggests the formation number to be slightly larger than six and certainly less than 7.2, which is the value required to have the same size range of f_n as witnessed at $Re=13,000$. The final test case examined, $Re=780$, exhibits a further compaction in formation number range, with the right skew

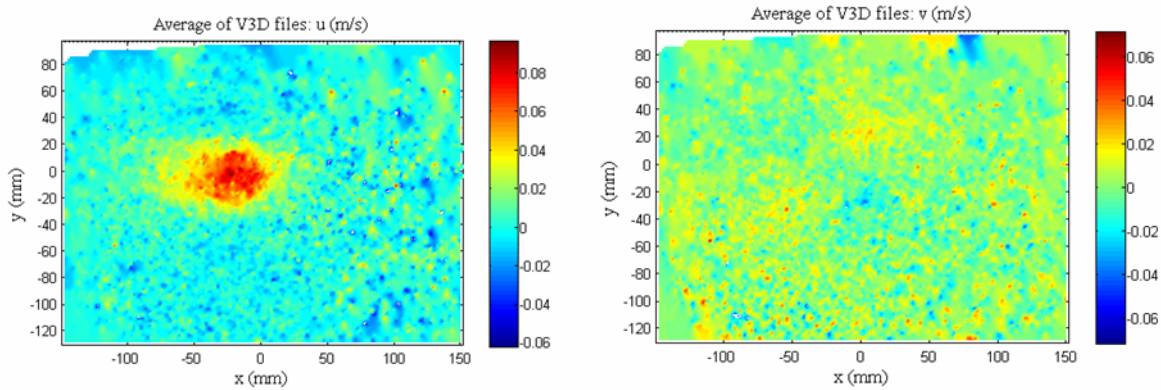
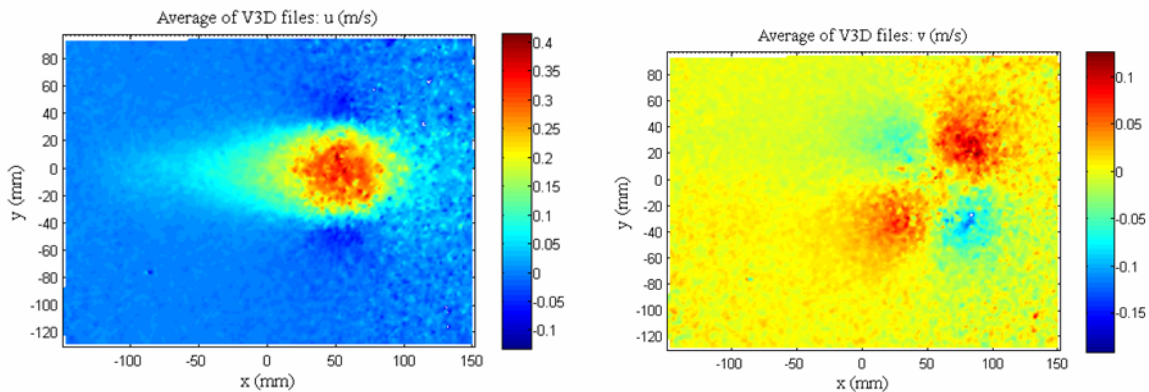
nearing pinch-off at $f_n = 6$ and the impulsive profile only marginally farther away. The logical extension of these trends of formation numbers approaching a common value for all profiles at higher L/D is noted at $Re=250$, where the behavior and development of the vortex rings appears to be independent of velocity profile. Thus, rather than being a drastic, step change in the influence of velocity profile on pinch-off, the insensitivity to pulse-shaping noted at $Re=250$ is merely a continuation of trends noted in all previous cases.

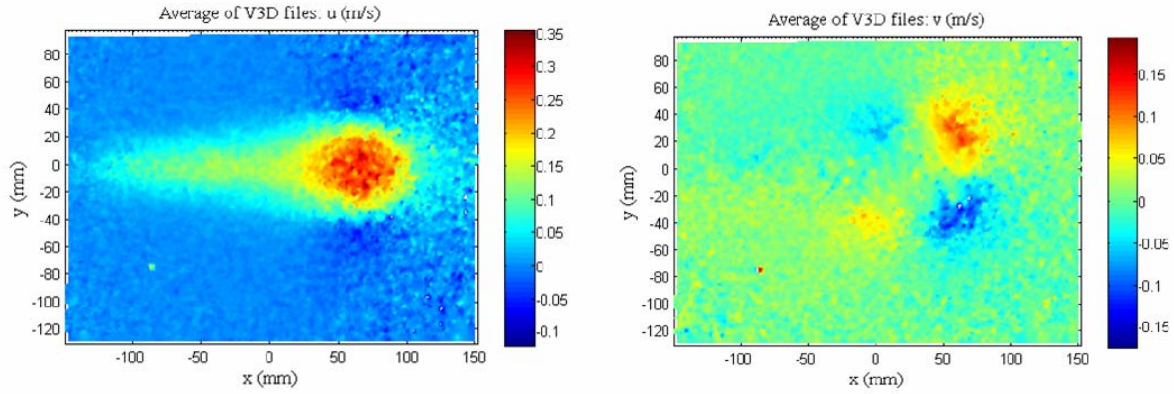
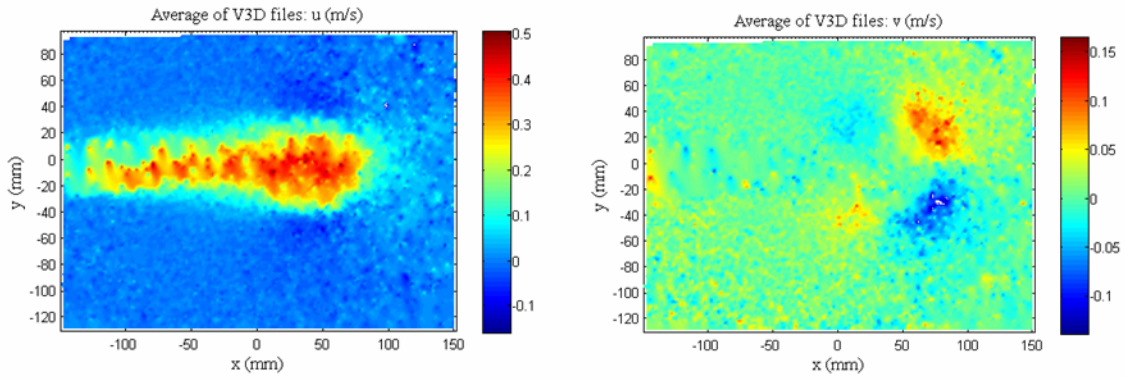
3.7.2 *Ring Structure*

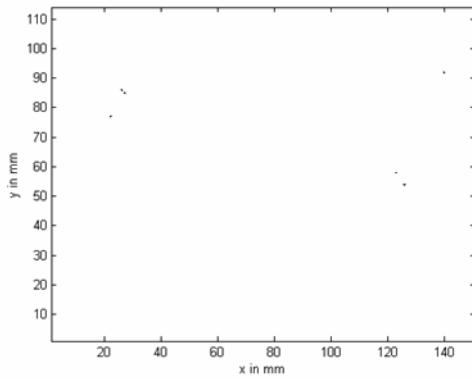
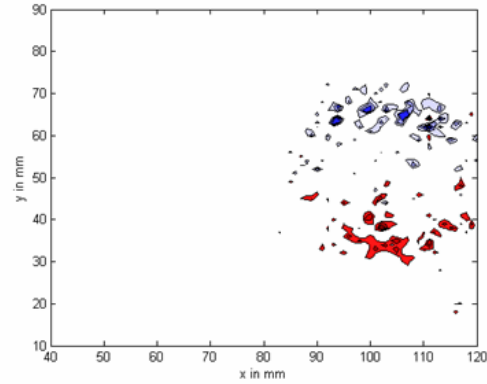
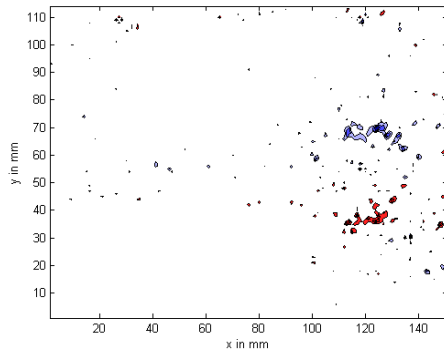
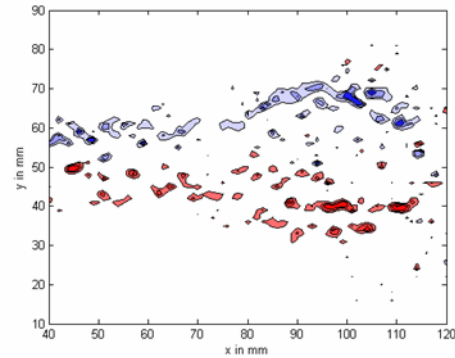
In addition to the velocity profiles not affecting the formation of the rings, at this Reynolds number the structure of the vortices was observed to markedly differ from that of rings at higher Reynolds number. These changes are numerous and noticeable in every facet of the vortex maps. First, the velocity maps, shown in Figure 47, showed a vortex with distinctly rounded core section, instead of the more oblong one noted in other tests. By examining the transverse velocity component, it is evident that the vortex has a much stronger (i.e., faster moving) front section and a much less concentrated, weaker trailing section. Second, all vortices were observed to lose coherency, becoming widely dispersed throughout the erstwhile vortex bubble region, as can be seen in Figure 48. At sufficiently low L/D (i.e., 0.5 and 1), the fluid transited the test region as a slug and rings did not form. At slightly higher L/D (i.e., $L/D=[2, 3, 4, 5, 6]$), the vortex was characterized by a strong leading pair of vortex cores, and a significantly weaker, distributed mass of vorticity. While these vortices were qualitatively similar to those observed at higher Reynolds number, they were noticeably thinner in the transverse direction and elongated axially. Translational velocities for all vortices observed for this combination of flow regime and L/D range were observed to be slower than those seen previously, likely due to the increase in viscous shearing forces.

When L/D was increased to values far exceeding those which had caused pinch-off previously, such as $L/D=[8, 10, 18, 20]$, notable changes in the vortex behavior were observed. Most importantly, the vortices did not pinch off from their generator pulses. Rather, the vortices were observed to elongate axially into a pronounced ‘teardrop’ shape, as shown in Figure 47 (c) and

(d). The vortices were characterized by a strong pair of leading vortex cores, followed by a much weaker pair forming the trailing half of the characteristic four dot vortex pattern discussed previously. Significantly elevated quantities of vorticity were observed in the trailing, pointed section of the vortex bubble. This vorticity was observed to be of the correct directionality to be the after end of a vortex, but its widely-dispersed appearance gave the vortex bubble the teardrop shape not observed at other Reynolds numbers and precluded any declaration of the occurrence of pinch-off. While the design of the test apparatus prevented the direct measurement of thrust, if trends noted by previous researchers hold at $Re=250$, these new findings could indicate greater benefit to thrust augmentation through vortex ring entrainment (Krueger and Gharib 2003). This greatly increases the potential viability of a pulsed, vortex ring generating propulsion system to vehicle motility at this Reynolds number.

(a) $L/D=1$ (b) $L/D=4$

(c) $L/D=10$ (d) $L/D=20$ Figure 47. Velocity component plots of varying profiles, at $Re=250$

(a) $L/D=1$ (b) $L/D=4$ (c) $L/D=10$ (d) $L/D=20$ Figure 48. Vorticity contours, at $Re=250$

3.8 Summary of Observed Trends

The data presented previously suggest clear tendencies in vortex ring formation, structure, and formation number. When velocity and vorticity maps from each Re are plotted relative to similar images from different Re on a graph of Reynolds number versus formation number, these trends become readily apparent, as shown in Figure 49.

In Figure 49, the black parallelogram indicates the relative acceptable range of conditions under which vortices are formed. At sufficiently small a Reynolds number and L/D combination (i.e., the upper left corner of Figure 49), no vortex ring formation was noted. At sufficiently large

combinations of these parameters (i.e., the lower right corner of the figure), the ring was observed to pinch-off, which is considered an undesirable condition due to the sharp reduction in thrust realized from a pinched-off ring. At sufficiently low Reynolds number, the ring becomes affected by the shearing forces dramatically enough that its characteristic shape is altered and it attains a teardrop cross-sectional appearance. The effect of this change on thrust augmentation is unknown.

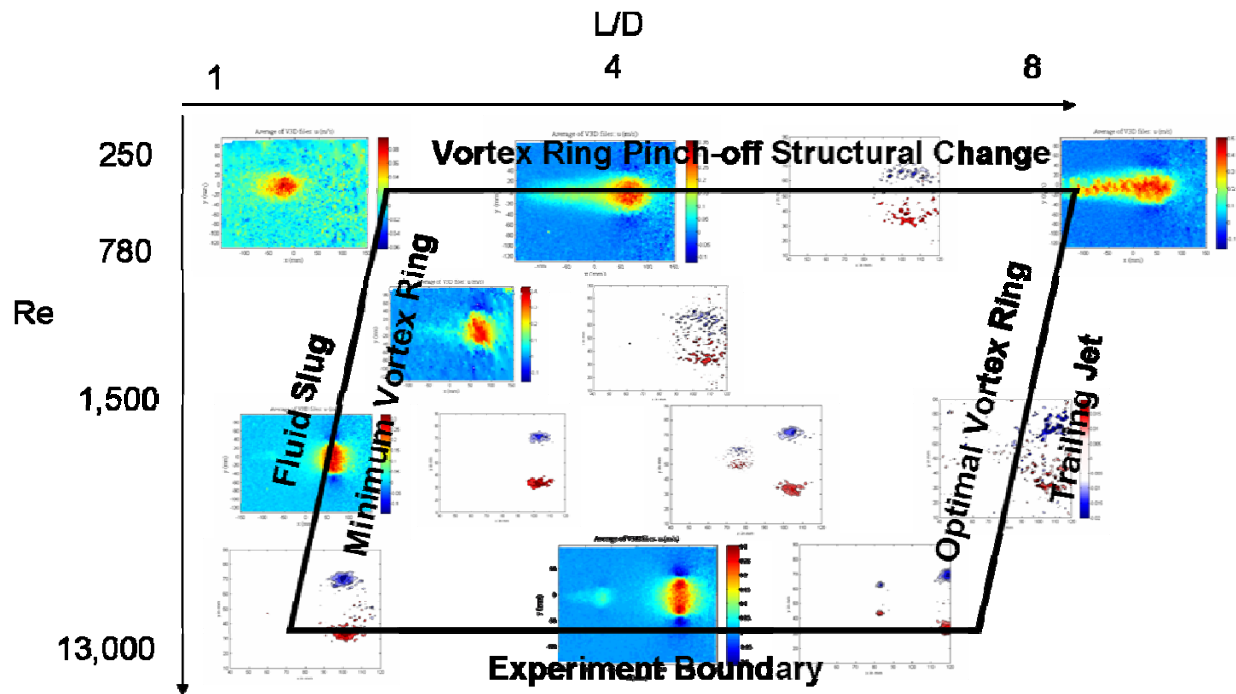


Figure 49. Major observed vortex ring evolutionary trends, with Reynolds number

3.9 Implications of Results

The results of this research have a number of implications, especially in the field of low Reynolds number vehicle design. Primarily, the formation number trends presented graphically in Figure 49 indicate that specialized tuning to the specific flow regime of interest will be required for any viable vortex ring propulsion system. Specific design concerns dictated by the target vehicle Reynolds number include the velocity profile of the engine and the exhaust pulse size. This research indicates that the most efficient engine would be that which closely replicates

the impulsive velocity profile and ejects pulses of a size shown along the rightmost leg of the parallelogram in Figure 49.

The observed changing of the vortex ring structure and evolution with Reynolds number could imply greater thrust augmentation potential at lower Reynolds number. The rings are characterized by higher formation numbers as Reynolds number is decreased, which was previously shown to correspond to greater thrust augmentation and greater overall thrust (Krueger and Gharib 2003). The logical limit to this pattern would be rings that never pinch-off and can grow to arbitrarily large size, dependent on generator pulse size. This was observed at the lowest Reynolds number test condition, $Re=250$, which implies that the benefits of thrust augmentation in this regime are significantly greater than those at less laminar regimes. The logical extension of this is that the viability of vortex ring-based propulsion systems increases markedly with the creation of ever-smaller vehicles. Thus, the propulsion of a gnat-sized aerial vehicle could be easier to achieve than that of a butterfly-sized vehicle. This would greatly expand the mission envelope of UAVs and UUVs and could cause a significant shift in intelligence-gathering and war-fighting doctrines.

A possible counterpoint to this idea could be implied by the noted structural trends noted at $Re=250$. Namely, that the thrust benefits of vortex rings are lost or greatly diminished when Reynolds number is reduced lower than a characteristic value. The precise effects of the incorporation of the elongated tail into the vortex ring, and the widely-dispersed vorticity therein, on thrust augmentation are unknown. It is therefore possible that these results suggest a lower limit to the viability of vortex ring propulsion schemes.

A final implication of these results is the utility of a variable diameter exit nozzle in vortex ring propulsion applications. In any vehicle motion, a range of velocities and viscosities is encountered. These changes in U and ν correspond to variations in Reynolds number, which this study has shown causes a shift in formation number. In order to operate at maximum efficiency throughout the vehicle mission profile, a ring-driven engine could possess a variable diameter exit nozzle to change the third variable in the Reynolds number equation and maintain the

highest formation number possible. This change in nozzle exit diameter would also yield a change in L/D , which could push pulse sizes closer to the formation number, and therefore, optimum propulsion potential.

4 CONCLUSIONS

The effects of piston velocity profile and L/D ratio on vortex ring entrainment and pinch-off were evaluated using SPIV in a novel test facility. The following specific conclusions may be drawn from an analysis of the data:

- The implementation of a rigidly-coupled piston and stepper motor in a vortex ring generator was shown to enable the repeatable collection of high-fidelity flowfield mappings.
- With SPIV, it is possible to precisely quantify the velocity components of the vortex ring, which permits the establishment of a more precise definition of pinch-off in the laboratory setting. This in turn improves the accuracy and repeatability of vortex pinch-off determinations.
- Left-skew or predominantly accelerative velocity profiles delay pinch-off by approximately one L/D over similar profiles with a smaller acceleration fraction.
- A symmetrical velocity profile delays pinch-off by as much as one L/D over a left skew profile.
- A profile characterized by “impulsive” acceleration and deceleration periods appears to delay pinch-off longer than all other profiles tested.
- The circulation and volume of the vortex ring for all velocity profiles is positively correlated to the length of the slug which can be ejected from the nozzle prior to pinch-off.
- As Reynolds number decreases, vortex rings lose their coherency, eventually obtaining a teardrop shape. Appearing to accompany this loss of coherency, is a reduced tendency to pinch-off and form a secondary vortex. At sufficiently low Reynolds number ($Re=250$), there appears to be a prohibition on pinch-off as none was observed, even at much higher L/D than should be required for pinch off.
- The trend of increasing formation numbers with decreasing Reynolds numbers was validated at lower Reynolds numbers than previously studied, to a lower limit of $Re=250$.

- The number of vector dropouts in ensemble averaged data was significantly smaller in data sets where more runs were averaged. While four runs provides data with acceptable accuracy, using a test plan with ten runs at each L/D yields a far smoother and more complete flow field.

4.1 Recommendations

Future tests should incorporate a minimum of ten runs for each condition (i.e., L/D, profile combination) to accurately map the entire flow field and reduce the number of vector dropouts to an unobtrusive and aesthetically- acceptable level.

Repetition of tests in 70% glycerin solution should be completed, to more accurately assess the trends noted from the sparse data from this experiment.

Direct thrust measurements would provide a useful way to truly assess the relative merit of each velocity profile to flight propulsion schema.

Nozzle exit overpressure measurements would provide more definitive insight into the relationship of this mechanism with the pinch-off phenomenon.

Further investigation of novel velocity profiles with varying acceleration and deceleration fractions is necessary for the correct characterization of the ‘optimal’ profile around which an engine could be designed.

If a hotfilm probe with sufficiently high sampling rate were utilized to gather velocity data at the nozzle exit plane, quantitative comparisons of momentum flux and thrust augmentation could be made. This would strengthen the conclusions suggested by the present study and provide more directly applicable data to the UAV propulsion problem.

Alternatively, the SPIV system could be moved to focus on the orthogonal plane, at the nozzle exit. The resulting data could then be integrated to determine the momentum flux contributed by

the exit mass flow, thereby permitting quantitative comparison of momentum flux and thrust augmentation data.

The case of a fully-pulsed jet should be explored to assess any effects that pulsing have on vortex ring development and thrust augmentation.

BIBLIOGRAPHY

Alkislar, M. B., Choutapalli, I., et al., "The Structure of a Pulsed Jet- A PIV Study," *Proceedings of the 43rd AIAA Aerospace Sciences Meeting and Exhibit*, 2005, AIAA Paper number 2005-1274.

Allen, J. J., and Auvity, B., "Interaction of a Vortex Ring with a Piston Vortex," *Journal of Fluid Mechanics*, Vol. 465, 2002, pp. 353-378.

Allen, J. J., and Chong, M. S., "Vortex Formation in Front of a Piston Moving Through a Cylinder," *Journal of Fluid Mechanics*, Vol. 416, 2000, pp. 1-28.

Bird, R. B., Stewart, W. E., and Lightfoot, E. N., *Transport Phenomena*, Wiley, New York, 1960.

Cantwell, B. J., "Viscous Starting Jets," *Journal of Fluid Mechanics*, Vol. 173, pp. 159-189.

Cook, J., et al., "Characterizing Vortex Ring Behavior During Ventricular Filling with Doppler Echocardiography: An *in Vitro* Study," *Annals of Biomedical Engineering*, Vol. 32, 2004, pp. 245-256.

Dabiri, J. O., and Gharib, M., "Fluid Entrainment by Isolated Vortex Rings," *Journal of Fluid Mechanics*, Vol. 511, 2004, pp. 311-331.

Dabiri, J. O., and Gharib, M., "The Role of Optimal Vortex Formation in Biological Fluid Transport," *Proceedings of the Royal Society of Biology*, Vol. 272, 2005, pp. 1557-1560.

Didden, N., "On the Formation of Vortex Rings - Rolling-up and Production of Circulation," *Zeitschrift fuer angewandte Mathematik und Physik*, Vol. 30, 1979, pp. 101-116.

Epstein, A. H., et al., "Power MEMS and Microengines," *Transducer 97*, pp. 753-756.

Fabris, D., and Liepmann, D., "Vortex Ring Structure at Late Stages of Formation," *Physics of Fluids*, Vol. 9, 1997, pp. 2801-2803.

Gharib, M., Rambod, E., and Shariff, K., "A Universal Time Scale for Vortex Ring Formation," *Journal of Fluid Mechanics*, Vol. 360, 1998, pp. 121-140.

Gharib, M., et al., "On the Effect of Pipe Boundary Layer Growth on the Formation of a Laminar Vortex Ring Generated by a Piston/Cylinder Arrangement," *Theoretical and Computational Fluid Dynamics*. Vol. 15, 2002, pp. 303-316.

- Gharib, M., et al., "Optimal Vortex Formation as an Index of Cardiac Health," *Proceedings of the National Academy of Sciences of the United States of America*, Vol. 103, 2006, pp. 6305-6308.
- Glezer, A., "The Formation of Vortex Rings," *Physics of Fluids*, Vol. 31, 1988, pp. 3532-3542.
- Glezer, A., and Coles, D., "An Experimental Study of a Turbulent Vortex Ring," *Journal of Fluid Mechanics*, Vol. 211, 1990, pp. 243-283.
- Hanff, E. S., "PIV Application in Advanced Low Reynolds Number Facility," *IEEE Transactions on Aerospace and Electronic Systems*, Vol. 40, 2004, pp. 310-319.
- Hedrick, T. L., et al., "Estimates of Circulation and Gait Change Based on a Three-Dimensional Kinematic Analysis of Flight in Cockatiels (*Nymphicus hollandicus*) and Ringed Turtle-Doves (*Streptopelia risoria*)," *The Journal of Experimental Biology*, Vol. 205, 2002, 1389-1409.
- Kaplanskii, F. B., and Rudi, Y. A., "Evolution of a Viscous Vortex Ring," *Fluid Dynamics*, Vol. 36, 2001, pp. 16-25.
- Krueger, P. S., and Gharib, M., "Thrust Augmentation and Vortex Ring Evolution in a Fully-Pulsed Jet," *AIAA Journal*, Vol. 43, No. 4, 2005, pp. 792 – 801.
- Krueger, P.S., and Gharib, M., "The Significance of Vortex Ring Formation to the Impulse and Thrust of a Starting Jet," *Physics of Fluids*, Vol. 15, 2003, pp. 1271-1281.
- Krueger, P. S., "An Over-pressure Correction to the Slug Model for Vortex Ring Circulation," *Journal of Fluid Mechanics*, Vol. 545, 2005, pp. 427-443.
- Lauder, G. V., and Drucker, E. G., "Forces, Fishes, and Fluids: Hydrodynamic Mechanisms of Aquatic Locomotion," *News in Physiological Science*, Vol. 17, 2002, pp. 235-240.
- Linden, P. F., and Turner, J. S., "'Optimal' Vortex Rings and Aquatic Propulsion Mechanisms," *Proceedings of the Royal Society*, Vol. 271, 2004, pp. 647-653.
- Lucey Jr., G. K., "Vortex Ring Generator: Mechanical Engineering Design for 100-kpsi Operating Pressures," Army Research Laboratory Technical Report no.: ARL-TR-2096, 1999.
- Michelson, R.C., "Novel Approaches to Miniature Flight Platforms," *Proceedings of the Institute of Mechanical Engineers*, Vol. 218, Part G: Journal of Aerospace Engineering, Special Issue Paper, 2004, pp. 363-373.
- Mohseni, K., "Pulsatile Vortex Generators for Low-Speed Maneuvering of Small Underwater Vehicles," *Journal of Ocean Engineering*, Vol. 33, 2006, pp.2209-2223.

- Mohseni, K., Hongyu R., and Colonius, T., "Numerical Experiments on Vortex Ring Formation," *Journal of Fluid Mechanics*, Vol. 430, 2001, pp. 267-282.
- Mueller, T. J., "Proceedings of the Conference on Low Reynolds Number Airfoil Aerodynamics", *Lecture Notes in Engineering*, Vol. 54, 1989, pp. 1-347.
- Nitsche, M., and Krasny, R., "A Numerical Study of Vortex Ring Formation at The Edge of a Circular Tube," *Journal of Fluid Mechanics*, Vol. 276, pp. 139-161.
- Pierrakos, O., and Vlachos, P. P., "The Effect of Vortex Formation on Left Ventricular Filling and Mitral valve Efficiency," *Journal of Biomechanical Engineering*, Vol. 128, 2006, pp. 527-539.
- Rayner, J. M. V., "A Vortex Theory of Animal Flight. Part 1. The Vortex Wake of a Hovering Animal," *Journal of Fluid Mechanics*, Vol. 91, 1979, pp. 697-730.
- Rosenfeld, M., Rambod, E., and Gharib, M., "Circulation and Formation Number of Laminar Vortex Rings," *Journal of Fluid Mechanics*, Vol. 376, 1998, pp.297-318.
- Saffman, P. G., "Dynamics of Vorticity," *Journal of Fluid Mechanics*, Vol. 106, 1981, pp. 49-58.
- Shariff, K., and Leonard, A., "Vortex rings," *Annual Review of Fluid Mechanics*, Vol. 24, 1992, pp. 235-279.
- Shusser, M., and Gharib, M., "Energy and Velocity of a Forming Vortex Ring," *Physics of Fluids*, Vol. 12, No. 3, 1999, pp. 618-621.
- Siekman, J., "On a Pulsing Jet from the End of a Tube, with Application to the Propulsion of Certain Aquatic Animals," *Journal of Fluid Mechanics*, Vol. 15, 1963, pp. 399-418.
- Thompson, J. T., and Kier, W. M., "Ontogeny of Squid Mantle Function: Changes in the Mechanics of Escape-Jet Locomotion in the Oval Squid, *Sepioteuthis lessoniana*," *Biology Bulletin*, Vol. 203, 2002, pp. 14-26.
- Van Dyke, M., *An Album of Fluid Motion*, Parabolic, Stanford, 1982.
- Weih, D., "Periodic Jet Propulsion of Aquatic Creatures," *Fortschritte der Zoology*, Vol. 24, 1977, pp. 171-175.
- Wilson, J. R., "Mini Technologies for Major Impact," *Aerospace America*, Vol. 36, 1998, pp. 36-38, 41, 42.

Zhao, W., Frankel, S. H., and Mongeau, L. G., “Effects of Trailing Jet Instability on Vortex ring Formation,” *Physics of Fluids*, Vol. 12, 2000, pp. 589-596.

APPENDIX A: CONTRACTION CURVE SCRIPT

```

%% Vortex Nozzle Contours

clear, clc, format compact
D1 = 9.2;    % Nozzle inlet diameter in inches.
D2 = 1.9;    % Nozzle exit diameter in inches.
L = 12;      % Nozzle length in inches.

x = [
    0:0.005:L/4],[L/4+0.01:0.01:L/2],[L/2+0.03:0.03:3/4*L],[3/4*L+0.1:0.1:L] ];
npts = length(x);

% Calculate a cubic contour
% Constraints:
% y(0) = 0.5*D1
% y(L) = 0.5*D2
% y'(L) = y''(L) = 0

A = [0 0 0 1; L^3 L^2 L 1; 3*L^2 2*L 1 0; 6*L 2 0 0];
b = [D1/2; D2/2; 0; 0];
k3 = A\b          % Coefficients k are the constants to the cubic y3(x).

% Calculate radius, area, and gradient of the velocity ratio...
y3 = polyval(k3, x);
A3 = pi*y3.^2; V3oV1 = A3(1)./A3;
dV3oV1dxoL(1) = (V3oV1(2)-V3oV1(1))/(x(2)-x(1))*L;
dV3oV1dxoL(npts) = (V3oV1(npts)-V3oV1(npts-1))/(x(npts)-x(npts-1))*L;
for i=2:npts-1
    dV3oV1dxoL(i) = (V3oV1(i+1)-V3oV1(i-1))/(x(i+1)-x(i-1))*L;
end

figure(1), plot(x,y3,'-b',x,-y3,'-r'), hold on
figure(2), plot(x,A3,'-g',x,V3oV1,'-k'), hold on
figure(3), plot(x/L,dV3oV1dxoL,'-m'), hold on
[maxV,imax]=max(dV3oV1dxoL); maxV, x(imax)/L

% Calculate a quartic contour
% Constraints:
% y(0) = 0.5*D1
% y(L) = 0.5*D2
% y'(L) = y''(L) = 0
% y'(0) = tan(ThetaIn4)

ThetaIn4 = -50;
A = [0 0 0 0 1; L^4 L^3 L^2 L 1; 4*L^3 3*L^2 2*L 1 0; 12*L^2 6*L 2 0 0; 0 0 0
1 0];
b = [D1/2; D2/2; 0; 0; tan(ThetaIn4*pi/180)];
k4 = A\b          % Coefficients k are the constants to the quartic y4(x).

```

```

% Calculate radius, area, and gradient of the velocity ratio...
y4 = polyval(k4, x);
A4 = pi*y4.^2; V4oV1 = A4(1)./A4;
dV4oV1dxoL(1) = (V4oV1(2)-V4oV1(1))/(x(2)-x(1))*L;
dV4oV1dxoL(npts) = (V4oV1(npts)-V4oV1(npts-1))/(x(npts)-x(npts-1))*L;
for i=2:npts-1
    dV4oV1dxoL(i) = (V4oV1(i+1)-V4oV1(i-1))/(x(i+1)-x(i-1))*L;
end

figure(1)
    plot(x,y4,'--b',x,-y4,'--r'), axis( [0 12 -5 5] ); axis equal; xlabel('x
(in.)'); ylabel('y (in.)');
    text(x(401), y3(401), ' \leftarrow Cubic','FontSize',14)
    text(x(601), y4(601), ' Quartic \rightarrow','FontSize',14,
'HorizontalAlignment', 'right')
    hold off
figure(2)
    plot(x,A4,'--g',x,V4oV1,'--k'), legend('Nozzle Area (sq.in.)','Velocity
Ratio (V/V1)'), xlabel('x (in.)');
    text(x(950), V3oV1(950), ' \leftarrow Cubic','FontSize',14)
    text(x(915), V4oV1(915), ' Quartic \rightarrow','FontSize',14,
'HorizontalAlignment', 'right')
    hold off
figure(3)
    plot(x/L,dV4oV1dxoL,'--m'), xlabel('x/L'); ylabel('d(V/V1)/d(x/L)');
    text(x(701)/L, dV3oV1dxoL(701), ' \leftarrow Cubic','FontSize',14)
    text(x(701)/L, dV4oV1dxoL(701), ' Quartic \rightarrow','FontSize',14,
'HorizontalAlignment', 'right')
    hold off
[maxV,imax]=max(dV4oV1dxoL); maxV, x(imax)/L
figure(4)
    plot(x,y4,'b',x,-y4,'b'), axis( [0 12 -5 5] ); axis equal;
xlabel('Lateral Position (in.)'); ylabel('Vertical Position (in.)')

xlswrite('CubicNozzle2', [x' y3'])
xlswrite('QuarticNozzle2', [x' y4'])

```

APPENDIX B: VELOCITY PROFILE GENERATOR SCRIPT

```

clear
format compact
clc
%% Constants
D=1.8;
Dp=9.2;
Rem=13000; % Desired Velocity program Reynolds Number
nu=0.0017424; %kinematic viscosity of fluid (Water at 60 deg F)
Vmax=(Rem*nu)/D; % max velocity AT THE NOZZLE EXIT ; in inches per second
vmax=Vmax*(D/Dp)^2; %max PISTON velocity; in inches per second
%Vmax=input('Desired Maximum Velocity in in/s? ');

%% Shaft Input
a=1;
b=2;
c=3;
s=input('Shaft? ');
if s==1,
    J=1; % in/rev

end
if s==3,
    J=0.25; %in/rev

end
if s==2,
    J=0.5; %in/rev

end

K=51200/J; % microsteps per inch
vm=(vmax/J)*51200; % Max SHAFT VELOCITY; in microsteps/s
LDmax=10;

%% Profile Calculation
da=input('Acceleration Distance Fraction? ');
dd=input('Deceleration Distance Fraction? ');

V=[];
X=[];
Xnorm=[];
ltotalactual=[];
A=[];
Dec=[];
i=1;
for LD=(1:1:LDmax),
    Ltot=LD*D;
    Daccel=da*Ltot;

```

```

Ddecel=dd*Ltot;
j=1;
for x=(0:0.01:Ltot),
    X(i,j)=x;
    Xnorm(i,j)=x./Ltot;
    if x<=Daccel,
        V(i,j)=(vmax/Daccel)*x;
        j=j+1;
    else
        if (da+dd)~=1,
            if x<=Ltot-dd*Ltot,
                V(i,j)=vmax;
                j=j+1;
            else
                V(i,j)=(-vmax/Ddecel)*x+(vmax*Ltot)/Ddecel;
                j=j+1;
            end
        else
            V(i,j)=(-vmax/Ddecel)*x+(vmax*Ltot)/Ddecel;
            j=j+1;
        end
    end
end
ltotalactual(i)=(D/Dp)^2.*x; % In inches
DaccelTRU=da*ltotalactual(i)*K; % In microsteps
DdecelTRU=dd*ltotalactual(i)*K; % In microsteps
A(i)=vm^2/(2*DaccelTRU); % in microsteps/s^2
Dec(i)=vm^2/(2*DdecelTRU); % in microsteps/s^2
i=i+1;
end

MR=(ltotalactual.*K);
HC=10;
RC=100;
vi=1;

%% Output

HC
RC
vi
vm
A
Dec
MR

%% Plots

vmaxg=vmax+0.1*vmax;
lmaxg=LDmax*D+2;

% Plot for ACTUAL Piston

```

```

lactual=(D/Dp)^2.*X;
lactualmaxg=LDmax*D*(D/Dp)^2+0.1;
figure(i+1)
plot(lactual(1,:),V(1,:),lactual(2,:),V(2,:),lactual(3,:),V(3,:),lactual(4,:),
,V(4,:),...
     lactual(5,:),V(5,:),lactual(6,:),V(6,:),lactual(7,:),V(7,:),...
     lactual(8,:),V(8,:),lactual(9,:),V(9,:),lactual(10,:),V(10,:))
axis([0 lactualmaxg 0 vmaxg])
xlabel('Actual Piston Travel in inches')
ylabel('Velocity (in/s)')
%title('- - - - - Velocity Profiles')
legend('L/D=1','2','3','4','5','6','7','8','9','10')

% Normalized Profile Plot
Vnorm=V./vmax;
figure(i+2)
plot(Xnorm(1,:),Vnorm(1,:),Xnorm(2,:),Vnorm(2,:),Xnorm(3,:),Vnorm(3,:),Xnorm(
4,:),Vnorm(4,:),...
     Xnorm(5,:),Vnorm(5,:),Xnorm(6,:),Vnorm(6,:),Xnorm(7,:),Vnorm(7,:),...
     Xnorm(8,:),Vnorm(8,:),Xnorm(9,:),Vnorm(9,:),Xnorm(10,:),Vnorm(10,:))
axis([0 1.2 0 1.2])
xlabel('Normalized Piston Travel')
ylabel('Normalized Velocity (V/Vmax)')
%title('Normalized - - - - - Velocity Profiles')
%legend('L/D=1','2','3','4','5','6','7','8','9','10')

```

APPENDIX C: SAMPLE VELOCITY PROFILE

Hc=10
Rc=100
Vi=1
Vm=49327
A=215533
D=53883
S1=16,1
O1=0
S4=16,1
O4=0

PG 100
LB rightskew
P=0
O1=1
H 1
O1=0
MR 28223
H
PR P
E
PG

APPENDIX D: ENSEMBLE AVERAGING SCRIPT

```
%=====
function V3DAverager2006
%=====
% This transforms coordinates, calculates average data and statistics, and
% outputs the results in a 3D vector data file (V3S format). The resulting
% files are appropriate for use with the script, PIVSeamCalculator (for
% meshing static and dynamic data files).

% Clear out workspace and variable list...
clear, clc
OutputFlag = 1; % Indicates whether an output file is generated of average
values.
PlotFlag = 1; % Indicates whether surface plots are generated.

% Write out some initial header information to the workspace...
fprintf('Multiple file averaging for V3D data from PIV tests\n')
fprintf('NOTE: USE THE MULTI-SELECT OPTION (CTRL-LEFT CLICK)\n')
fprintf('-----\n')

% Open dialog to get all required V3D files (using multiselect)...
[FileNames, PathNameIn] = uigetfile('*.v3d','Multi-select required V3D
files','MultiSelect','on');
nfiles = length(FileNames);

%% FIRST PASS
% Load all the data into one huge, 3D data block...
for ifile=1:nfiles
    FileNameIn = char( FileNames(ifile) );
    disp(FileNameIn)
    [fid data] = readV3D(PathNameIn, FileNameIn);

% These don't really matter...
    run = data.run;
    labels = data.labels;
    m = data.m;
    n = data.n;
    values = data.values;
    nlines = m*n;

% Fill in the other instantaneous quantities (|V|, theta, phi)...
    for i=1:nlines
        speed = sqrt( (values(i,4))^2 + (values(i,5))^2 + (values(i,6))^2 );
        theta = 180/pi*atan( values(i,6)/values(i,5) );
        if values(i,5) < 0
            if values(i,6) < 0
                theta = -180 + theta;
            else
```

```

        theta = 180 + theta;
    end
end
V1 = sqrt( (values(i,5))^2 + (values(i,6))^2 );
phi = 180/pi*atan( V1/values(i,4) );
values(i,9) = speed;
values(i,10) = theta;
values(i,11) = phi;
end

% Stack the data into a huge, 3D data block...
datablock(:, :, ifile) = values;
end

avgvalues = zeros(nlines, 17);

%% SECOND PASS
% Process the data for averages...
% Cycle through the huge 3D data block, one line at a time...

fprintf('-----\n')
fprintf('Calculating average values')
fprintf('\n-----\n')

for i=1:nlines
    for ifile=1:nfiles
        if datablock(i,7,ifile) > 0;    % The vector is valid (otherwise,
it's a dropout).
            avgvalues(i,4:6) = avgvalues(i,4:6) + datablock(i,4:6,ifile);
            avgvalues(i,7) = avgvalues(i,7) + datablock(i,7,ifile);
            avgvalues(i,8:11) = avgvalues(i,8:11) + datablock(i,8:11,ifile);
        end
    end
    VectorCount = avgvalues(i,7);
    avgvalues(i,1:3) = datablock(i,1:3,1);
    if VectorCount > 0;
        avgvalues(i,4:6) = avgvalues(i,4:6)/VectorCount;
        avgvalues(i,8:11) = avgvalues(i,8:11)/VectorCount;
    else
        avgvalues(i,4:6) = NaN;
        avgvalues(i,8:11) = NaN;
    end
end
end

%% THIRD PASS
% Process the data for standard deviation and rms values...
% Cycle through the huge 3D data block, one line at a time...

fprintf('Calculating standard deviations')
fprintf('\n-----\n')

```



```

for i=1:nlines
    for ifile=1:nfiles
        if datablock(i,7,ifile) > 0;    % The vector is valid (otherwise,
it's a dropout).
            avgvalues(i,12:14) = avgvalues(i,12:14) + (
datablock(i,4:6,ifile) - avgvalues(i,4:6) ).^2;
            avgvalues(i,15:17) = avgvalues(i,15:17) + (
datablock(i,9:11,ifile) - avgvalues(i,9:11) ).^2;
            end
        end
        VectorCount = avgvalues(i,7);
        if VectorCount > 1;                % The vector is valid (otherwise,
it's a dropout)
            avgvalues(i,12:17) = ( avgvalues(i,12:17)./(VectorCount-1) ).^0.5;
        elseif VectorCount == 1
            avgvalues(i,12:17) = ( avgvalues(i,12:17) ).^0.5;
        else
            avgvalues(i,12:17) = NaN;    % The vector is invalid (a dropout,
etc.)
        end
    end
end

%% Prepare output information
% If output flag is true...
if OutputFlag == 1

% Add the column labels for the additional data stored in the V3S file...
    labelsout = labels;
    labelsout(9) = cellstr('Speed');
    labelsout(10) = cellstr('theta');
    labelsout(11) = cellstr('phi');
    labelsout(12) = cellstr('u Std Dev');
    labelsout(13) = cellstr('v Std Dev');
    labelsout(14) = cellstr('w Std Dev');
    labelsout(15) = cellstr('Speed Std Dev');
    labelsout(16) = cellstr('theta Std Dev');
    labelsout(17) = cellstr('phi Std Dev');

% Set up the output data block...
    dataout.run = run;
    dataout.labels = labelsout;
    dataout.m = m;
    dataout.n = n;
    dataout.values = avgvalues;

% Open dialog to get the V3S output filename...
    [FileNameOut,PathNameOut] = uiputfile('*.v3s','Output File');

    fprintf('Outputting data to a V3S file')
    fprintf('\nVector output file name: %s', FileNameOut);
    fprintf('\n-----\n')
    -----\n')

```

```

% Write V3S file contents.
    writeV3S(PathNameOut, FileNameOut, dataout)
end

%% Plot stuff
% If plot flag is true...
if PlotFlag == 1    % This dictates if surface plots are generated.

% Generate the contour (surface) plots for the averaged output...
% Set up the uniform grid.
    xmin = min(avgvalues(:,1));
    xmax = max(avgvalues(:,1));
    ymin = min(avgvalues(:,2));
    ymax = max(avgvalues(:,2));
    [xg,yg] = meshgrid(round(xmin):1:round(xmax), round(ymin):1:round(ymax));

% Create mesh-interpolated data arrays...
% Plotted number of valid vectors averaged...
    np = griddata(avgvalues(:,1),avgvalues(:,2),avgvalues(:,7),xg,yg);
    npmin = 0;
    npmax = nfiles;

% Plotted u velocity component...
    up = griddata(avgvalues(:,1),avgvalues(:,2),avgvalues(:,4),xg,yg);
    upmin = min( min(up) );
    upmax = max( max(up) );

% Plotted v velocity component...
    vp = griddata(avgvalues(:,1),avgvalues(:,2),avgvalues(:,5),xg,yg);
    vpmin = min( min(vp) );
    vpmax = max( max(vp) );

% Plotted w velocity component...
    wp = griddata(avgvalues(:,1),avgvalues(:,2),avgvalues(:,6),xg,yg);
    wpmin = min( min(wp) );
    wpmax = max( max(wp) );

% Plotted velocity magnitude (speed)...
    sp = griddata(avgvalues(:,1),avgvalues(:,2),avgvalues(:,9),xg,yg);
    spmin = min( min(sp) );
    spmax = max( max(sp) );

% Create the surface plots (flooded contours only)...
    title = 'Average of V3D files';

    figure('PaperOrientation','landscape', 'PaperPosition',[0.25 0.25 10.5
8], 'PaperSize',[11 8.5]);
    figure(1)
        GraphTitle = [title ' : u (m/s)'];
        SurfacePlot1(xg, yg, up, GraphTitle, xmin, xmax, ymin, ymax, upmin,
...

```

```

        upmax, 'x (mm)', 'y (mm)', 'u (m/s)');
figure(2)
    GraphTitle = [title ': v (m/s)'];
    SurfacePlot1(xg, yg, vp, GraphTitle, xmin, xmax, ymin, ymax, vpmin,
...
        vpmax, 'x (mm)', 'y (mm)', 'v (m/s)');
figure(3)
    GraphTitle = [title ': w (m/s)'];
    SurfacePlot1(xg, yg, wp, GraphTitle, xmin, xmax, ymin, ymax, wpmin,
...
        wpmax, 'x (mm)', 'y (mm)', 'w (m/s)');
figure(4)
    GraphTitle = [title ': Vector Count'];
    SurfacePlot1(xg, yg, np, GraphTitle, xmin, xmax, ymin, ymax, npmin,
...
        npmax, 'x (mm)', 'y (mm)', 'Number');
end

fprintf('\nDONE!')

```

APPENDIX E: VORTICITY CONTOUR GENERATOR SCRIPT

```

clear

load data

data1 = data;
[r,c] = size(data1);
badrows = [];

for i = 1:r
    for j = 1:c
        if data1(i,j) > 1e6
            data1(i,j) = 0;
        end
    end
end

%Assemble U, V, W matrices

I=168; % These Parameters Require Adjustment For Each Run Condition
J=127; % These Parameters Require Adjustment For Each Run Condition

colX = 1;
colY = 2;
colZ = 3;

for j = 1:J
    y(j) = data1(j*I,2);
end

for j = 1:J
    for i = 1:I
        U(j,i) = data1(i+I*(j-1),4);
        V(j,i) = data1(i+I*(j-1),5);
        W(j,i) = data1(i+I*(j-1),6);
    end
end

x = data1(1:I,1);
[X,Y]=meshgrid(x,y);

xi = [round(x(1)):2:round(x(length(x)))];
yi = [round(y(1)):-2:round(y(length(y)))];
[XI,YI,UI] = griddata(x,y,U,xi,yi,'cubic');
[XI,YI,VI] = griddata(x,y,V,xi,yi,'cubic');
cav = curl(XI,YI,UI,VI);

```

```
figure1 = figure('Colormap',[0 0 0.5625;0 0 0.625;0 0 0.6875;0 0 0.75;0 0
0.8125;0 0 0.875;0 0 0.9375;0 0 1;0.04545 0.04545 1;0.09091 0.09091 1;0.1364
0.1364 1;0.1818 0.1818 1;0.2273 0.2273 1;0.2727 0.2727 1;0.3182 0.3182
1;0.3636 0.3636 1;0.4091 0.4091 1;0.4545 0.4545 1;0.5 0.5 1;0.5455 0.5455
1;0.5909 0.5909 1;0.6364 0.6364 1;0.6818 0.6818 1;0.7273 0.7273 1;0.7727
0.7727 1;0.8182 0.8182 1;0.8636 0.8636 1;0.9091 0.9091 1;0.9545 0.9545 1;1 1
1;1 1 1;1 1 1;1 1 1;1 1 1;1 0.9545 0.9545;1 0.9091 0.9091;1 0.8636 0.8636;1
0.8182 0.8182;1 0.7727 0.7727;1 0.7273 0.7273;1 0.6818 0.6818;1 0.6364
0.6364;1 0.5909 0.5909;1 0.5455 0.5455;1 0.5 0.5;1 0.4545 0.4545;1 0.4091
0.4091;1 0.3636 0.3636;1 0.3182 0.3182;1 0.2727 0.2727;1 0.2273 0.2273;1
0.1818 0.1818;1 0.1364 0.1364;1 0.09091 0.09091;1 0.04545 0.04545;1 0
0;0.9375 0 0;0.875 0 0;0.8125 0 0;0.75 0 0;0.6875 0 0;0.625 0 0;0.5625 0
0;0.5 0 0]);
z=[ -.07 -.06 -.05 -.04 -.03 -.02 -.015 -.01 .01 .015 .02 .03 .04 .05 .06
.07];
contourf(cav,z)
axis([40 120 10 90])
xlabel('x in mm')
ylabel('y in mm')
```

```
figure2= figure('Colormap',[0 0 0.5625;0 0 0.625;0 0 0.6875;0 0 0.75;0 0
0.8125;0 0 0.875;0 0 0.9375;0 0 1;0.04545 0.04545 1;0.09091 0.09091 1;0.1364
0.1364 1;0.1818 0.1818 1;0.2273 0.2273 1;0.2727 0.2727 1;0.3182 0.3182
1;0.3636 0.3636 1;0.4091 0.4091 1;0.4545 0.4545 1;0.5 0.5 1;0.5455 0.5455
1;0.5909 0.5909 1;0.6364 0.6364 1;0.6818 0.6818 1;0.7273 0.7273 1;0.7727
0.7727 1;0.8182 0.8182 1;0.8636 0.8636 1;0.9091 0.9091 1;0.9545 0.9545 1;1 1
1;1 1 1;1 1 1;1 1 1;1 1 1;1 0.9545 0.9545;1 0.9091 0.9091;1 0.8636 0.8636;1
0.8182 0.8182;1 0.7727 0.7727;1 0.7273 0.7273;1 0.6818 0.6818;1 0.6364
0.6364;1 0.5909 0.5909;1 0.5455 0.5455;1 0.5 0.5;1 0.4545 0.4545;1 0.4091
0.4091;1 0.3636 0.3636;1 0.3182 0.3182;1 0.2727 0.2727;1 0.2273 0.2273;1
0.1818 0.1818;1 0.1364 0.1364;1 0.09091 0.09091;1 0.04545 0.04545;1 0
0;0.9375 0 0;0.875 0 0;0.8125 0 0;0.75 0 0;0.6875 0 0;0.625 0 0;0.5625 0
0;0.5 0 0]);
%z=[ -.07 -.06 -.05 -.04 -.03 -.02 -.015 -.01 0.01 .015 .02 .03 .04 .05 .06
.07];
z=[-0.03 -0.02 -.015 .015 0.02 0.03];
contourf(cav,z)
xlabel('x in mm')
ylabel('y in mm')
```

```
figure3 = figure('Colormap',[0 0 0.5625;0 0 0.625;0 0 0.6875;0 0 0.75;0 0
0.8125;0 0 0.875;0 0 0.9375;0 0 1;0.04545 0.04545 1;0.09091 0.09091 1;0.1364
0.1364 1;0.1818 0.1818 1;0.2273 0.2273 1;0.2727 0.2727 1;0.3182 0.3182
1;0.3636 0.3636 1;0.4091 0.4091 1;0.4545 0.4545 1;0.5 0.5 1;0.5455 0.5455
1;0.5909 0.5909 1;0.6364 0.6364 1;0.6818 0.6818 1;0.7273 0.7273 1;0.7727
0.7727 1;0.8182 0.8182 1;0.8636 0.8636 1;0.9091 0.9091 1;0.9545 0.9545 1;1 1
1;1 1 1;1 1 1;1 1 1;1 1 1;1 0.9545 0.9545;1 0.9091 0.9091;1 0.8636 0.8636;1
0.8182 0.8182;1 0.7727 0.7727;1 0.7273 0.7273;1 0.6818 0.6818;1 0.6364
0.6364;1 0.5909 0.5909;1 0.5455 0.5455;1 0.5 0.5;1 0.4545 0.4545;1 0.4091
0.4091;1 0.3636 0.3636;1 0.3182 0.3182;1 0.2727 0.2727;1 0.2273 0.2273;1
0.1818 0.1818;1 0.1364 0.1364;1 0.09091 0.09091;1 0.04545 0.04545;1 0
0;0.9375 0 0;0.875 0 0;0.8125 0 0;0.75 0 0;0.6875 0 0;0.625 0 0;0.5625 0
0;0.5 0 0]);
contourf(cav)
```

```
xlabel('x in mm')  
ylabel('y in mm')
```

[illegible]

GLOSSARY

Formation Number- the highest L/D for which a specific velocity profile forms a single vortex ring without a trailing jet

Nozzle Exit Overpressure (NEOP)- a phenomenon whereby the pressure is elevated above ambient at the exit plane of a nozzle through which fluid is being ejected

Pinch-off- the process wherein the vortex ring impinges on the fluid slug ejected from the nozzle, separating itself from the nozzle exit flow and forming a trailing jet

Slug Length to Diameter Ratio (L/D)- if the volume of fluid ejected from a nozzle were to be formed into a cylinder with the same cross-sectional area as the nozzle exit, L/D would be the length of the cylinder divided by the diameter of the nozzle exit

Stereoscopic Particle Image Velocimetry (SPIV)- a measuring technique whereby two digital cameras mounted at oblique angles to a fluid flow are used to record the motion of discrete particles in the flow, for the purpose of determining the three-dimensional velocity components of each particle in the flow

Trailing Jet- the weak vortex ring formed after the main vortex has undergone pinch-off

Velocity Profile- a plot of the velocity of a piston versus its position; a time-history of the motion of a piston

Vortex Ring- a region of rotational fluid in which individual particles move in streamlines about the circumferential axis of a torus. The net movement of the fluid is normal to the circumferential axis of the torus.

Vortex Ring Entrainment (VRE)- the process whereby ambient fluid is accelerated and swept into the toroidal vortex formed by the nozzle ejecta